A Rotor Flux Linkage Estimator and Operating Envelopes of a Variable-Flux IPM Synchronous Machine

Akrem Mohamed Aljehaimi

A Thesis

In the Department

of

Electrical and Computer Engineering

Presented in Partial Fulfillment of the Requirements

For the Degree of

Doctor of Philosophy (Electrical and Computer Engineering) at

Concordia University

Montréal, Québec, Canada

April 2018

CONCORDIA UNIVERSITY

SCHOOL OF GRADUATE STUDIES

This is to certify that the thesis prepared

By: Akrem Mohamed Aljehaimi

Entitled: A Rotor Flux Linkage Estimator and Operating Envelopes of a
                       Variable-Flux IPM Synchronous Machine

and submitted in partial fulfillment of the requirements for the degree of

Doctor of Philosophy (Electrical & Computer Engineering)

complies with the regulations of the University and meets the accepted standards with respect
to originality and quality.

Signed by the final examining committee:

_____Chair
Dr. Govind Gopakumar

_____External Examiner
Dr. Brij N. Singh

_____External to Program
Dr. Anjali Awasthi

_____Examiner
Dr. Shahin Hashtrudi Zad

_____Examiner
Dr. Luiz A.C. Lopes

_____Supervisor
Dr. Pragasen Pillay

Approved by _____
             Dr. Wei-Ping Zhu, Graduate Program Director

Thursday, May 31, 2018   _____
                           Dr. Amir Asif, Dean
                           Faculty of Engineering and Computer Science

ABSTRACT

A Rotor Flux Linkage Estimator and Operating Envelopes of a Variable-Flux IPM Synchronous Machine

Akrem Mohamed Aljehaimi, Ph.D.
Concordia University, 2018

Interior permanent magnet synchronous machines (IPMSMs) with rare-earth magnets are widely used by the electric and hybrid electric vehicle industry due to their high efficiency and high torque density. The drawbacks of the IPMSMs like the fluctuating prices of the rare-earth permanent magnets (PMs), the difficulty in flux weakening, and relatively low efficiency in high speed region, triggered the need for alternative electrical machines for traction applications. The variable-flux type IPMSMs, also called memory motors, is a promising technology for electrified transportation applications. These machines make use of low-coercivity magnets such as AlNiCo magnets, which makes them rare-earth PM independent. Moreover, owing to the low-coercivity, the AlNiCo magnets can be demagnetized in the high-speed region. This reduces or eliminates the extra current component needed for flux weakening, which results in lower copper/iron losses and improved machine efficiency. Besides, the variable-flux IPMSMs can provide torque densities comparable to rare-earth IPMSMs in high-torque low-speed regions.

Since the magnetization state of AlNiCo magnets can be varied online by a short stator current pulse, and the current needed for a particular magnetization state is machine parameter dependent, it is of a vital importance to the drive system to keep track of the magnet flux during transient and steady-state conditions. Moreover, failing in depicting the actual magnetization state of the magnets means a mismatch between the real value of the magnet flux in the machine and the estimated one in the controller, which directly affects the resultant torque and performance. In addition, the current pulse excitation method for magnetization causes non-uniform variable flux distribution in the air-gap. Therefore, an estimation algorithm of the rotor flux linkage of variable-flux IPMSMs via flux harmonics extraction has been proposed. Compared to the existing methods, this method does not need any voltage or current signal

injection into the stator winding. The algorithm was experimentally evaluated for different magnetization states and showed a good performance in tracking the rotor flux linkage variations during transient and steady-state conditions

The operating envelopes of the variable-flux IPMSM were found to be affected by the nonlinearity of the magnet flux with the machine direct axis current. New analytical solutions for the operating point were reached for maximum power and maximum output voltage control for the variable-flux IPMSM taking into consideration this nonlinearity. The experimental measurement performed also support the analytical results.

The irreversible demagnetization of the low-coercivity magnets in the high-speed region results in extending the braking time of the variable-flux IPMSMs. A simple yet effective minimal-time braking algorithm is proposed and experimentally validated.

AKNOWLEDGEMENT

First and foremost, I would like to thank Allah Almighty for giving me the strength and the ability to conduct and finish this piece of research. My deep thanks goes to Him for all the blessings he has given me even for this opportunity to thank Him.

My deep gratitude goes to my professor Pragasen Pillay, whom without his guidance, instructions, support, enlightenment, patience, and being there when help is most needed, this research won't be completed. Again, I thank Allah for giving me such a nice advisor and father in this long journey toward this degree.

I would like to acknowledge and thank my biggest source of encouragement, my family back home. My mom and father, without your continuous prayers, encouragement, and unconditional love, I would not be able to continue my PhD journey. I pray that Allah blesses you with a long and a happy life, and pray that He gives me the strength and wealth to return some your favors and compensate you for the years I lived far from you. To my darling wife, who have stood by my side during this journey, who bore the long hours I spent working in the lab far from her, who has taken care of our baby daughter when I was not having time to do so, and who always gives and asks little for herself, I am deeply thankful to you, and I ask Allah to give me the strength and time to make it up to you. To my naughty crying daughter, who never let me have a good sleep in the past one year and half, your smiles and hugs are what erases my tiredness whenever I come back home from work.

DEDICATION

To my parents,

Sasia Alshami,

Mohamed Aljehaimi,

Without whom none of my success would be possible

TABLE OF CONTENTS

LIST OF FIGURES

xiv

LIST OF TABLES

LIST OF ABBREVIATIONS

EV   Electric Vehicle

HEV   Hybrid Electric Vehicle

PM   Permanent Magnet

IPM   Interior Permanent Magnet

PMSM   Permanent Magnet Synchronous Machine

IPMSM   Interior Permanent Magnet Synchronous Machine

VFM   Variable-Flux Machine

VFIPMSM   Variable-Flux Interior Permanent Magnet Synchronous Machine

IS-VFIPMSM   Inverted-Saliency Variable-Flux Interior Permanent Magnet Synchronous Machine

FI-VFIPMSM   Flux-Intensifying Variable-Flux Interior Permanent Magnet Synchronous Machine

MS   Magnetization State

FOC   Field Oriented Control

Low-H_c Low Coercivity

d-axis   Direct Axis

q-axis   Quadrature Axis

emf   Electromotive Force

OCV   Open Circuit Voltage

DC   Direct Current

ANF   Adaptive Nonlinear Filter

MANF   Modified Adaptive Nonlinear Filter

PWM   Pulse Width Modulation

VSI   Voltage Source Inverter

VDSF   Voltage Disturbance State Filter

EKF   Extended Kalman Filter

NdFeB   Neodymium Magnet (rare-earth permanent magnet)

AlNiCo   Aluminum-Nickel-Cobalt

FE	Finite Element
LUT	Lookup Table
IGBT	Insulated-Gate Bipolar Transistor
ECG	Electrocardiogram
LPF	Low Pass Filter
FFT	Fast Fourier Transform
MTPA	Maximum Torque Per Ampere
MPPS	Maximum Power Per Speed
MTPF	Maximum Torque Per Flux
L	Limiter
S	Sample

LIST OF SYMBOLS

Symbol	Unit	Definition
v_d	V	d-axis stator voltage
v_q	V	q-axis stator voltage
V_a	V	Peak value of stator voltage
V_s	V	Maximum available voltage
i_d	A	d-axis current
i_q	A	q-axis current
i_s	A	Vector sum of d- and q-axis currents
I_a	A	Peak value of stator current
I_s	A	Peak value of rated stator current
L_d	H	d-axis inductance
L_q	H	q-axis inductance
λ_m	Wb-turn or V.s	Magnet flux which links the stator coils or rotor flux linkage
R_s	Ω	Stator winding resistance
ω	rad/sec	Electrical angular speed
ω_m	rpm	Mechanical angular speed
T	N.m	Electrical torque
P_{in}	W	Input power
P_{out}	W	Output power
P		Number of pole pairs
T_{SW}	Celsius	Stator winding temperature
V_{dc}	V	DC bus voltage
B	T	Magnetic flux density
H	A/m	Magnetic field intensity
λ_d	Wb-turn or V.s	Air-gap flux linkage d-axis component

λ_q	Wb-turn or V.s	Air-gap flux linkage q-axis component
$\lambda_a, \lambda_b, \lambda_c$	Wb-turn or V.s	a, b, c phase air-gap flux linkages
v_a, v_b, v_c	V	a, b, c phase voltages
θ_r	rad	Rotor angle
β	rad	Angle between stator current vector and q-axis
ξ	unitless	Saliency ratio (L_q/L_d)
V_l	V	Maximum available voltage
I_s^r	A	Peak value of machine rated current
I_{inv}^r	A	Peak value of inverter rated current
I_d^{limit}	A	d-axis current limit
I_q^{limit}	A	q-axis current limit
T_{rated}	N.m	Rated torque
$i_{d_{braking}}$	A	d-axis braking current reference
*		superscript indicates the reference value
^		superscript indicates the estimated value

Chapter 1.   Introduction

Research Background

Electric vehicles (EVs) have a recognized future of in transportation. In recent decades, both hybrid and pure electric vehicles (HEVs and EVs) have attracted much attention and experienced a rapid growth [1] [2]. In Canada, the province of Quebec has announced "The 2011-2020 Action Plan for Electric Vehicles", where 250 million dollars is being invested in the development and use of electric vehicles, and the EV related industrial sector [3].

The electric propulsion system is the heart of the EVs/HEVs with the electric motor being the core unit of the electric propulsion system. Hence improved performance of the HEVs/EVs is determined by the relevant improvements of the electric motors [4]. The major requirements of the EV electrical motors can be summarized as follows [5]: (a) high torque and power density, (b) high torque at starting, at low speeds and hill climbing, and high power for medium- and high-speed cruising, (c) wide speed range, (d) wide constant power operating range of 3-4 per unit speed, (e) high efficiency over a wide torque-speed range, and in particular at low-torque high-speed operating region, (f) short duration overloading capability, (g) high robustness and reliability appropriate to the vehicle environment, (h) acceptable cost, (i) low acoustic noise and torque ripple.
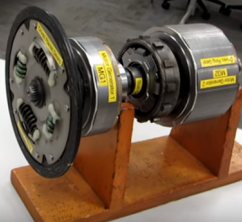
Various electric motors have been developed over the past few decades with the help of progress in materials, power electronics, and control drive technologies. Brushed electric motors require regular maintenance, hence less suitable for EVs/HEVs. Only wound field synchronous motors are utilized in very limited EVs, e.g. Renault Fluence and ZOE [6]. Brushless electric motors however enjoy more advantages, which make them suitable for EVs/HEVs [4]. The induction motors and permanent magnet synchronous motors are currently the two most dominant motors in EVs/HEVs [4]. The synchronous reluctance motors are also attracting attention for EVs/HEVs due to robustness, relative lower cost, and high speed operation [4]. However, their use in EVs/HEVs is still immature due to poor torque and overloading capabilities, low power factor, and high torque ripple which results in higher noise and vibration [4].

Induction motors are the main workhorse in many industry applications and are widely used in EVs/HEVs, especially in early designs. This is due to the robust structure, relatively low cost, well established manufacturing techniques, comparatively good efficiency and peak torque capability, and good dynamic performance which can be achieved by vector control or direct torque control [4]. However, their disadvantages include: (1) narrow constant power-speed range (2-3 per unit speed), thus to satisfy the EVs/HEVs demand, special IM designs are required, (2) lower efficiency compared to permanent magnets motor due to the inherent rotor loss, (3) low power factor, (4) difficulty of heat dissipation on the rotor [6].

Permanent magnet synchronous motors (PMSMs) are the most widely used motors for EVs/HEVs. This is due to: (1) high torque/power density, hence less volume per unit area, (2) high power factor, (3) high efficiency, (4) good heat dissipations as the heat mostly arises from the stator, (5) lower electromechanical time constant of the rotor, thus quick acceleration, (5) various configurations and adjustable performance [4] [5] [6] [7]. Also, this is the reason why they are always chosen as the benchmark of comparison between different motor types for EVs/HEVs. The main disadvantages include: (1) relatively high cost and uncertainty due to rare earth permanent magnets, (2) relative difficulty in flux weakening due to high coercivity permanent magnet excitation, (3) relatively lower efficiency at high speeds due to the additional current component needed for flux weakening, (4) risk of irreversible demagnetization due to high temperature, (5) high back electromotive force at high speeds in case of faults [4] [7].

For the previously mentioned advantages of PMSMs and their typical constant power-speed range (3-4 per unit speed), which is suitable for EVs/HEVs, almost the entire industry for light-duty EVs has shifted to PMSMs even after experiencing the high prices of rare-earth permanent magnets (PMs) [8]. Table 1-1 highlights some types and ratings of PM electric motors used in HEVs from well-known automotive companies like Toyota Motor Corporation, Aichi, Japan, and Honda Motor Company Ltd., Tokyo, Japan [8]. Those companies have been pioneers in commercializing HEVs. It can be noticed that the interior permanent magnet (IPM) is a dominant type of motors especially in Toyota. This is mainly due to its high speed capability. Also, the use of high DC bus voltage (by boost converter) in the Toyota Camry and Lexus can be noticed. This is to reduce the flux weakening requirement for high speed motors. Apart from light-duty EVs/HEVs, the IPM motors are finding a growing interest in medium-

and heavy-duty EVs/HEVs. UQM technologies, Longmont, Colorado is a leading company which provides liquid-cooled IPM machines for medium- and heavy-duty vehicles [9].

Table 1-1. Some PM motor/generator systems in the key HEVs [8] [10] [11].

Vehicle type:	Honda Civic 2006	
Stator:	Distributed winding	
Rotor:	Inset PM	
Rating:	30 kW/239 N.m	
DC bus voltage:	156 V	

Vehicle type:	Honda Accord 2017	
Stator:	Segment conductor winding	
Rotor:	IPM	
Rating:	135 kW/315 N.m	
DC bus voltage:	256 - 650 V	

Vehicle type:	Toyota Camry 2007	
Stator:	Distributed winding	
Rotor:	IPM	
Rating:	34 kW/275 N.m	
DC bus voltage:	244-650 V	Rotor

Vehicle type:	Toyota Lexus 2009	
Stator:	Distributed winding	
Rotor:	IPM	
Rating:	123 kW	
DC bus voltage:	650 V	

Vehicle type:	Toyota Prius 2004	
Stator:	Distributed winding	
Rotor:	IPM	
Rating:	50 kW/400 N.m	
DC bus voltage:	450 V	Rotor

Towards lower cost and improved efficiency, and with the help of progress in materials, variable-flux IPM synchronous motors have been recently introduced as a strong rival for IPM synchronous motors [12] [13] [14] [15] [16]. The costly high-coercivity rare-earth PMs, e.g.

Neodymium magnets (NdFeB), which are used in IPM motors, are replaced with low-coercivity non-rare-earth PMs, e.g. AlNiCo magnets, in variable-flux IPM motors. This fundamental change in the material type of PM allows the variable-flux IPM motors to overcome the previously mentioned disadvantages of IPM motors. To illustrate, (1) cost reduction due to independency of rare-earth PMs, (2) relative ease in flux weakening due to low-coercivity permanent magnet excitation, (3) relatively higher efficiency at high speeds due to reduction/elimination of the additional current component needed for flux weakening, (4) risk-free of irreversible demagnetization due high temperature, as the low-coercivity AlNiCo magnets can operate at temperatures up to 500°C without irreversible demagnetization. Moreover, they can provide high remanent flux density comparable to rare-earth PMs, e.g. 0.9-1.2 T, in the constant torque region.

This is why variable-flux IPMs is a very promising technology for EVs/HEVs. However, it is still immature and research is going on as this moment to improve and elevate this technology in different aspects e.g. machine design/optimization and control. Due to the low-coercivity of the AlNiCo PMs, the magnetic flux density can be easily altered with a short current pulse. This eliminates the extra current component needed for flux weakening, thus lower copper loss and improved motor efficiency. This means extra energy saving for the battery, which can be reflected in spee*d*-range extension of EVs/HEVs. Therefore, the key feature of the variable-flux IPM technology is the magnetization state manipulation to achieve better motor efficiency based on the operating point in the torque-speed envelope. The disadvantages include, (1) special rotor design is needed to prevent demagnetization of the magnets by load current, (2) relatively high magnetization current (2-3 per unit current), which results in an oversized inverter, (3) relatively low power capability in the flux weakening region due to irreversible magnet demagnetization, (4) the resultant back-emf harmonics due to complicated rotor geometries require more advanced rotor flux monitoring techniques, (5) braking in minimal time from relatively high speeds is challenging due to difficulty in magnetizing the magnets within the electric drive constraints.

Fig. 1-1 shows the rotor geometry of a proof-of-concept variable-flux IPM synchronous motor, which is designed in P. D. Ziogas Power Electronics Laboratory at Concordia University in 2015 [15]. In this design, low-H_c AlNiCo9 PMs are used. It is a 6 pole, 5 hp/36 N.m @ 900

RPM motor. It has an air cooled IM stator with a fractional winding. This motor is utilized in the following chapters for the experimental results validation of the presented work.
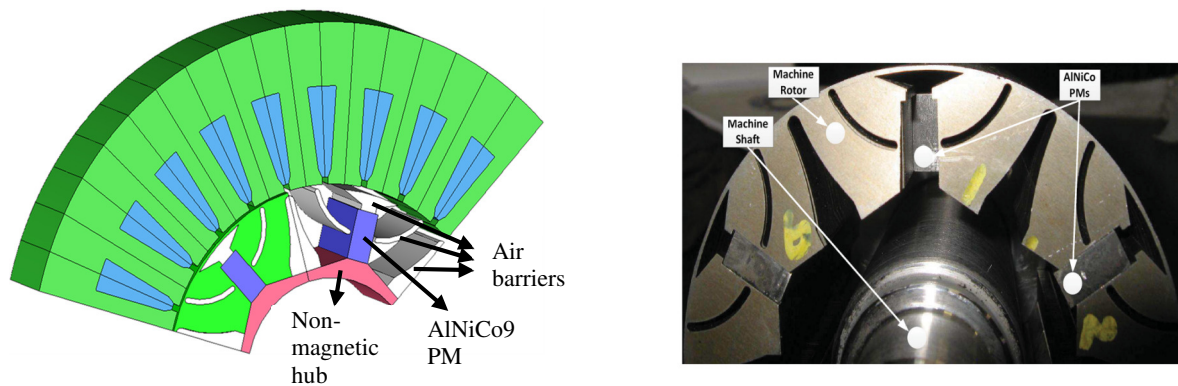
Fig. 1-1. Rotor geometry of a variable-flux IPM synchronous motor introduced in *[15]*.

Objectives

The objectives of this thesis are:

- To develop an online estimation technique for a magnet/rotor flux linkage of a variable-flux IPM synchronous motor, which takes into consideration the resultant flux harmonics due to the special-designed rotor.
- To investigate the torque/power-speed envelopes of the variable-flux IPM synchronous motor taking into consideration the nonlinear magnetization characteristics of the low-H_c magnets utilizing the developed flux estimator.
- To compare the variable-flux IPM synchronous motor with an equivalent IPM synchronous motor in terms of torque/power-speed capability, iron and copper losses, efficiency, and speed extension.
- To develop a minimal-time braking algorithm for variable-flux IPM synchronous motors utilizing the developed flux estimator.

Limitations

The limitations of the thesis are:

- Due to the unavailability of flux transducers, and the difficulty associated with their placement inside the motor due to limited space, the work on flux estimation is limited to the use of the measured voltage and current signals.

- Due to the unavailability of a high-bandwidth torque transducer, the measured motor torque is limited to the measured output power of the DC dynamometer and its losses.

- Due to unavailability of an equivalent IPM synchronous motor to the used variable-flux IPM synchronous motor, some of the presented work on the comparison is limited to simulated and finite-element obtained results.

Literature Review on Rotor Flux Linkage Estimation

A new vector control strategy for a variable flux machine was introduced in [13], [17]. In [13] and [17] the online demagnetization and remagnetization processes of the variable flux machine using d-axis current pulses was demonstrated. In [13] and [17], an offline look-up table of magnet flux versus current is used to determine the magnetization state (MS) of the magnets. A particular current that is required to get a magnetization state depends on machine parameters, i.e. stator resistance and inductances, which change depending on temperature. The look-up table presented in [13] and [17] fails to determine the actual magnetization state of the magnets online. Failing to depict the actual magnetization state of the magnets means a mismatch between the magnet flux in the control circuit and the real magnet flux in the machine which directly affects the resultant torque and machine current. Hence estimating the actual magnet flux is necessary to improve the torque control especially when magnet flux variation due to temperature rise and saturation is reported to be 3 to 20% depending on the type of the permanent magnet used in the machine [18].

Various methods for rotor flux linkage estimation of normal PMSMs have been presented in the literature and can be reviewed as follows.

In [19], an online identification method based on system identification theory for PMSM's parameters estimation was proposed. In system identification theory, it is known that the estimation accuracy cannot be ensured based on a rank-deficient reference model, and the PMSM's steady-state dq-model is known for rank-deficiency for simultaneously estimating the

stator resistance, *dq*-axis inductances, and rotor flux linkage [20]. Therefore, and according to [21] [22] [23] , it is impossible to estimate the rotor flux linkage and the winding resistance simultaneously from one set of PMSM states. Thus, [19] did not consider the full-rank of the PMSM's model, and suffers from ill convergence of stator resistance. Furthermore, it requires current signal injection for parameter estimation, which can cause instability and unwanted toque ripple. [11] proposed an extended Kalman filter (EKF) for rotor flux linkage estimation. However, it neglects the variation of stator resistance with temperature, and *dq*-axis inductances with current.

To have a full-rank model, several works [24] [25] [26] [27] [28] [29] [30] propose separating the parameters while estimating. In other words, once estimating a parameter, the other parameters are set to their nominal values. According to [22], not simultaneously estimating the rotor flux linkage and the stator winding resistance result in convergence to wrong points due to the mismatch between the actual and nominal values of the unestimated parameters. For instance, [25] proposed two model reference adaptive system estimators. One for estimating the winding stator resistance and rotor frequency while keeping the rotor flux linkage at its nominal value. The second one for estimating the rotor flux linkage and the rotor frequency while keeping the stator resistance at its nominal value. While both schemes were verified in [22] they suffer from the mismatch of the unestimated parameter, only the first scheme was reported in [25] to provide stable operation at low speeds. The same issue of the mismatch between the actual and nominal values of the unestimated parameters was reported in [26] when simultaneously estimating the stator resistance and *dq*-axis inductances while setting the rotor flux linkage at its nominal value.

In practice, the rotor flux linkage and the stator winding resistance are required for condition monitoring, e.g. temperature rise, magnet demagnetization, and faults. In this case, the rank-deficient issue should be resolved prior to estimation to avoid the mismatch between the actual and the nominal values [20]. Injecting a perturbation signal like $i_d \neq 0$ and dc voltage offset into the system to have a full-rank reference model was reported in [20] [22] [31] [32] [33] [34] as a solution to the rank-deficient issue. In [20], [22], [31] and [32], an instantaneous injection of *d*-axis current was implemented to activate the stator resistance term in the *d*-axis equation, thus, the stator resistance and the rotor flux linkage are estimated if the actual values of *dq*-axis inductances are available. However, due to the injection of the *d*-axis current, this

7

method suffers from the variation of dq-axis inductances. Moreover, the injection of d-axis current alters the MS of the magnets of variable flux machines. [33] introduced two least square based estimation algorithms with two different convergence speeds (slow and fast) as well as a three-level d-axis current signal injection in order to simultaneously estimate the rotor flux linkage, stator resistance, and dq-axis inductances. Despite the novelty of this method, it did not take into account the effect of inverter non-linearity. However, the injected three-level d-axis current signal varies the MS of the low- coercive magnets in the variable flux machine, thus adds one degree of complexity to the proposed scheme in [33]. [34] proposed an injection of a controlled dc voltage signal in one or more of motor phases in order to estimate the stator winding resistance online for small induction machines.

In [35], thermocouples and an Adaline estimator are used to estimate the stator winding resistance and the inverter nonlinearity, respectively. Then both are used to aid the estimation of the rotor flux linkage [35]. Since the distorted voltage due to inverter nonlinearity varies with current, the proposed Adaline estimator was designed to estimate the distorted voltage from the d-axis voltage equation assuming $i_d = 0$ [35]. This makes the proposed method in [35] suitable only for $i_d = 0$ control of a PMSM drive system. Nevertheless, the proposed method in [35] was able to overcome the rank-deficient issue, since it is independent of dq-axis inductances, and the stator resistance was estimated from the copper thermal coefficient through thermocouples prior to rotor flux estimation. Also a full-rank machine model was developed using a quantum genetic algorithm to estimate stator resistance, dq-axis inductances, and rotor flux linkage taking into account the inverter nonlinearity was proposed in [36] , which is suitable only for $i_d = 0$. [37] [38] proposed a method for estimating the mechanical parameters of PMSMs based on the rotor flux linkage estimation from a position offset-based parameter estimator (POPE). For POPE, two data sets for the encoder position error needed to be recorded, while the machine is loaded at constant speed and constant dq-axis currents, and used later as a look-up table for estimating the rotor flux linkage [37] [38]. This makes the proposed algorithm in [37] [38] encoder dependent, although it eliminates the dependency on the other motor parameters, e.g. stator resistance and dq-axis inductances, and the inverter nonlinearity in estimating the rotor flux linkage.

On the other hand, it was proposed in [18], [39], and [40] that the rotor flux linkage and stator winding resistance can be estimated by changing one of the operating conditions of the

8

machine; motor speed [39], [40], and induced torque [18]. However, this method ignores the change in stator resistance due to temperature. Furthermore, changing the operating condition might be difficult or not preferable in some applications. Therefore, this method has lower accuracy and applicability limitations.

A combination of a load test and a linear regression algorithm is reported to be a simple alternative solution for the rank-deficient issue [41], [42]. In [41] a load test was added for the rotor flux linkage estimation while [42] presented an embedded thermocouple in the stator in order to estimate the temperature of the stator winding resistance and rotor magnet.

In [43], a non-linear speed controller for a PMSM was proposed, in which two reduced-order disturbance observers are used to estimate the rotor flux linkage and torque disturbances, respectively. The full-state observer was achieved by assuming the disturbance parameters are slowly varying, thus considered constant during a sampling interval, and by assuming that the rotor speed is not zero. Despite the innovation of the method, it uses the nominal values of stator inductance and resistance. Thus, the observers still suffer from the mismatch between the actual and nominal values of the unestimated parameters.

[44] proposed a pulsating high-frequency voltage signal injection on the fundamental excitation to estimate the high- frequency stator-reflected permanent magnet resistance, thus the magnetization state of the magnets can be estimated. This was done under the assumption that the permanent magnet high-frequency resistance is dominant in the rotor d-axis high frequency resistance [44]. This is quite accurate for the SPMSMs as the magnets shield the rotor laminations, and the high-frequency voltage signal induces eddy currents mainly in the permanent magnets [45] [46] [47]. In IPMSMs, both the rotor laminations and the permanents magnets are affected by the high-frequency flux caused by the high-frequency voltage signal injection [44] [48]. Thus, compensating for the high-frequency resistance of the rotor lamination is required, which is not a trivial task as it is influenced by the rotor geometry [44] [48]. The influence of rotor geometry, in IPMSMs, on the response to the high-frequency voltage signal injection method was investigated in [48], and special rotor design criteria were suggested to help improve the estimation method of the high-frequency injection in sensorless control of IPMSMs. Moreover, [44] did not account for the nonlinearity effect of the inverter on the injected high-frequency voltage signal, which was reported to be significant, especially when low-magnitude high-frequency voltage signals are being injected [49] [50]. Nevertheless,

9

the high-frequency voltage signal injection method is independent of dq-axis inductances and can be used even at stand-still [51]. Thus, the effect of the induced high-frequency current signal on the magnetization state of the low-coercive magnets can be seen.

A decoupling current observer-based method was proposed in [52] to achieve a smooth torque during magnetization manipulation of a variable flux IPMSM. In this work, to mitigate the parameter variations effect, e.g. stator resistance and PM flux with temperature and dq-axis inductances with current, on the estimated air-gap flux linkage, a voltage disturbance state filter (VDSF) was used. Although, this method did not estimate the machine parameters (stator resistance and dq-axis inductances) with the aim of air-gap flux linkage estimation, but rather mitigate their variation from the nominal values, it still suffers from the mismatch between the actual and the nominal values of the unestimated parameters. Moreover, since the reference voltage modulating signals are used in the proposed flux estimator without compensating for the distorted voltage due to VSI nonlinearity, the method suffers from voltage source inverter (VSI) nonlinearity effects, which was reported to be significant in several research works [35] [36] [53].

This thesis presents a rotor flux linkage estimation of a variable flux machine at different flux density levels through the electromotive force harmonics estimation of the machine. For the back emf harmonics estimation, a modified adaptive nonlinear filter which is able to extract the amplitude, phase angle, and frequency of a nonstationary sinusoid embedded in a nonstationary signal is used. The stator winding resistance is estimated prior to rotor flux linkage estimation through the thermal coefficient of the copper as in [54] [55]. Thus, thermocouples are used for this purpose. The variation of machine dq-axis inductances with current as well as with magnetization state of the magnets is considered for more accurate rotor flux estimation. To compensate for the VSI nonlinearity, which is caused mainly by the dead-time, the average value theory presented in [56] was adopted for this purpose. Thus, the proposed method is free of d-axis current injection or high-frequency voltage signal injection, and it does not require a change in the operating condition in order to estimate the rotor flux linkage. Moreover, since the back emf of the variable flux machines is usually non-sinusoidal due the special rotor geometry design [16] [57], the proposed method utilizes the flux harmonics in estimating the rotor flux linkage instead of estimating the average value depending only on the fundamental.

Thesis Outline

This thesis proceeds as follows.

Chapter 2: This chapter presents an overview of the drive system of the variable-flux IPM synchronous motor, which was proposed by a former Ph.D. student of Prof. Pragasen Pillay (Dr. Lesedi Masisi) in [17].

Chapter 3: This chapter presents a novel algorithm for online rotor flux linkage estimation for a variable flux IPM synchronous machine drive system at different flux density levels. A modified adaptive nonlinear filter (MANF) is used to instantaneously estimate the amplitude, phase angle and frequency of the major back emf harmonic components, from which the total air gap flux linkage is estimated. The algorithm avoids the averaging method which depends only on the fundamental back emf component in estimating the air gap flux linkage.

Chapter 4: This chapter aims to investigate and compare the different possible operating envelopes of the variable-flux IPM synchronous machine from the drive point of view. Demagnetizing the low-coercive magnets via only a short d-axis current pulse eliminates the need of continuously applying a negative d-axis current in the flux-weakening region; hence lower copper loss and improved motor efficiency is expected. In this chapter, this has been investigated and compared with the utilization of continuous negative d-axis current in the flux-weakening region considering the non-linear demagnetization characteristics of the low-coercive magnets. The latter scheme has been seen to improve the high-speed output characteristics and to extend the speed-range. Also, the high-speed power capability of the variable-flux IPM synchronous motor is shown to be feasible with the latter scheme via saliency manipulation. Moreover, a comparison between a variable-flux IPM synchronous motor and an equivalent IPM synchronous motor is presented in this chapter.

Chapter 5: This chapter proposes a method for braking the variable flux IPM synchronous motor in a minimal time condition while operating in the high-speed region. The IPMSM has its inherent characteristics of magnet flux being recoiled to its maximum value as the speed decreases and crosses the rated speed. This inherent feature of the IPMSM makes the braking

torque maximization possible, thus minimal time braking can be achieved. In contrast, the low-coercive permanent magnets utilized in variable flux IPM synchronous motors are irreversibly/permanently demagnetized in the high-speed region. This means the variable-flux IPMSM takes a longer time to stop if compared to the IPMSM. Supplying a magnetizing current, which ranges from one to three per unit current, in the high-speed region where the inverter runs out of voltage is quite challenging. In this chapter, an analytical solution to the amount of magnetizing current required to maximize the braking torque based on the available voltage to ensure minimal time braking is presented. A front-end active rectifier is utilized to recuperate the braking energy and keep the DC link voltage constant.

Chapter 6: This chapter presents thesis conclusions and future work.

Contributions

The achieved contributions in this Ph.D. work are as follows.

I.   In chapter 3, a novel online rotor flux linkage estimation algorithm has been designed for variable-flux IPM synchronous motors. The estimator scheme has been experimentally evaluated for different magnetization states and has showed a good performance in tracking the rotor flux linkage variations. The resultant publications out of this chapter are as follows,

Akrem Mohamed Aljehaimi and Pragasen Pillay, "Online rotor flux linkage estimation for a variable flux interior permanent magnet synchronous machine operating at different flux density levels," *in IEEE International Conference on Power Electronics, Drives and Energy Systems (PEDES)*, Trivandrum, India, 14-17 Dec. 2016. DOI**:** 10.1109/PEDES.2016.7914310.

Akrem Mohamed Aljehaimi and Pragasen Pillay, "Novel Flux Linkage Estimation Algorithm for a Variable Flux PMSM," *IEEE Transactions on Industry Applications*, vol. 54, no. 3, p. 2319-2335, May/June 2018. DOI: 10.1109/TIA.2018.2794338.

II. In chapter 4, an investigation study on the possible operating envelopes of the variable flux IPM synchronous motor using both methods of demagnetization, either demagnetization current pulse or continuous demagnetization current has

been established. In addition to a comparative study between a variable-flux IPMSM and an equivalent IPMSM has been conducted. The resultant publications out of this chapter are as follows,

Akrem Mohamed Aljehaimi and Pragasen Pillay, "Torque and power improvement for a variable flux permanent magnet synchronous machine," *in IEEE Transportation Electrification Conference and Expo (ITEC)*, Chicago, USA, 22-24 June 2017. DOI**:** 10.1109/ITEC.2017.7993308.

Akrem Mohamed Aljehaimi and Pragasen Pillay, "Operating Envelopes of the Variable Flux Machine with Positive Reluctance Torque," *Accepted for publication in IEEE Transactions on Transportation Electrification*, 18 Apr. 2018. DOI: 10.1109/TTE.2018.2828385.

III.   In chapter 5, the issue of minimal-time braking from relatively high speeds with variable-flux IPM synchronous motors has been highlighted for the first time in the literature. A suitable braking algorithm has been developed and experimentally validated. A transaction article out of this chapter has been written and submitted to IEEE Transactions on Transportation Electrification.

Akrem Mohamed Aljehaimi and Pragasen Pillay, "Braking a Variable Flux-Intensifying IPMSM in Minimal Time," *Accepted for publication in IEEE Transactions on Transportation Electrification*, 17 Aug. 2018. DOI: 10.1109/TTE.2018.2865908.

Chapter 2.   An Overview of the Drive System of the Variable-Flux IPMSM

Introduction

As was illustrated in the previous chapter, machines of high-torque/power density and high efficiency are required for traction applications. This is why the IPMSMs are the choice for EVs/HEVs, despite the price uncertainty of the rare-earth permanent magnets (PMs). However, the benefits of the variable-flux IPMSMs, e.g. the independence of rare-earth PMs, the ease of flux-weakening, and the higher efficiency in the low-torque high-speed region, ignite the research to investigate their applicability in traction applications.

The key feature of variable-flux IPMSMs is the employment of low-coercivity magnets, which can be demagnetized as needed on the fly via a short *d*-axis current pulse. This results in eliminating or reducing the excessive flux-weakening current in the high-speed region. Thus, lower copper and iron losses and improved machine efficiency are possible. A proof-of concept variable-flux IPMSM using AlNiCo9 magnets was introduced in [16] [15], for which a drive design was proposed in [17]. In this chapter, an overview of the drive system which was proposed in [17] will be presented along with some experimental results at different operating points in the torque-speed envelope.

Machine Model

The steady-state voltage equations of the three-phase variable-flux IPMSM in the *dq*-synchronous-rotating reference frame are [58]:

$$\begin{bmatrix} v_d \\ v_q \end{bmatrix} = \begin{bmatrix} R_s & 0 \\ 0 & R_s \end{bmatrix} \begin{bmatrix} i_d \\ i_q \end{bmatrix} + \begin{bmatrix} 0 & -\omega L_q \\ \omega L_d & 0 \end{bmatrix} \begin{bmatrix} i_d \\ i_q \end{bmatrix} + \omega \begin{bmatrix} 0 \\ \lambda_m(i_d) \end{bmatrix} \tag{2-1}$$

where,

v_d, v_q *d*- and *q*-axis armature voltage components,

i_d, i_q *d*- and *q*-axis armature current components,

L_d, L_q d- and q-axis armature self-inductance components,

R_s phase stator resistance,

ω rotor electrical angular velocity, and

$\lambda_m(i_d)$ magnet/rotor flux linkage as a function of d-axis current.

The induced torque (T) is given by

$$T = \frac{3P}{2}\left[i_q\,\lambda_m(i_d) + \left(L_d - L_q\right)i_d i_q\right]$$

(2-2)

where, P is the number pole pairs [58]. The magnet flux which links the stator coils called the rotor flux linkage (λ_m) is a function of the d-axis current. Fig. 2-1 depicts the measured change in the AlNiCo9 magnet flux linkage with d-axis current in the second quadrant.
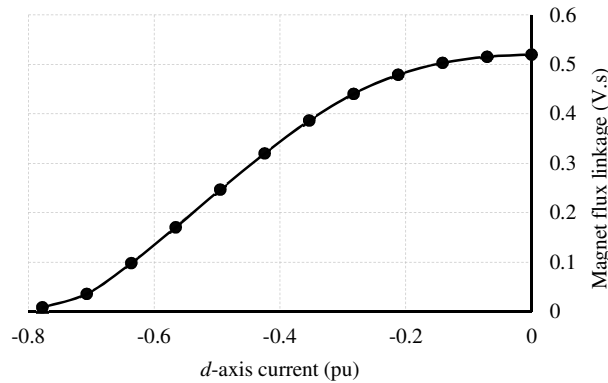
Fig. 2-1. Offline-measured demagnetization curve of the AlNiCo9 magnets.

Operating Point Trajectories of AlNiCo9 Magnets during Magnetization

The demagnetization and remagnetization dynamics of the VFM are examined using FE simulation. Fig. 2-2(a) shows the magnetic flux density of the magnet when the machine is fully magnetized and running unloaded at 1200 rpm. This corresponds to point (w) on the B-H curve of the magnet as shown in Fig. 2-2(c). At a simulation time of 0.01667 s, a demagnetizing current pulse of 6 A is applied for one electrical cycle as shown in Fig. 2-2(b). Due to this demagnetizing current, the magnets are exposed to an external magnetic field which drives the
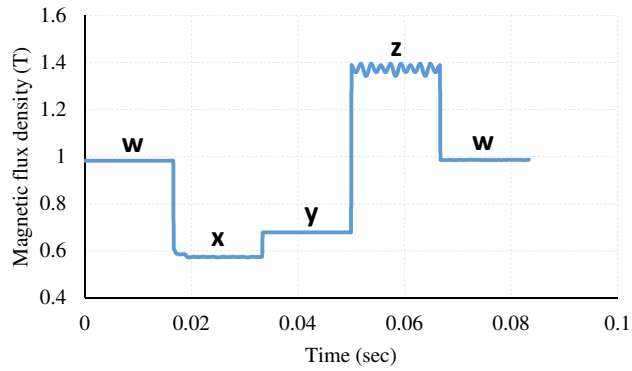
(a)
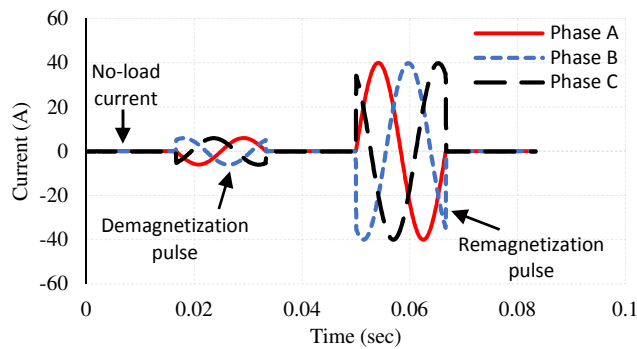
(b)
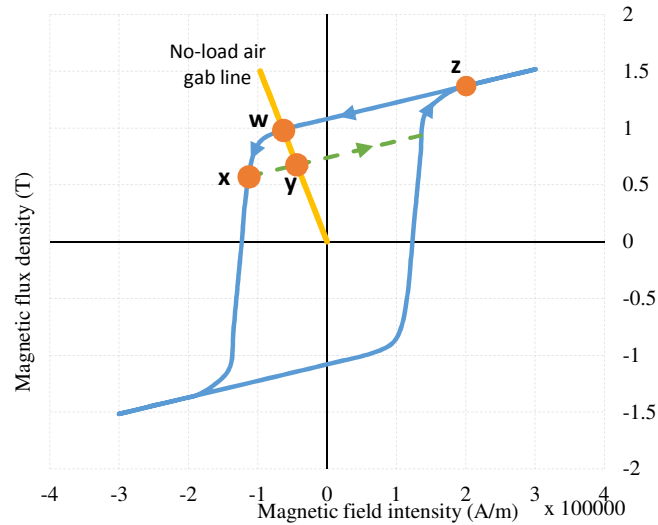
(c)

Fig. 2-2. AlNiCo9 PM operating point trajectories in FEA when magnetizing pulses are applied. (a) Simulated magnetic flux density. (b) Simulated three-phase currents. (c) B-H curve of AlNiCo 9.

operating point of the magnets below the knee to point (x) as shown in Fig. 2-2 (c). After the removal of the demagnetization current at 0.0333 s, the magnet recoils along a new magnetization curve parallel to the original demagnetization curve. The magnet operating point

is shifted to the intersection of the no-load air gap line and the new demagnetization curve (point y). At 0.05 s, a magnetization pulse of 40 A is applied for one electrical cycle as shown in Fig. 2-2(b). This magnetization field shifts the magnet operating point to point (z) as shown in Fig. 2-2(a) and Fig. 2-2(c). Once the magnetization current is released at 0.06667 s, the magnet recoils along the original magnetization curve to point (w).

Overview of the Drive System

The block diagram of the drive system of a variable-flux IPMSM is shown in Fig. 2-3 [17]. It is a field-oriented vector-control based approach, where the torque and flux channels of the machine are decoupled through its stator-excitation inputs. The output of the speed control loop is the torque reference, which is translated into a q-axis current command. The d-axis current command, which is the machine's flux channel command, is either a zero, a flux-weakening current, or a magnetization pulse current. The zero d-axis current control is the simplest vector control technique which can be used up to the base speed. Beyond base speed, the growing back electromotive force (back emf) exceeds the maximum available voltage from the inverter and needs to be compensated. In this case, the back emf is lowered by either a flux weakening current or by a demagnetization current pulse. The flux weakening controller is a proportional integral based compensator. Once the stator voltage exceeds the maximum available voltage from the inverter, the compensator generates the required negative d-axis to weaken the air-gap flux allowing the machine to accelerate and follow the speed reference command.

In variable-flux machines, this current can be eliminated by demagnetizing the magnets to a certain level via a short d-axis current pulse. The speed, q-axis current, and d-axis current proportional integral controllers are tuned online to obtain acceptable speed and current responses. The output of the dq-axis current controllers are the dq-axis stator reference voltages. Those voltage signals form the modulating signals of the space vector pulse width modulation (PWM) technique. The triangle carrier signal is of 5 kHz frequency, which makes the switching frequency of the inverter switches. The sampling rate is 50 kS/s or 20 μs sampling time. The output of the PWM block is the gating signals which drive the inverter. The control and the PWM schemes are implemented by an Opal-RT real-time simulator [59]. The experimental setup is shown in Fig. 2-4. In [13] [17], an offline-obtained look-up table (LUT) of the rotor

17

flux linkage versus *d*-axis current is used to estimate the rotor flux linkage online as seen in Fig. 2-3.
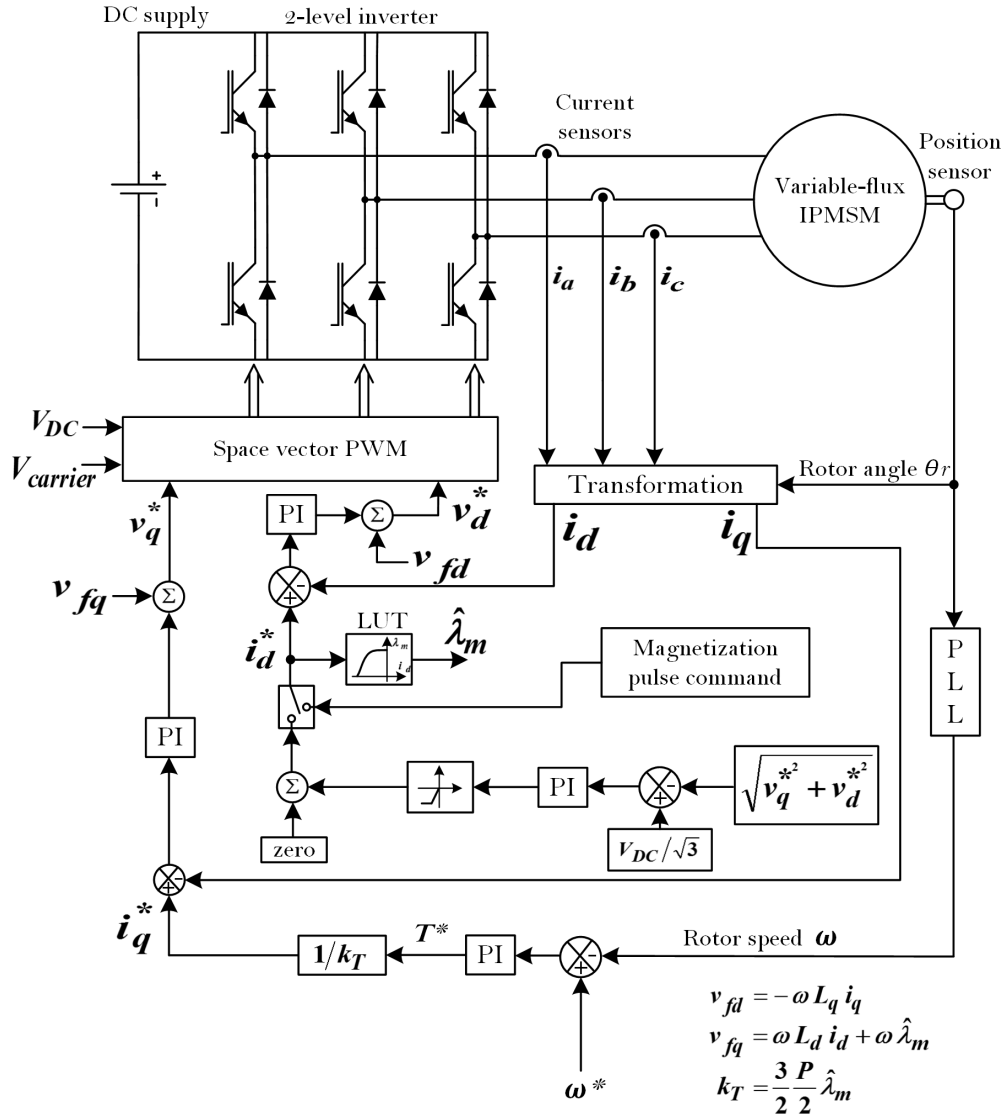
Fig. 2-3. Block diagram of the drive system.

Fig. 2-5 shows the variable-flux IPMSM running fully loaded at rated speed. In this scenario the AlNiCo9 magnets are kept fully magnetized in order to meet the demanded load torque. Fig. 2-6 shows an experimentally obtained result of an online magnet demagnetization via a negative *d*-axis current pulse beyond the base speed. As the speed increases, the modulation index crosses unity. Thus, the flux weakening controller operates, and a continuous
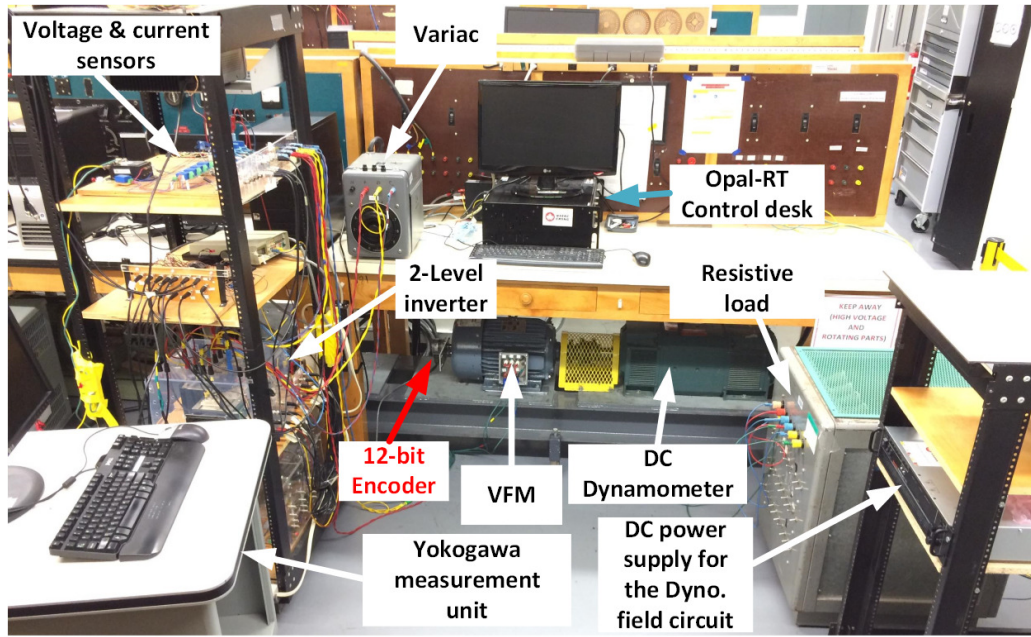
Fig. 2-4. Experimental setup.
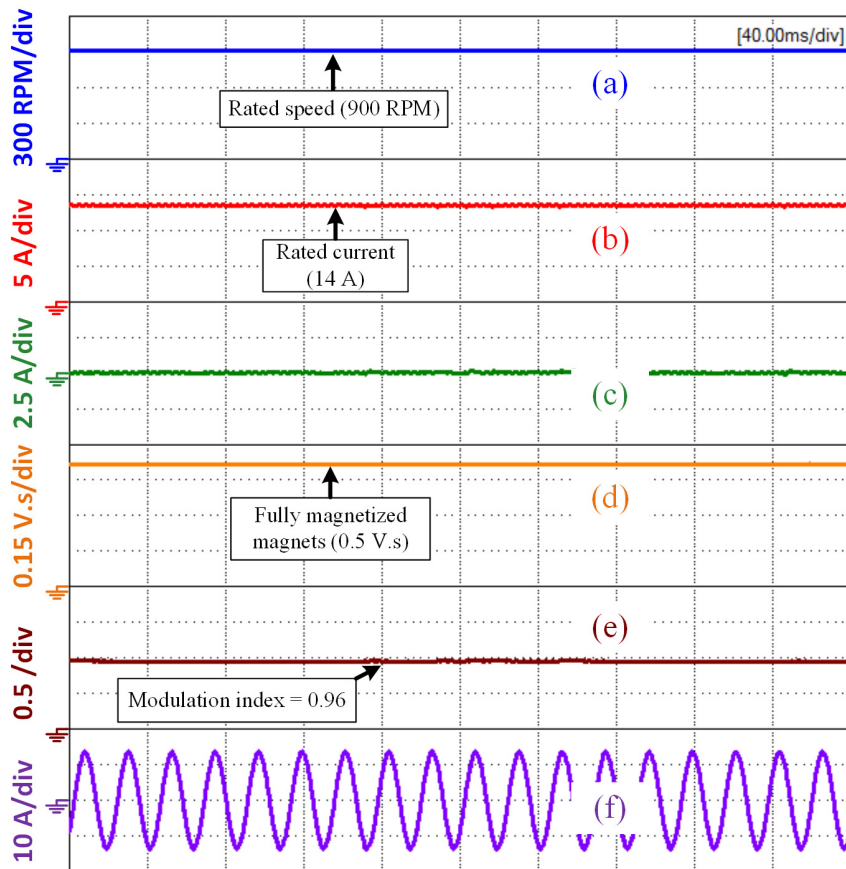
Fig. 2-5. Illustration of motor performance at rated condition (36 N.m): (a) motor speed, (b) q-axis current, (c) d-axis current, (d) estimated rotor flux linkage via a LUT, (e) modulation index, (f) phase current.

negative *d*-axis current is drawn by the motor in order to counter the growing back emf. From Fig. 2-6, it can be seen that once the motor speed reaches a steady state, a negative 2 A *d*-axis current is continuously needed. Thereafter, a demagnetization pulse of negative 6 A is excited, which demagnetizes the magnets to almost 0.32 V.s (60% MS). This demagnetization process reduces the amount of the needed flux weakening current as seen in Fig. 2-6. Moreover, once the demagnetization by negative *d*-axis current pulse occurred, the load current (*q*-axis current) is consequently increased in order to meet the load torque requirement.
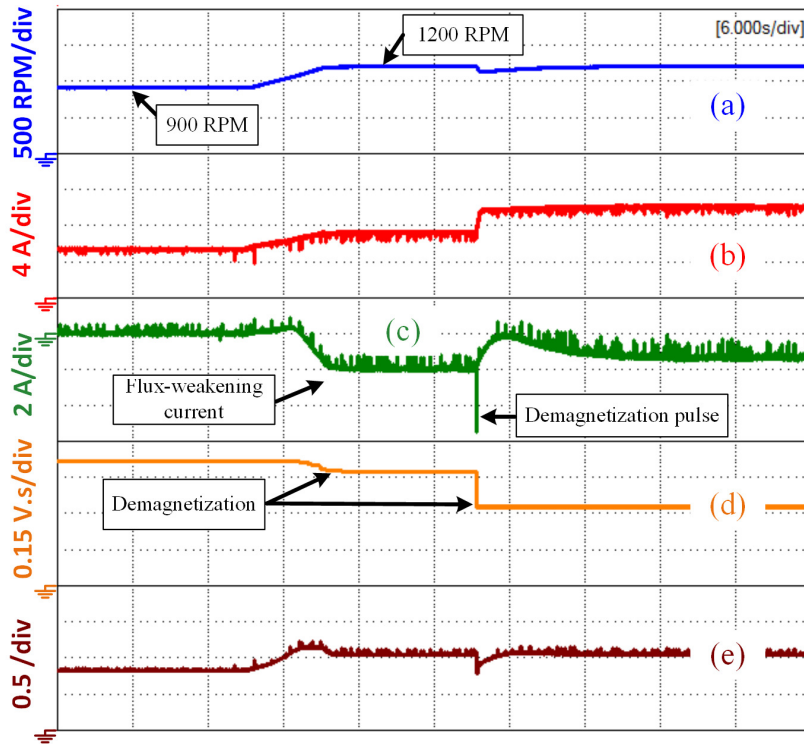
Fig. 2-6. Illustration of the flux-weakening current reduction by magnet demagnetization: (a) motor speed, (b) *q*-axis current, (c) *d*-axis current, (d) estimated rotor flux linkage via LUT, (e) modulation index.

Fig. 2-7 shows the elimination of the flux-weakening current and consequently the reduction of the machine current in the high-speed low-torque region. As seen in Fig. 2-7, the motor speed is first ramped up from 1100 RPM to 1400 RPM where a negative 1 A of flux-weakening current is needed. Then, a negative 3 A demagnetization pulse is excited to demagnetize the magnets to almost 85%. As a result the flux-weakening current is eliminated and the machine current is reduced as seen in Fig. 2-7(b) and (e). After that the motor speed is ramped up again from 1400 RPM to 1800 RPM, in which a negative 2.2 A flux weakening current is needed. Thereafter, a negative 5 A demagnetization pulse is excited, which

demagnetizes the AlNiCo9 magnets to almost 50%. Consequently, the flux-weakening current is eliminated and the total machine current is reduced. This will be further illustrated in chapter 4, when the operating envelopes of the variable-flux IPMSM is examined.
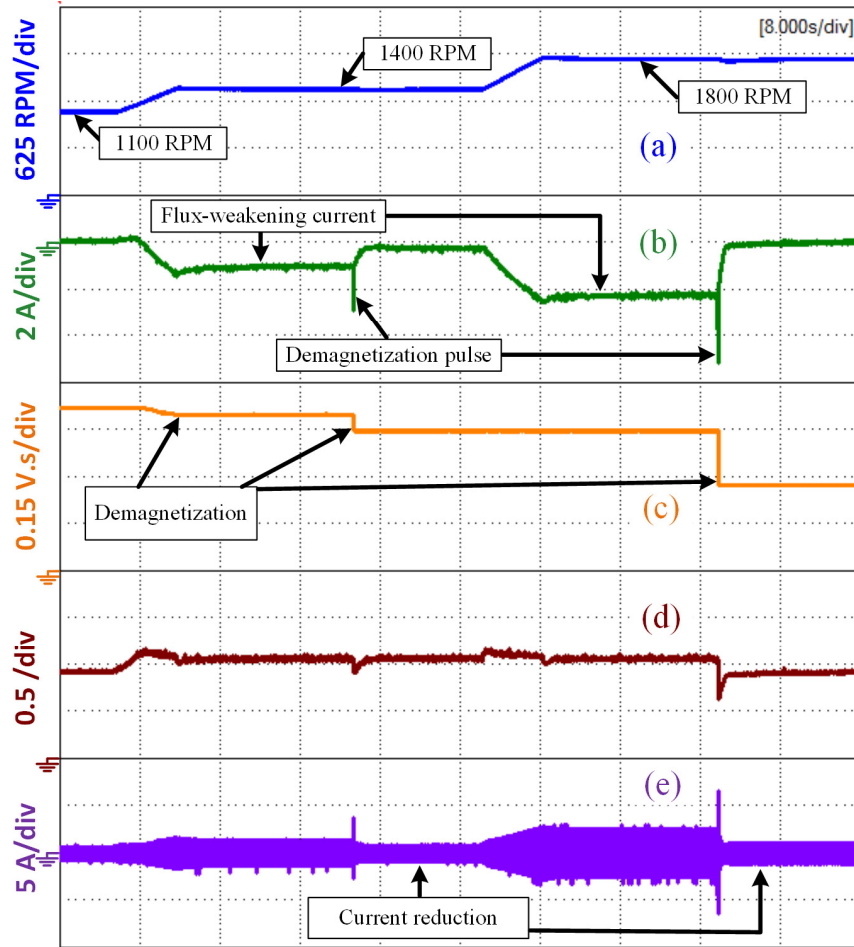
Fig. 2-7. Illustration of the flux-weakening current elimination by magnet demagnetization: (a) motor speed, (b) *d*-axis current, (c) estimated rotor flux linkage via LUT, (d) modulation index, (e) phase current.

Summary

In this chapter, the functionality of the rotor flux linkage with *d*-axis current in the machine model was presented. The operating point trajectory of the AlNiCo9 magnet during the magnetization process is illustrated. Moreover, an overview of the drive system with the experimental results is demonstrated.

Chapter 3.   A Novel Flux Linkage Estimation Algorithm for a

Variable-Flux IPMSM

Introduction

Permanent magnet synchronous machines (PMSMs) are widely used in industrial servo drives, wind power generators, electrical and hybrid electrical vehicles, etc. This is due to high power/torque density, high performance, high efficiency, and desirable control characteristics [60].

However, the price fluctuation of rare earth PMs has triggered the research for alternative motor technologies which are independent of rare-earth magnets [16]. A novel design of a variable-flux interior permanent magnet synchronous machine (VFIPMSM) which uses AlNiCo9 magnets was introduced in [16]. In [16], it was shown that AlNiCo9 magnets can operate at flux densities comparable to rare-earth magnets, and their magnetization level can be altered through a short armature current pulse. This is what makes the variable flux machines (VFMs) unique. However, for variable flux machines, where the rotors are specially designed to prevent magnet demagnetization by load current (i_q), usually the electromotive force is not purely sinusoidal [16] [57]. In fact, it contains harmonics due to the design aspects [16] [57]. In addition, the demagnetization and remagnetization processes, e.g. *d*-axis current pulse excitation, causes non-uniform variable flux distribution in the air-gap. Therefore, this requires higher accuracy in estimating the magnet flux linkage for the VFMs, through the harmonic extraction, than in the normal PMSMs, which is the focus of this chapter.

A novel vector control strategy for a variable flux machine was introduced in [13] [17]. In [13] and [17] the online demagnetization and remagnetization processes of the variable flux machine using *d*-axis current pulses was demonstrated. In [13] and [17], an offline look-up table of magnet flux versus current is used to determine the magnetization state (MS) of the magnets. A particular current that is required to get a magnetization state depends on machine parameters, i.e. stator resistance and inductances, which change depending on temperature. The look-up table presented in [13] and [17] fails to determine the actual magnetization state of the magnets online. Failing to depict the actual magnetization state of the magnets means a mismatch

between the magnet flux in the control circuit and the real magnet flux in the machine which directly affects the resultant torque and machine current. Hence estimating the actual magnet flux is necessary to improve the torque control especially when magnet flux variation due to temperature rise and saturation is reported to be 3 to 20% depending on the type of the permanent magnet used in the machine [18].

Proposed Scheme

The rotor flux linkage is estimated from the measured values of the phase motor voltages and currents, stator resistance, and d-axis inductance. The machine phase voltages are measured right at the machine terminals (phase to neutral). This eliminates the need of compensating the drop voltage due to voltage source inverter nonlinearity. Fig. 3-1 shows the block diagram of the estimation scheme. First, the manifold of phase back emf signal is measured by subtracting the voltage drop on the phase resistance from the machine phase voltage. This manifold signal contains all back emf harmonics, switching components, and noise. Here comes the importance of using the modified adaptive nonlinear filter to extract only the harmonics that shape the exact back emf signal of the machine. By integrating the extracted back emf harmonics and adding
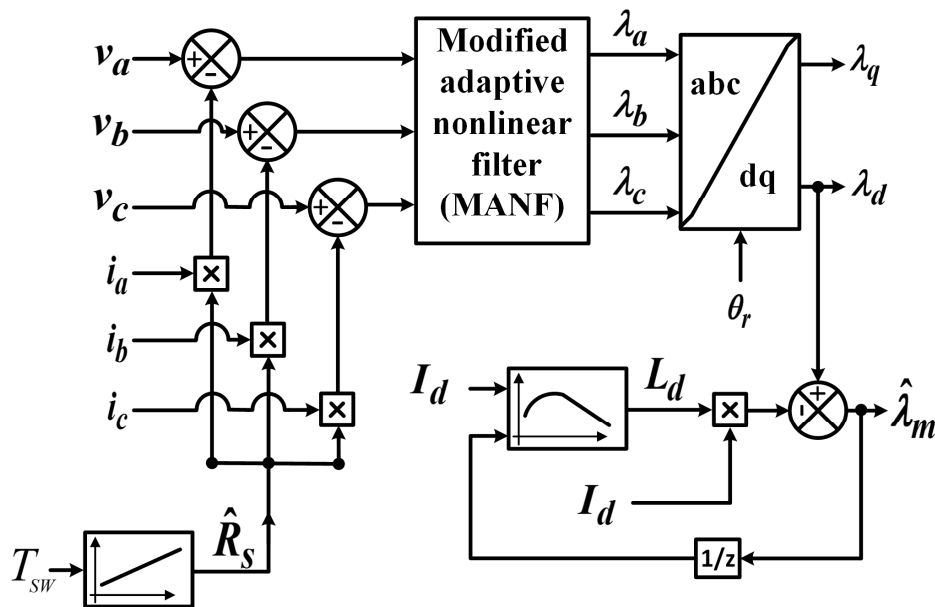
Fig. 3-1. Rotor flux linkage estimation scheme. T_{sw} is the stator winding temperature.

the resultant integrated signals together, the per phase air gap flux linkage is formed. A forward park transformation is then used to calculate the *dq*-axis flux linkages form the three phase values. Finally, the rotor flux linkage λ_m is estimated by subtracting the *d*-axis air-gap flux linkage from the *d*-axis stator flux linkage $L_d(I_d)\,I_d$. An inductance versus current measurement is done to account for the variation of *d*-axis inductance with *d*-axis current. This is done at different magnetization levels, and the results are incorporated in the estimation scheme as a look-up table as shown in Fig. 3-1.

It is known that dead-time in two level voltage source inverter introduces low order harmonics (6n±1, where n = 1,2,3,..) in the line and phase voltages and consequently in the machine currents [56] [61] [53]. Those harmonics need to be mitigated to prevent their interference with the flux harmonics. In principle, the severity of those harmonics depends mostly on the ratio between the dead-time and the switching time (1/switching frequency) [56]. This ratio times the DC bus voltage gives approximately the lost volt-second caused by dead-time, which needs to be added to the modulating signals for compensation [56]. For this chapter, the average value theory proposed in [56] is adopted for its simplicity and sufficient accuracy in mitigating those harmonics. All electrical parameters needed for dead-time compensation are shown in Table 3-1. However, if the proposed flux estimator is used for other applications, where a high lost volt-second is present either due to high switching frequency or high dead-time, this requires more effective dead-time compensation to ensure low order harmonics mitigation. More effective dead-time compensation techniques can be consulted in [53] [62].

A simulated result, using Matlab Simulink environment, of a 3µs dead-time, 5 kHz switching frequency, and 600 DC bus voltage at different motor speeds and full load is done to investigate the mitigation of the inverter low order harmonics with dead-time compensation. Fig. 3-2 shows the magnitude of the 6n±1 harmonics in dB versus rotor frequency with and without dead-time compensation. It can be clearly seen that those harmonics has been mitigated with dead-time compensation.
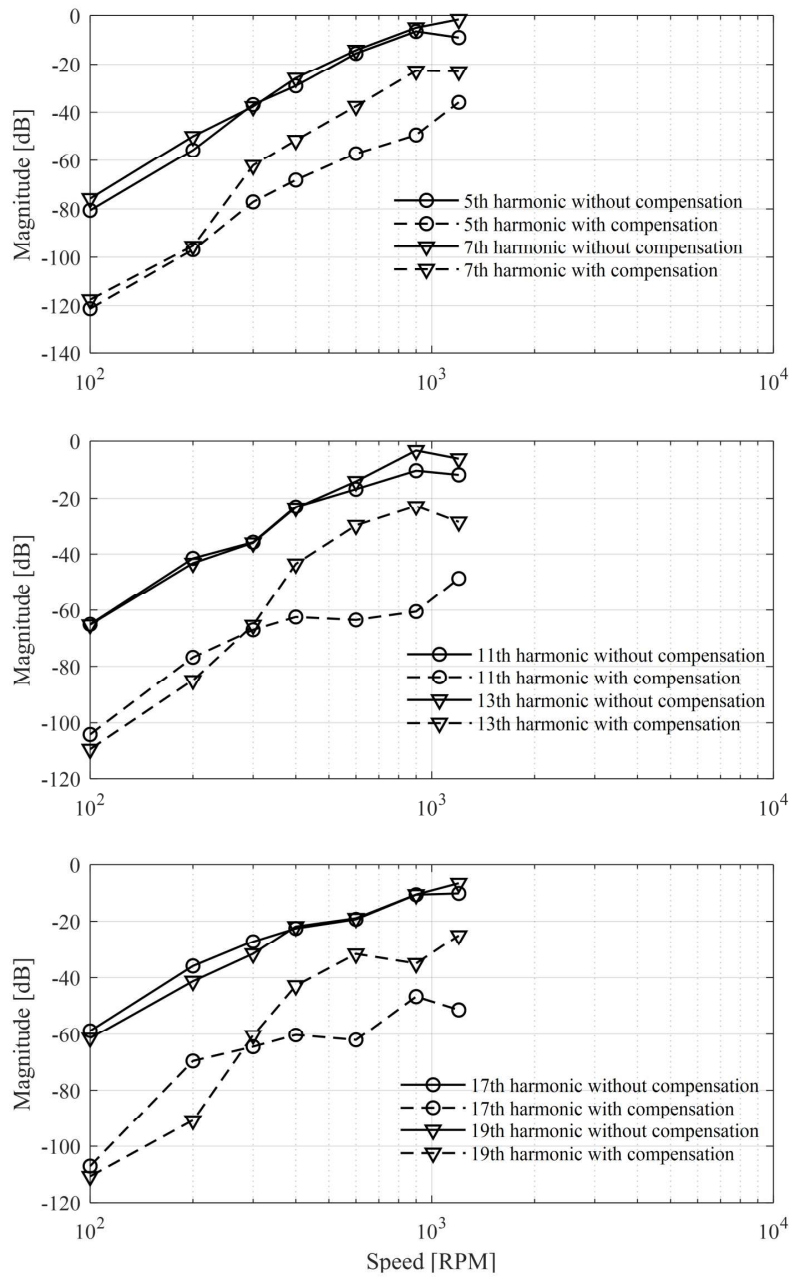
Fig. 3-2. Inverter harmonics in phase voltage at full load (10 A) without and with dead-time compensation.

Modified Adaptive Nonlinear Filter (MANF)

This section reviews the mathematical structure and properties of the main unit of the adaptive nonlinear filter (ANF) utilized to construct the amplitude, phase angle and frequency of a sinusoidal signal embedded in a distorted signal. This filter was first introduced in [63] to

25

Table 3-1. Typical electrical parameters of IGBT module
(from SEMITRANS M IGBT Module SKM 50 GB 123 D datasheet)

Turn on delay $t_{d(on)}$	70 ns
Rise time t_r	60 ns
Turn off delay $t_{d(off)}$	400 ns
Fall time t_f	45 ns
Switch control dead-time t_d	3 µs
Voltage drop across the IGBT (25ºC) V_{CEsat}	2.5 V
Voltage drop across the freewheeling diode (25ºC) V_d	1.85 V
Supply voltage range	0-750 V

eliminate the interference of a power line signal with an electrocardiogram (ECG) signal. Then, the same filter was employed in [64] to analyze the startup current of induction machines for broken rotor bars detection purposes. In this chapter, this filter is used to instantaneously construct the back emf signal with its associated harmonics from a very distorted switching signal for rotor flux linkage estimation purpose. In this section, a modification in the filter algorithm to improve its convergence speed and reduce its steady state error to make it suitable for electric drive applications is introduced.

Let $u(t)$ denote a distorted back emf signal comprising a number of desirable sinusoidal components and some undesirable components

$$u(t) = y_h(t) + e(t) \tag{3-1}$$

in which

$$y_h(t) = A_h sin(\omega_h t + \delta_h), \qquad h = 1,3,5,7,15,17,19 \tag{3-2}$$

are the sinusoidal components of interest, or in other words, the desirable harmonics that form the back emf signal. $e(t)$ is the total undesirable components including switching harmonics and noise. The goal of the algorithm is to estimate $y_h(t)$ from the input signal $u(t)$ as fast and as accurate as possible. The gradient descent method is used to minimize the least square error between the input signal $u(t)$ and the estimated desirable sinusoidal component $y_h(t)$ embedded in $u(t)$. The objective function is defined as

$$F(t, \theta_h) = [u(t) - y_h(t, \theta_h)]^2/2 \triangleq [e(t, \theta_h)]^2/2 \tag{3-3}$$

where θ_h is the parameters vector; the amplitude A_h, phase δ_h and frequency ω_h that defines the estimated signal $y_h(t)$.

$$\theta_h = [A_h, \omega_h, \delta_h] \tag{3-4}$$

The vector parameter θ_h is calculated using the gradient descent method so that the objective function tends to its local minimum by taking steps proportional to the negative of the gradient of the objective function [64]. The gradient descent method can be written as

$$\frac{d\theta_h(t)}{dt} = -\mu \frac{\partial[F(t, \theta_h(t))]}{\partial \theta_h(t)} \tag{3-5}$$

where μ is a $n \times n$ diagonal matrix consist of real positive constants regulating the step size of the gradient descent method [64]. This diagonal matrix μ controls the convergence speed and the steady state error of the algorithm [63], [64] [65].

Following the above steps, a set of differential equations [14] that governs the filter algorithm can be obtained as follows:

$$\dot{A}_h(t) = \mu_1 e(t) \sin \phi_h(t) \tag{3-6}$$

$$\dot{\omega}_h(t) = \mu_2 e(t) A_h(t) \cos \phi_h(t) \tag{3-7}$$

$$\dot{\phi}_h(t) = \mu_3 e(t) A_h(t) \cos \phi_h(t) + \omega_h(t) \tag{3-8}$$

$$y_h(t) = A_h(t) \sin \phi_h(t) \tag{3-9}$$

$$e(t) = u(t) - y_h(t), \tag{3-10}$$

where $\phi_h = \omega_h t + \delta_h$ is the total phase, and $e(t)$ is the total undesirable components present in $u(t)$ except the estimated component of interest $y_h(t)$. The dot on top of the parameters means differentiation with respect to time. Equations (3-6) to (3-10) form the main unit of the filter and are represented as a block diagram in Fig. 3-3.

The filter in its behavior of extracting a specific component presents a notch filter [64]. However, it is an adaptive in the sense that it takes into consideration the variations of the estimated signal $y_h(t)$ over time [64]. The convergence of the filter algorithm is mathematically proven in [64] and [65].
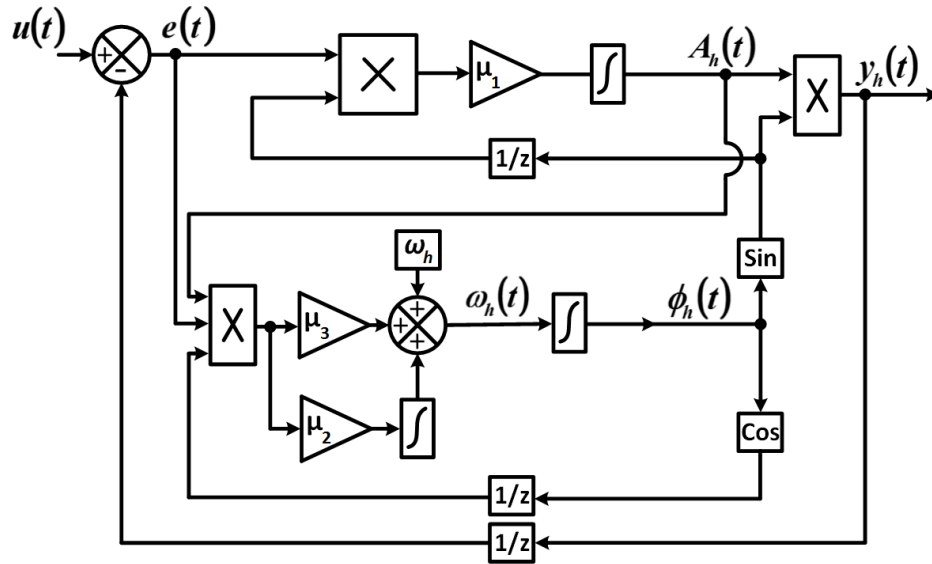
Fig. 3-3. Adaptive nonlinear filter *[64]*.

3.1.1 Filter Shortcoming and Modification

It was shown in [63] that the filter dynamics represented by the above differential equations, has a unique stable periodic orbit which lies in the neighborhood of the desired component $y_h(t)$. The extent of this neighborhood, however, depends on the level of "distortion" $e(t)$ and on the step sizes; mainly μ_1 [64] [65].

The level of distortion or the signal to noise ratio (signal means $y_h(t)$, and noise means all other components) can be improved by using a low-pass filter (LPF) to filter out the high-order harmonics, e.g., switching harmonics, from the input signal $u(t)$. The LPF does not need to be sophisticated, and it can be as simple as a second-order filter. Whatever is not removed by the LPF, will be removed by the ANF to produce a pure sinusoidal component which is $y_h(t)$. The LPF causes a known attenuation $|H(f)|$ and phase delay $\angle H(f)$. Since the ANF estimates the amplitude and the phase of the $y_h(t)$ in real-time, the attenuation and phase delay of the LPF can be restored as depicted in Fig. 3-4.

As for step sizes of the gradient descent method. The step sizes govern the convergence speed to the solution of the differential equations, and the steady state error of the solution [64].
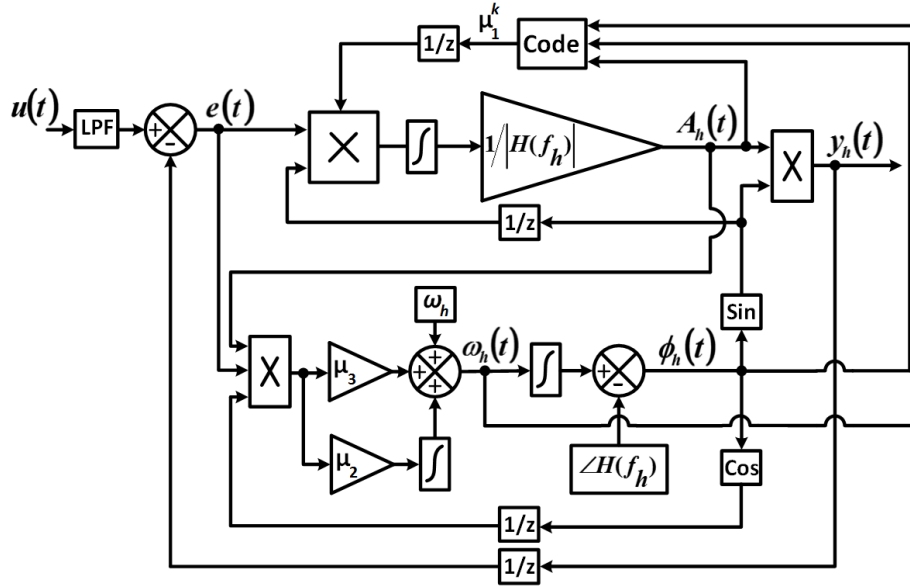
Fig. 3-4. Main unit of the modified adaptive nonlinear filter.

A small step size results in a refined periodic orbit in a tight neighborhood [64]. In other words, low steady-state error. On the other hand, the convergence speed to the solution is very slow. Large step sizes, however, result in a fast response with a higher steady-state error. A tradeoff, therefore, exists between the transient convergence speed and the steady- state accuracy [63] [64]. The objective is to have a fast response with an acceptable steady-state error. A fast response means, for instance, once the motor experiences a step or a ramp change in the frequency, the solution should be reached when the motor frequency reaches steady-state.

μ_2, and μ_3 step sizes together control the speed of the filter algorithm's transient response with respect to frequency variations of the estimated sinusoidal component $y_h(t)$ [63] [64]. They are the least sensitive step sizes in the algorithm [63] [64]. As a general rule, one can fix them to be unity, and the phase and the frequency of the estimated signal will converge as fast and as accurately as needed. Also, all initial conditions of integrators are set to zero.

μ_1, however, is the most sensitive step size in the algorithm. It controls the speed of the filter algorithm's transient response with respect to the amplitude variations of the estimated sinusoidal component $y_h(t)$ [63] [64]. Small values for μ_1 lead to a very slow convergence in the amplitude of the estimated signal $y_h(t)$ with a low steady-state error. In contrast, larger values of μ_1 lead to a fast response in the amplitude with a high steady-state error. This means

to overcome the tradeoff between the convergence speed and the steady-state error, step size μ_1 has to be varied.

In the literature, a lot of research has been done on how to choose the step-size for the gradient descent method. Following the result by Barzilai and Borwein [66], where their method of choosing the step size significantly improves the convergence of the standard gradient descent method. This method is motivated by Newton's method but does not involve any Newton's matrix or Hessian's matrix expensive computation [66]. The main idea is to use the information in the previous iteration to decide the step size in the current iteration.

For the gradient descent method,

$$A_h^{k+1} = A_h^k - \mu_1 g^k \tag{3-11}$$

where A_h^k and A_h^{k+1} are the solutions for the amplitude of the estimated signal at k and $k+1$ iterations, respectively. g^k is the gradient of the objective function at k iteration, and μ_1 is a fixed chosen value which needs to be varied to overcome the tradeoff between the convergence speed and the steady-state error of the estimated amplitude. For Newton's method [66],

$$A_h^{k+1} = A_h^k - (F^k)^{-1} g^k \tag{3-12}$$

where F^k is Newton's matrix, and it has the following property

$$F^k s^{k-1} = m^{k-1} \tag{3-13}$$

in which

$$s^{k-1} = A_h^k - A_h^{k-1} \tag{3-14}$$

and

$$m^{k-1} = g^k - g^{k-1}. \tag{3-15}$$

Newton's method ensures fast convergence to the solution [66]. However, the computation of F^k is expensive. The goal is to have $(\mu_1^k I) g^k$ approximate $(F^k)^{-1} g^k$ without computing F^k. In order to force the matrix $(\mu_1^k I)$ to have Newton's property, it is reasonable to require the following least-square problem [66]

$$(\mu_1^k)^{-1} = arg \min_{(\mu_1^k I)^{-1}} \frac{1}{2} \|(\mu_1^k I)^{-1} s^{k-1} - m^{k-1}\|^2 \tag{3-16}$$

from which

$$\mu_1{}^k = \frac{(s^{k-1})^T s^{k-1}}{(s^{k-1})^T m^{k-1}}. \tag{3-17}$$

Superscript T denotes a transpose. It is clear from equation (3-17) that the step size $\mu_1{}^k$ is varied with each iteration depending on the information from the current and previous iterations. Equations (3-14), (3-15), and (3-17) are coded as shown in Table 0-1 in the appendix and shown in the filter Fig. 3-4 as a box with a word "code" written inside it. This tuning of the step size μ_1 guarantees fast convergence of the amplitude of the estimated signal with low steady-state error. Fast response means, for instance, once the motor experiences a step or a ramp change in its frequency, a solution should be reached once the motor reaches steady state.

Fig. 3-5 shows the comparison between using fixed step sizes and the proposed variable step of μ_1 when the filter is extracting the amplitude of the imposed fifth harmonic of the back emf signal at the startup transient (from 0 to 60 Hz), 100% MS, and no load.
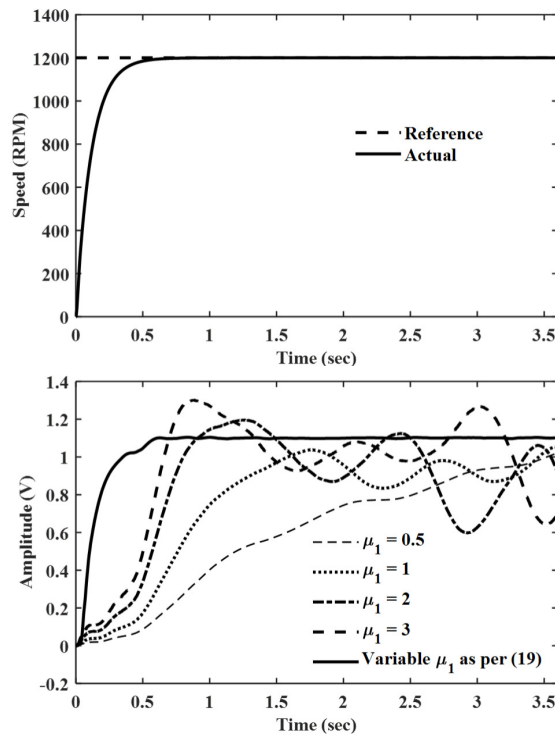
Fig. 3-5. The estimated amplitude of the fifth harmonic when the motor frequency undergo a step change from 0 to 60 Hz, or 0 to 1200 rpm (simulated result); comparison between fixed step sizes of μ_1 and a variable step size as proposed.

This comparison can also be seen in Fig. 3-6 and Fig. 3-7, where in Fig. 3-6 a fixed step size $\mu_1 = 3$ is used, and in Fig. 3-7 a variable step size is used. One can see that the orbits which the algorithm form as it reaches the solution intersect each other in Fig. 3-6, when a fixed step

31

size is used. This is because the amplitude of the signal is oscillating around the solution in the steady-state. However, this is not the case in Fig. 3-7, where a variable step size is used.
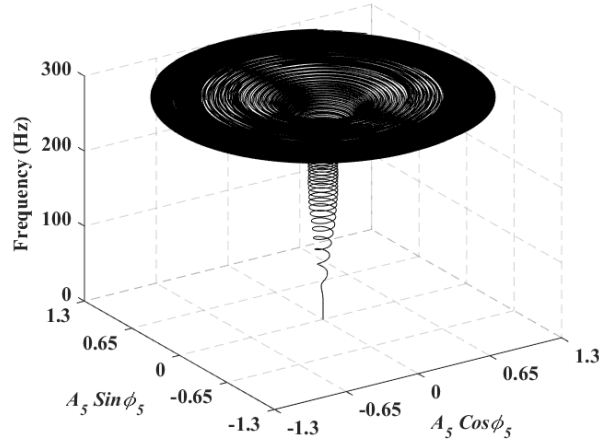
Fig. 3-6. Illustration of the algorithm's performance (simulated result) in extracting the fifth harmonic when the motor frequency undergo a step change from zero to 60 Hz with a fixed step size $\mu_1 = 3$.
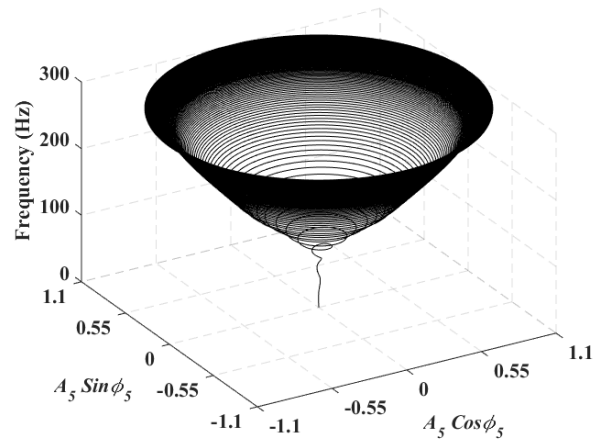
Fig. 3-7. Illustration of the algorithm's performance (simulated result) in extracting the fifth harmonic when the motor frequency undergo a step change from zero to 60 Hz with a variable step size μ_1.

To construct the back emf signal with its associated harmonics using the modified adaptive nonlinear filter (MANF), first one needs to know what type of harmonics exist in the original back emf signal of the motor. For this, a FFT analysis is done on the measured phase open circuit voltage of the machine while it is running as a generator unloaded at rated frequency (60 Hz) with fully magnetized magnets. Fig. 3-8 shows the harmonic spectrum of the measured open circuit phase voltage. The first major seven harmonics are considered in the estimation scheme, namely; fundamental, third, fifth, seventh, fifteenth, seventeenth, and

nineteenth. In order to achieve this, several filters are used, one for each harmonic as shown in Fig. 3-9.

(a)

(b)
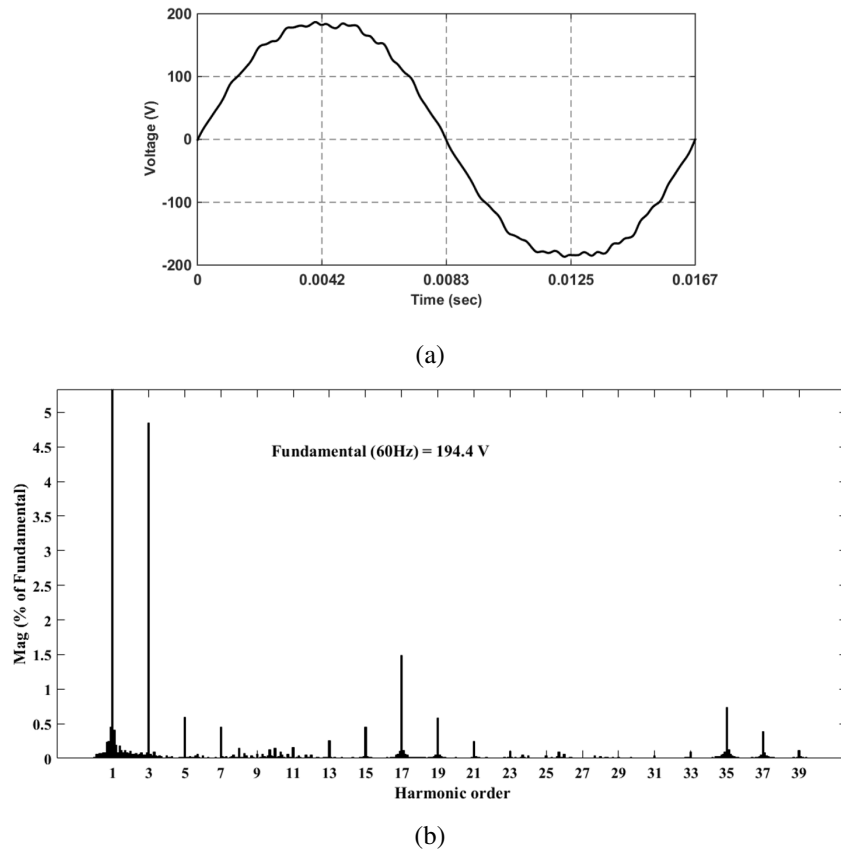
Fig. 3-8. (a) One electric cycle of the measured open circuit phase voltage at no-load and rated frequency (60 Hz), (b) Harmonic spectrum of the open circuit voltage in (a).
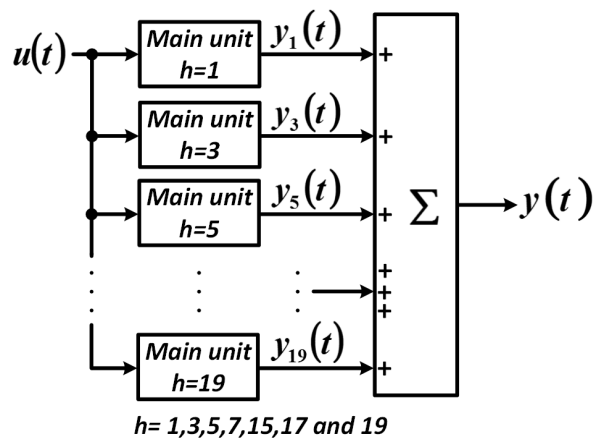
Fig. 3-9. Modified adaptive nonlinear filter.

To make the algorithm more motor independent, the open circuit voltage (OCV) test can be avoided if the finite element (FE) design file of the machine is available to the control design engineer. Fig. 3-10 shows the OCV signal of the machine running unloaded at rated frequency and 100% MS, with its harmonic spectrum. Fig. 3-10 depicts the same harmonic components seen in Fig. 3-8. Another approach is by excluding the known harmonics exist in the switching phase voltage of the machine, while it is running in motoring mode. For instance, the inverter causes high switching frequencies, and they can be excluded. Also, it is known that the even harmonics are eliminated by the symmetry of pulse width modulation (PWM) technique. What is left are the low order odd harmonics. If they appear in the phase voltage of the machine, this gives a high indication that they are a machine produced harmonics.
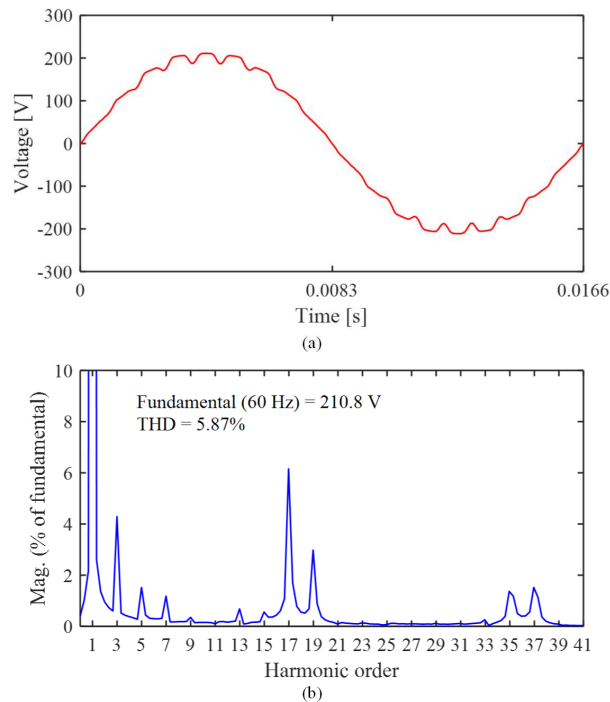
Fig. 3-10. (a) One electric cycle of the open circuit phase voltage at no-load and rated frequency (60 Hz) from finite element, (b) Harmonic spectrum of the open circuit voltage in (a).

Fig. 3-11 depicts the extraction of the amplitude and the total phase of the back emf fundamental component, when the motor is running unloaded at 60 Hz, and 600 DC bus. From Fig. 3-11, it can be seen that the algorithm takes a few cycles (less than 0.167 sec) to converge to the right amplitude and frequency of the extracted signal embedded into a distorted waveform.
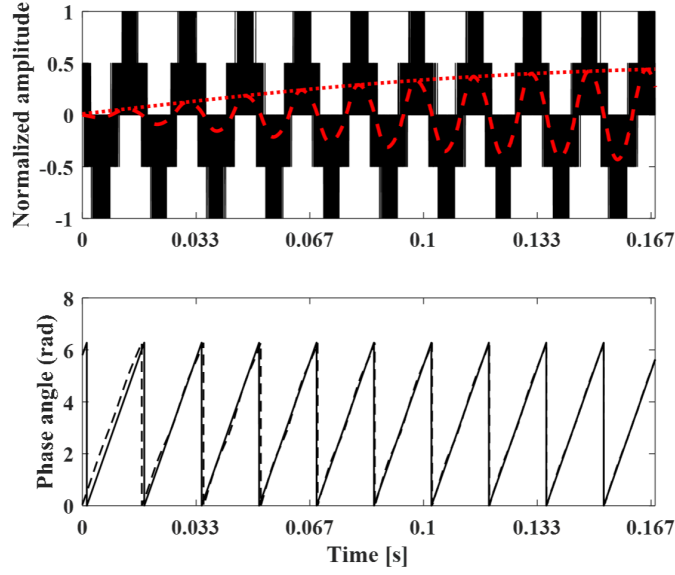
Fig. 3-11. Illustration of the convergence time taken to extract the back emf fundamental component using the filter algorithm. Top: input signal to the algorithm (solid), extracted back emf fundamental component (dashed), and its amplitude (dotted). Bottom: actual (solid) and extracted (dashed) phase angles.

Flux Linkage and *d*-Axis Inductance

3.1.2 Flux linkage

Once the phase back emf harmonics are extracted by using the MANF, each harmonic is integrated in order to get the corresponding air-gap flux linkage component, as per equation (3-18), where h denotes the harmonic order. Then, flux linkage components are added together to form the total phase air-gap flux linkage, as per equation (3-19).

$$\lambda_h(t) = \int y_h(t) \, . \, dt \tag{3-18}$$

$$\lambda(t) = \sum_{h=1,3,5,7,15,17,19} \lambda_h(t) \tag{3-19}$$

A forward park transformation is done on the resultant three phase air-gap flux linkage to *d*- and *q*-axis flux linkages. The rotor flux linkage λ_m is then estimated as per equation (3-20),

$$\lambda_m = \lambda_d - L_d(I_d) \, I_d, \tag{3-20}$$

where L_d and I_d are the *d*-axis inductance and the *d*-axis current, respectively. Here, the *d*-axis inductance is a function of *d*-axis current.

3.1.3   *d*-Axis inductance measurement

At the flux weakening region or for a maximum torque per ampere control scheme where *d*-axis current is not set to zero, the *d*-axis inductance versus *d*-axis current profile should be taken into account for accurate rotor flux linkage estimation.

Fig. 3-12 shows the electrical circuit for the test, where the rotor of the VFM is locked in the *d*-axis. DC current pulses with different current magnitudes up to the rated current are applied for a certain duration and recorded along with the corresponding DC voltage waveforms. At steady state the rate of change in the inductance is zero. Once the switch is open at $t = t_1$, the current starts decaying until it reaches zero at $t = t_2$. Hence the inductance is measured as follows [67], [68], and [69]

$$\int_{i_1}^{i_2} L\, di = \int_{t_1}^{t_2} (v - iR)\, dt. \tag{3-21}$$

The test is done at four different magnetization states. Fig. 13 shows the measured d-axis inductance versus d-axis current at 100%, 75%, 50%, and 25% magnetization states (MS), respectively. In general, the inductances decrease with current. Moreover, Fig. 3-13 depicts that the inductances are inversely proportional to the magnetization state as well. This is because in this VFM, the air gap is fairly small (0.4 mm) and the steel permeability is not negligible compared to air permeability. Therefore, as the flux increases, the steel saturates and the reluctance path of the magnetic circuit increases, hence, the inductance decreases.
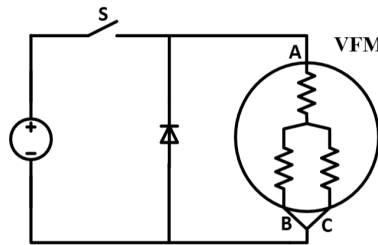
Fig. 3-12. Electrical circuit for inductance test.

Regarding the increase in the inductance at low currents, this can be explained by the following equation of the inductance,

$$L = \frac{\mu_0 \mu_r A}{N^2\, l}. \tag{3-22}$$
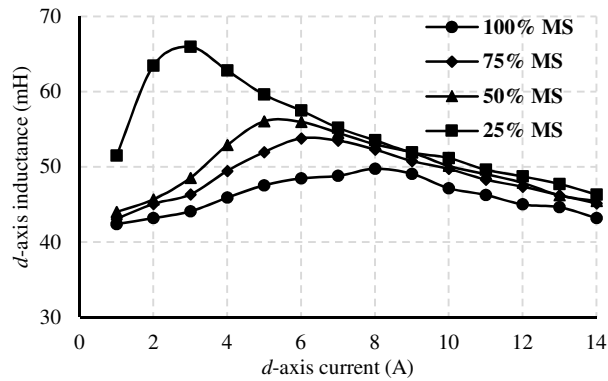
Fig. 3-13. Measured *d*-axis inductances versus *d*-axis current at different magnetization level.

In principle, air permeability μ_0, the area A, number of turns N^2, and the length of the magnetic path l are constant. Therefore, the inductance is proportional to the permeability of the steel μ_r, and somehow will have the same behavior of the steel permeability.

The permeability is the magnetic flux density over the magnetic field intensity. Fig. 3-14(a) shows the B-H curve of the steel M19G19, which is used in the machine. Fig. 3-14(b) shows the permeability versus the magnetic flux density. From Fig. 3-14(a), it can be seen that the permeability increases before saturation, and decreases in the saturation region.
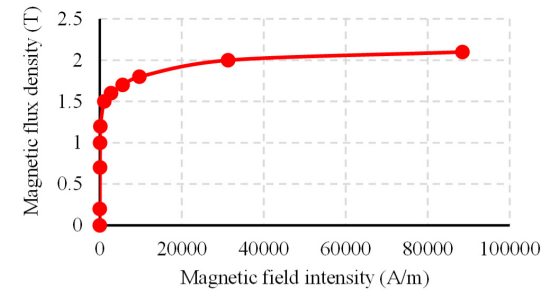
(a)
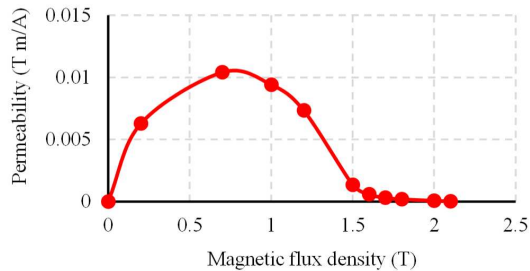
(b)

Fig. 3-14. (a). B-H curve of steel M19G19. (b) Permeability versus magnetic flux density of steel M19G19.

37

The same thing happens with the inductance. With increasing current up to 5 A, the d-axis stator flux enhances the magnet flux without driving the steel into saturation, which means the reluctance of the magnetic path decreases. Therefore the inductance increases. However, beyond 5 A, saturation occurs, which means the reluctance of the magnetic path increases. Therefore, the inductance decreases.

In this work the results are used as a look up table for more precise online estimation of rotor flux linkage. The d-axis inductance lookup table is two dimensional. First the inductance is selected with respect to the magnetization state as per Table 3-2. Then the inductance is selected based on its corresponding current as depicted in Fig. 3-13. The magnetization state (MS) is as per equation (3-23).

Table 3-2. First entry of inductance look-up table

Magnetization state (MS %)	Consider the curve of
$75 \leq MS < 100$	100 % MS
$50 \leq MS < 75$	75 % MS
$25 \leq MS < 50$	50 % MS
$0 \leq MS < 25$	25 % MS

$$MS\ (\%) = (\lambda_m/0.5) \times 100 \tag{3-23}$$

Regarding the harmonics introduced by the variation of dq-axis inductances with rotor positon, Fig. 3-15 shows the variation of d-axis inductance with rotor positon at rated machine current and 100% MS using finite element (FE) software. Two things are noteworthy over here.

First, the depicted inductance variations due to rotor position is 1.8% from the average inductance value (42.62 mH). This variation is small if compared with the main variation of the inductance with current (almost 19%). This is because of the utilization of fractional winding and a high ratio between the number of slots and the number of poles, which minimizes both the variation of dq-axis inductances with position and the cogging torque [70] [71]. However in some applications like wind power, machines of a high number of poles (small ratio of number of slots to number of poles) are used [72]. In such machines, the variation of dq-axis inductances with position can be quite significant. If the introduced harmonics by the inductance variation with position interferes with the flux harmonics, then the proposed

estimator might not be suitable to extract the flux harmonics. In this case another method should be developed or adopted.

Second, form Fig.15, it can be seen that in 120 mechanical degrees, the inductance variation waveform will repeat itself six times. And since the machine has six poles, this makes 120 mechanical degrees equals to 360 electrical degrees (one electric cycle). This means, the *d*-axis inductance variation with rotor position causes even harmonic of order 6n (n = 1,2,3,…) in the phase back emf waveform. However, the components of interest (the induced voltage harmonics) are of odd order as shown in Fig. 3-8 and Fig. 3-10. Therefore, the harmonics caused by the *d*-axis inductance variation with rotor position do not interfere with flux linkage harmonics.

Since the experimental results showed good tracking of rotor flux linkage and the resultant torque at steady state and during transients using the proposed filter algorithm as will be shown in the next section, the inductance cross coupling effect has been neglected in this work.
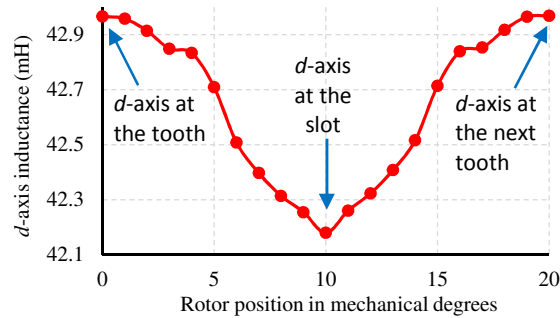
Fig. 3-15. *d*-axis inductance variation with rotor position at rated machine current and 100% MS.

Experimental Results

The VFM, which parameters are shown in Table 0-2 in the appendix, is driven by a two level inverter with a switching frequency of 5 kHz and 490 V DC bus voltage. A space vector pulse width modulation scheme is used to generate the switching signals to the inverter. This section is divided into six subsections as follows.

3.1.4 Back emf extraction during startup transient

In this subsection, a step change in motor frequency is applied from zero to 60 Hz, or from zero to 125.6 rad/sec, at no-load, and the machine is fully magnetized, as shown in

Fig. 3-16. The purpose of this is twofold. First, is to see the extraction of the back emf harmonics at the startup transient. Second, is to compare the total extracted phase back emf signal in steady-state with that of the open circuit phase voltage of the machine when it is running as generator at the same operating conditions of speed, magnetization state, and no-load. The comparison is done in both the time domain and frequency domain.
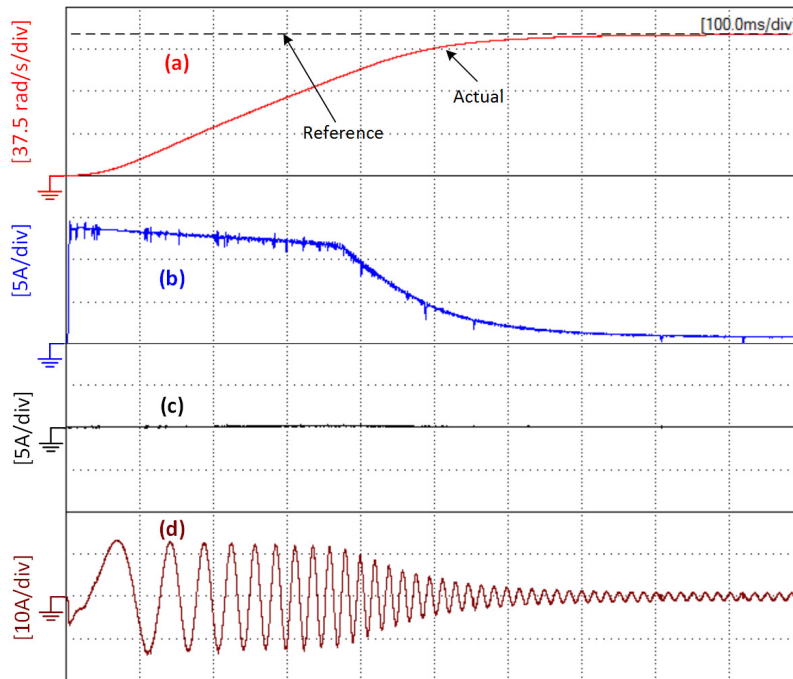
Fig. 3-16. A step change in motor frequency from 0 to 60 Hz (0 to 125.6 rad/s). (a) Reference and actual speed. (b) q-Axis current. (c) d-Axis current. (d) Machine current (i_a).

Fig. 3-17 illustrates filter dynamics in extracting the amplitude and phase of the fundamental component of the back emf signal during the startup transient. The amplitude of the extracted signal converges quickly and is able to follow the changes in the amplitude of the embedded signal with almost negligible steady-state error. Moreover, Fig. 3-18 depicts the extraction of the third, fifth, and seventh harmonics along with the total extracted phase back emf signal. In a similar manner, all the other harmonic components are extracted. A time domain comparison between the total extracted phase back emf in motoring mode using the MANF and the open circuit phase voltage of the machine in generation mode running at the same operating conditions for a half electric cycle is shown in Fig. 3-19. Fig. 3-20, however, shows the comparison in the frequency domain. Fig. 3-21 shows the estimated rotor flux linkage λ_m during the startup transient, where it rises to almost 0.495 V.s, with a 1% error from the measured average rotor flux linkage in the generation mode (0.5 V.s).
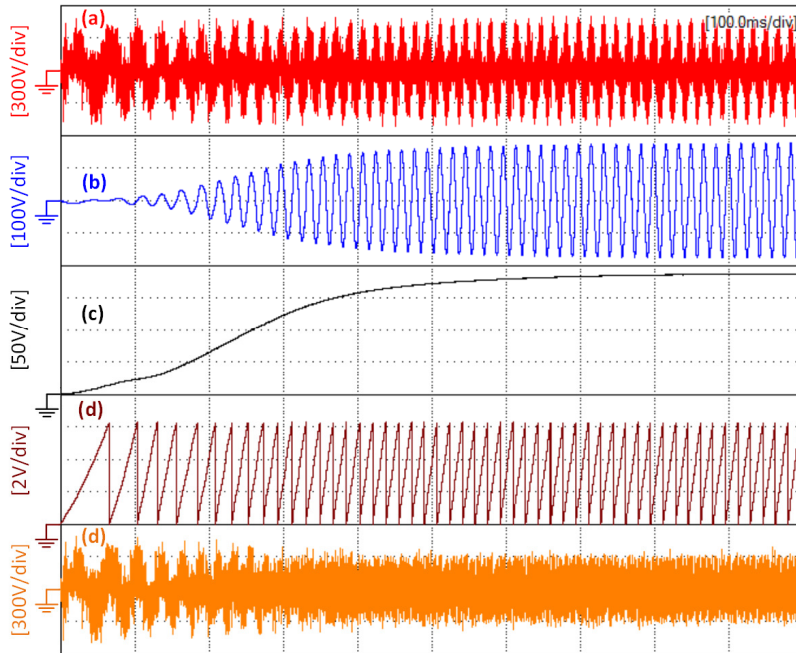
Fig. 3-17. Illustration of the filter performance in extracting the back emf fundamental component during the startup transient. (a) The phase back emf switching signal, the input signal to the filter algorithm $u(t)$. (b) The extracted back emf fundamental component. (c) The estimated amplitude of the fundamental. (d) The estimated phase of the fundamental. (e) The input signal after extracting the fundamental, the error signal $e(t)$.
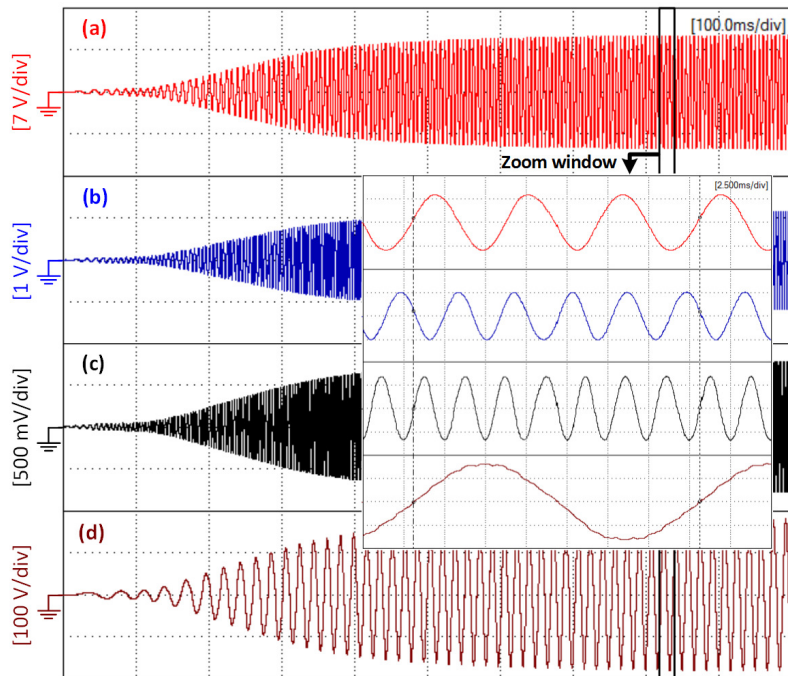
Fig. 3-18. Some of the extracted harmonics along with the total estimated back emf. (a) The third harmonic $y_3(t)$. (b) The fifth harmonic $y_5(t)$. (c) The seventh harmonic $y_7(t)$. (d) The total estimated back emf $y(t)$.

41
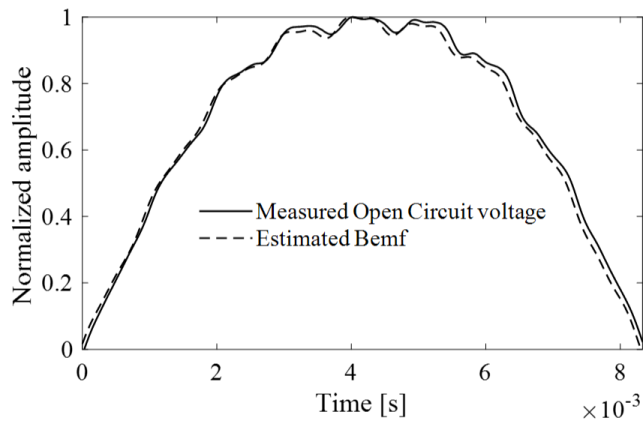
Fig. 3-19. Time domain comparison for a half electric cycle between the extracted phase back emf $y(t)$ using the MNAF and the open circuit phase voltage at the same operating conditions of 60 Hz, no-load and full magnetization state.
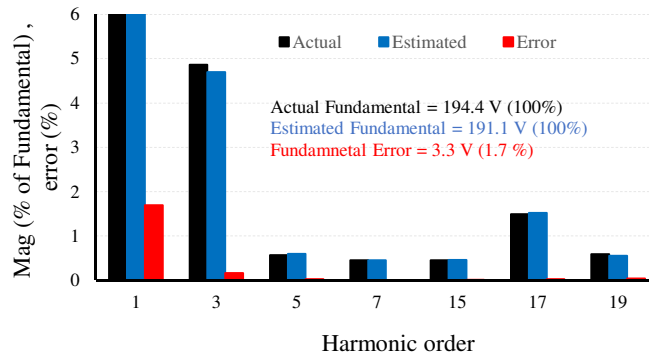
Fig. 3-20. Frequency domain comparison between the estimated back emf harmonics and their corresponding harmonics of the open circuit phase voltage at 60 Hz, no-load and full magnetization state.
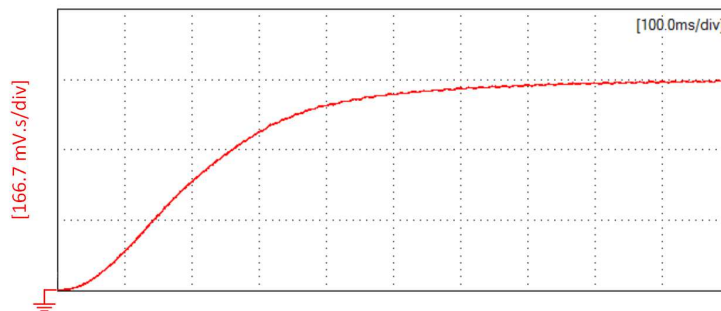
Fig. 3-21. The estimated rotor flux linkage λ_m during startup.

3.1.5   Rotor flux linkage at nominal load

Fig. 3-22 shows the estimated rotor flux linkage at full load, 450 rpm, and 100% MS. The magnets are considered fully magnetized at 0.5 V.s. However, at full load as seen in Fig. 3-22, the estimated rotor flux linkage is almost 0.475 V.s. This is due to armature reaction. Fig. 3-22(f) shows the estimated torque using the proposed scheme in comparison with the measured torque and the estimated torque using a lookup table as in [17]. The proposed estimator showed an error of almost 2.5% from the average measured torque value. However, the error in estimated torque using the flux from the lookup table is almost 16%. This is because the lookup table method does not account for magnet's demagnetization due to armature reaction. Also, from the measured torque in Fig. 3-22(f), it can be seen that the machine has high torque ripple.
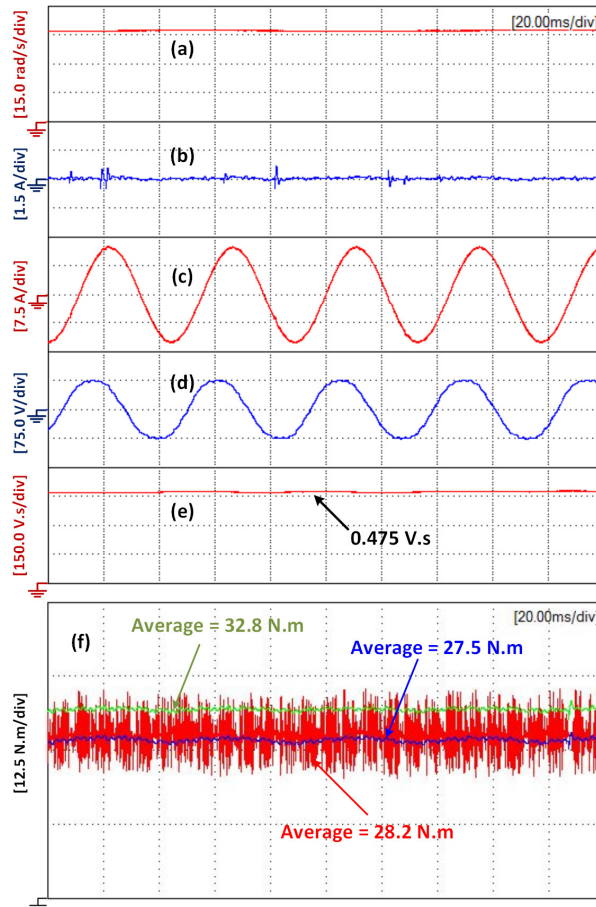
Fig. 3-22. Rotor flux linkage estimation at full load, 100% magnetization state, and 450 rpm (47 rad/s). (a) Motor speed. (b) d-axis current. (c) Machine current (i_a). (d) Total estimated back emf. (e) Estimated rotor flux linkage using the proposed algorithm. (f) Measured torque (red trace), estimated torque using the estimate flux by the proposed scheme (blue trace), and estimated torque using the estimated flux using a lookup table (green trace).

3.1.6 Rotor flux linkage during torque transient

Fig. 3-23 shows the dynamic response of a torque control using FOC ($i_d = 0$) scheme. A step change in load torque is applied from 1 N.m to 12 N.m when the machine is running at 425 rpm. Fig. 3-23(e) clearly depicts the dynamics of the filter algorithm in estimating the rotor flux linkage during torque transient. The torque transient response in Fig. 3-23(g) is mainly governed by the transient response of q-axis current. However, once the machine torque reaches steady-state, the superiority of the proposed algorithm is clearly evident. Fig. 3-23(h) shows that the estimated torque using the rotor flux from the proposed algorithm has an error of 2.5% from the measured average torque value, whereas the estimated torque using the flux from the lookup table has a 29% error. Despite having high torque ripple, the proposed filter algorithm still demonstrates good performance in tracking the rotor flux linkage and the resultant output torque.

3.1.7 In comparison with the fundamental

Fig. 3-24 shows the comparison between the estimated torque using the proposed algorithm and by using the fundamental back emf component only, during a ramp change in load torque from 0 to 17 N.m. It can be seen that when using the back emf harmonics, the estimated rotor flux linkage and the resultant torque are slightly higher than the ones when the fundamental back emf is used. The steady state result of the measured and estimated torques depict 1.57% error in the estimated torque using the flux from the proposed algorithm versus 2.6% error in the estimated toque using the flux from the fundamental component only. This comes to almost 1% improvement in the error. This improvement is expected to be even slightly higher if the rest of the harmonics are included in the algorithm. Actually, this result is expected since the RMS value of the total back emf is higher than the back emf fundamental component.

3.1.8 Rotor flux linkage during magnetization transient

This subsection presents the response of the filter during the magnetization transient. While the machine is driven unloaded at 60 Hz (125.6 rad/sec), a negative 6.8 A d-axis current pulse is excited for 50 msec as shown in Fig. 3-25. The total extracted back emf $y(t)$ and the estimated rotor flux using the MANF during the demagnetization process are also shown in Fig. 3-25. After this operation, the machine is brought to a standstill and run as a generator with the help of the dynamometer unloaded at 125.6 rad/sec. The average rotor flux was measured

from the open circuit voltage and the speed, and it is indicated as dashed line in Fig. 3-25(d). This shows 0.43% error between the estimated and the measured values of rotor flux linkage.
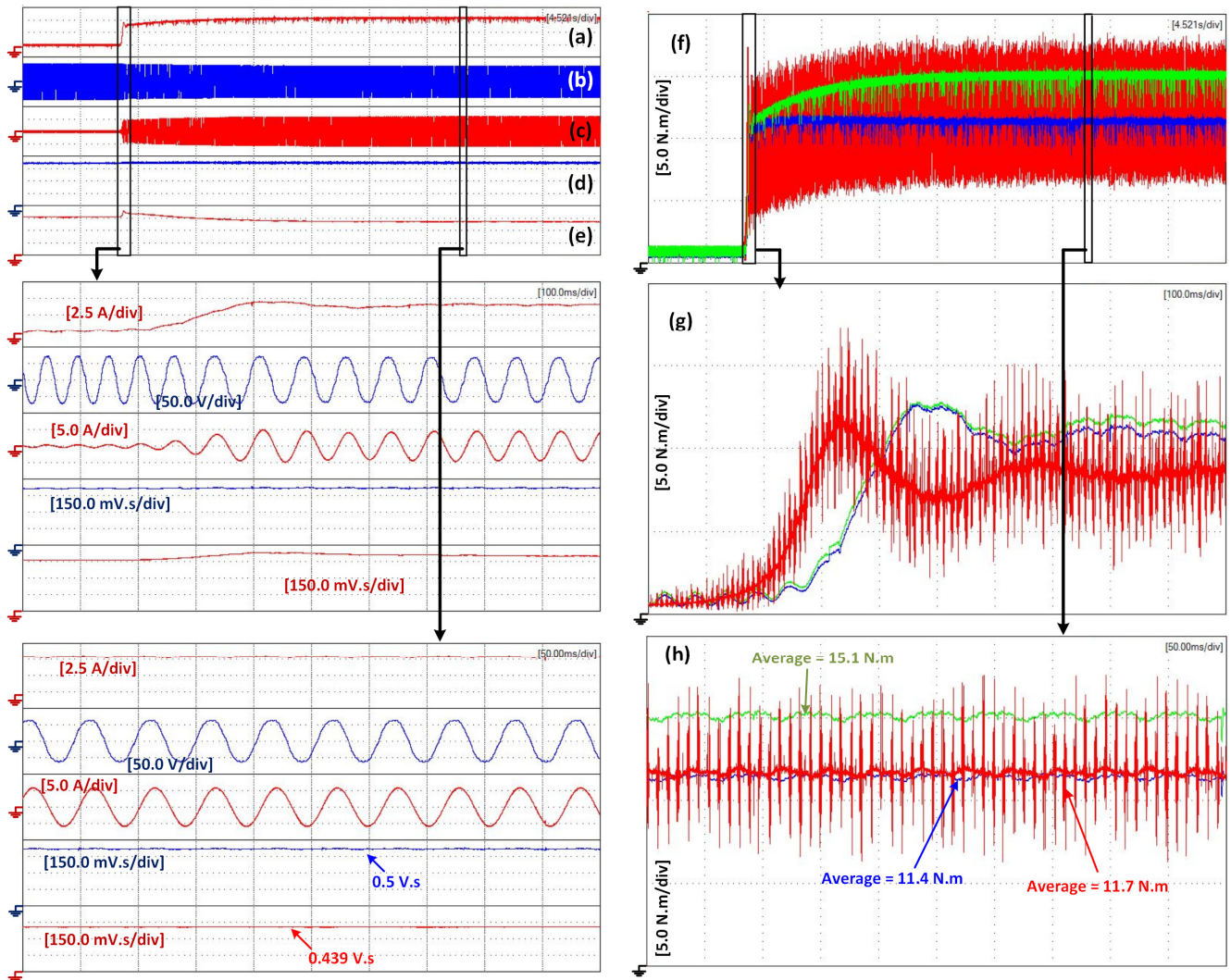
Fig. 3-23. Illustration of the filter dynamics during a step change in load torque. (a) q-axis current. (b) The total estimated back emf signal. (c) Machine current (i_a). (d) The estimated rotor flux linkage using a lookup table method. (e) The estimated rotor flux linkage using the proposed method. In (f) , (g), and (h), the red trace is the measured torque, the blue trace is the estimated torque using the estimate flux form the proposed scheme, and the green trace is the estimated torque using the estimated flux from a lookup table.

3.1.9   Operating with continuous negative d-axis current

The proposed scheme is also tested with continuous negative d-axis current being injected. The d-axis current is ramped from zero to negative 6 Amperes in almost six seconds, while the machine is running unloaded at constant speed of 125.6 rad/sec as it is seen from Fig. 3-26. The total extracted back emf $y(t)$ and the estimated rotor flux linkage are also shown

45

in Fig. 3-26. The error between the estimated and the measured (dashed line) values of rotor flux linkage in this operation is around 0.97 % as per Fig. 3-26(e). Fig. 3-27 shows the experimental setup.
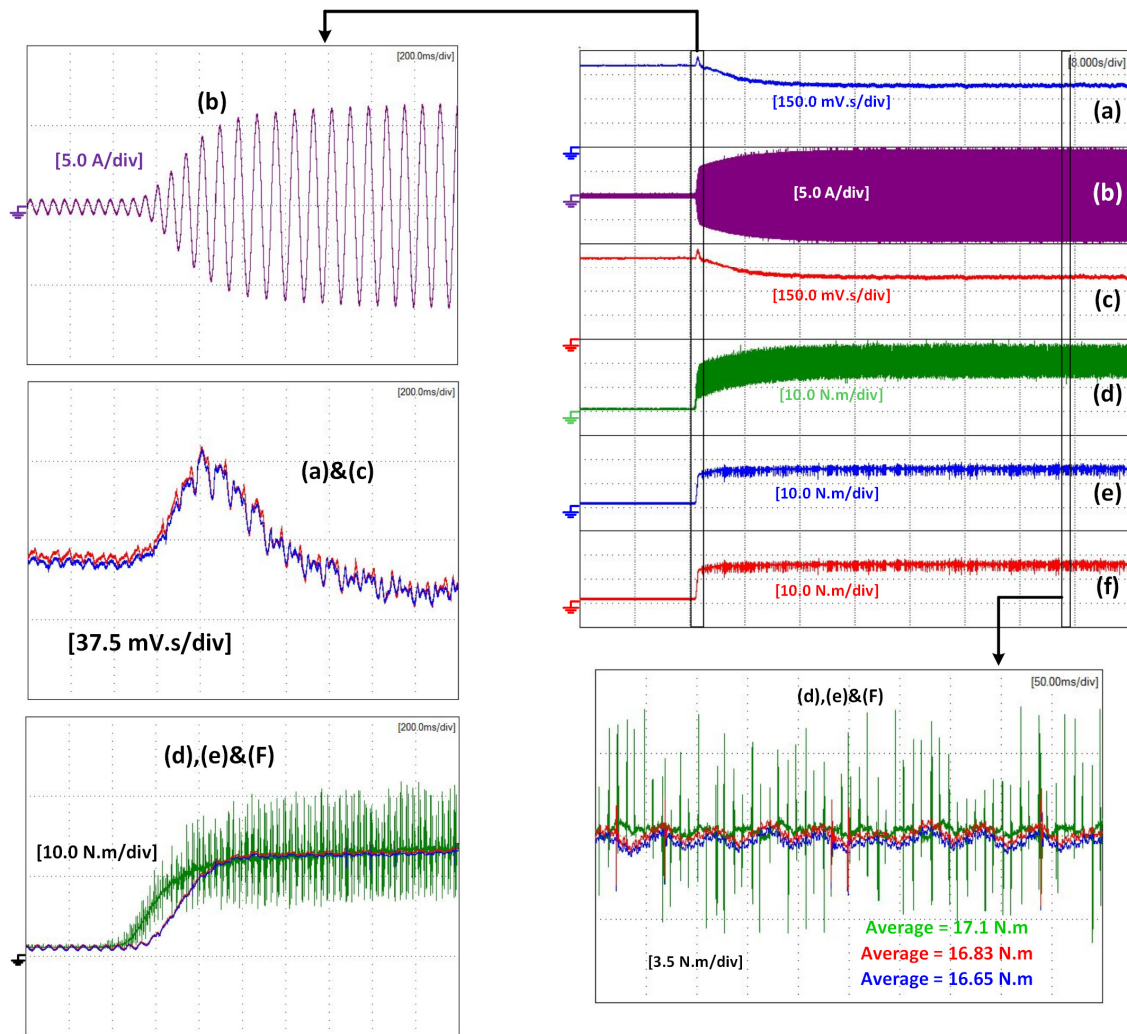
Fig. 3-24. Illustration of the filter dynamics during a ramp change in load torque. (a) Estimated rotor flux linkage using the fundamental component. (b) Machine current i_a. (c) Estimated rotor flux linkage using the proposed algorithm. (d) Measured torque. (e) The estimated torque using the fundamental. (f) The estimated torque using the proposed algorithm.
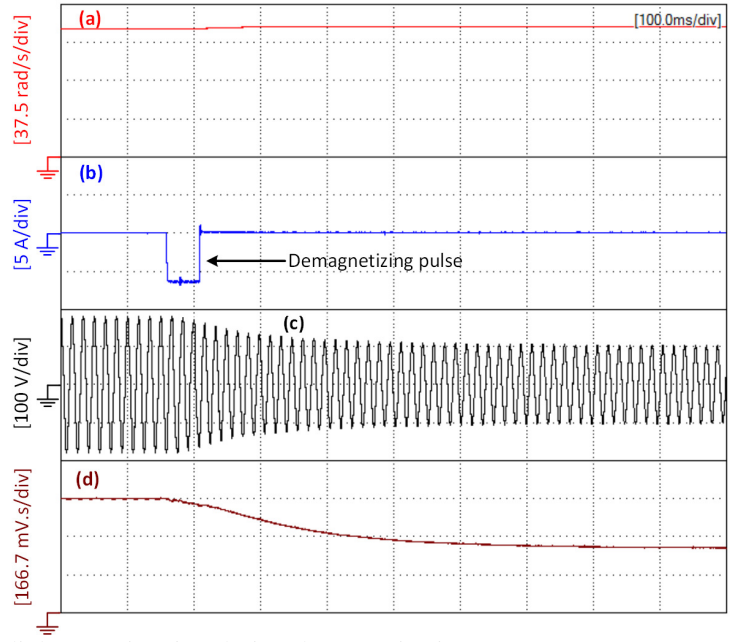
Fig. 3-25. Rotor flux linkage estimation during demagnetization process. (a) Motor speed. (b) *d*-axis current. (c) Total estimated back emf. (d) Estimated rotor flux linkage.
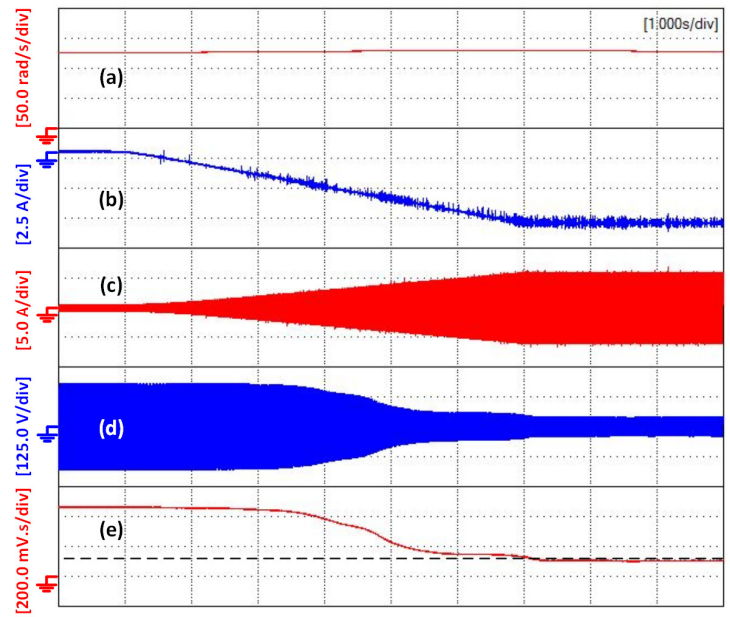
Fig. 3-26. Testing the algorithm with negative d-axis current operation. (a) Motor speed. (b) *d*-axis current. (c) Machine currant (i_a). (d) Total extracted phase back emf signal. (e) Estimated rotor flux linkage.
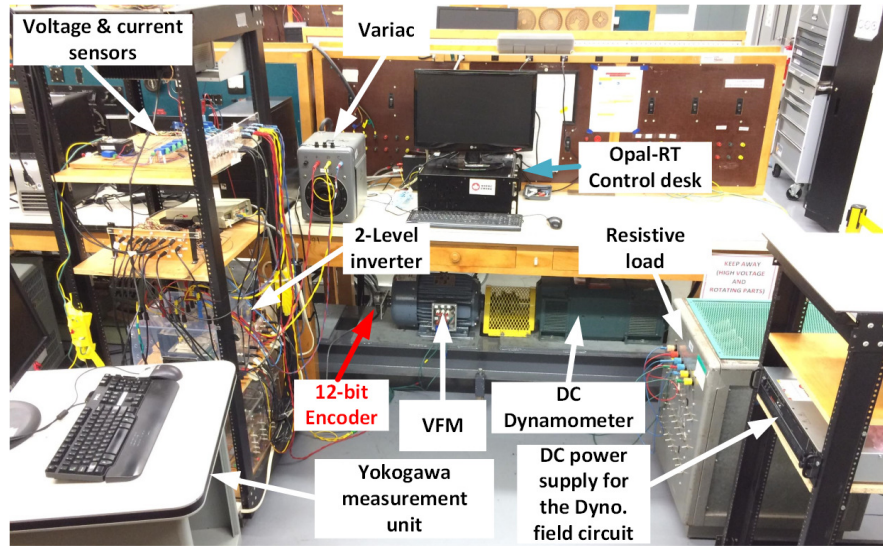
Fig. 3-27. Experimental setup.

Summary

An improvement to an existing nonlinear adaptive filter algorithm which is able to extract a time and frequency varying sinusoidal signal embedded within a nonstationary waveform has been introduced. The improvement comes in a form of overcoming the tradeoff between the convergence speed and the steady-state error of the filter algorithm by adopting a variable step size μ_1 based on Barzilai and Borwein method instead of manually choosing it by trial and error method.

This is then applied to extract the back emf phase voltage harmonic components of a variable flux machine from the inverter phase switching signal with the aim of estimating the varying rotor flux linkage.

Compared to the existing methods for rotor flux linkage estimation, this does not need any voltage or current signal injection into the stator winding. The method has been experimentally validated and has shown good performance in predicting the rotor flux linkage during the normal run time and during the torque and magnetization transients.

Moreover, it is noteworthy that the proposed scheme is effective when there is a quite small cogging torque, negligible eccentricity, and high back emf over distorted voltage due to inverter nonlinearity.

Chapter 4.   Operating Envelopes of the Variable Flux Machine with Positive Reluctance Torque

Introduction

Motors with a high torque per volume ratio and with a high efficiency over a wide speed range are preferred for electrified transportation. This is why the interior permanent magnet synchronous machines (IPMSMs) are the choice for many electric vehicles. However, due to the limited DC supply voltage, a flux weakening regime has to be utilized beyond the base speed to counter the growing back electromotive force and to expand the operating limits within the inverter capacity. This is done by injecting a continuous negative d-axis current to weaken the air-gap flux linkage [73]. This current causes copper loss, especially when cruising at high speed for extended periods. This issue is addressed by using variable-flux interior permanent magnet synchronous machines (VFIPMSMs), where the magnetization state (MS) of the low coercive magnets can be lowered irreversibly to a certain level, depending on the operating point in the torque-speed envelope, via a short d-axis current pulse, which eliminates the continuous use of d-axis current in the flux weakening region [74].

Since the permanent magnets utilized in VFIPMSMs are of low-coercivity (low-H_c) [74] [75], the MS can be manipulated easily and as needed to achieve better motor efficiency [76]. This, and the independency of rare-earth permanent magnets, are the key features of the VFIPMSMs. With the ease of MS manipulation (low-H_c) comes the subjectivity of magnet demagnetization to load current [13], which decreases the machine torque capability in the loading condition [74]. To avoid this issue, a positive d-axis current is needed to maintain a high MS in the loading conditions. However, in normal saliency IPMSMs, this current generates a negative reluctance torque, which reduces the overall machine torque. This issue has been addressed in [77] and [78] by designing an inverted-saliency type VFPIMSMs (IS-VFIPMSMs). Also, they are known as flux-intensifying (FI) VFIPMSMs [77]. In this work, the term IS-VFIPMSM will be used as it is more precise than the term FI-VFIPMSM.

However, and in contrast to IPMSMs, the IS-VFIPMSMs experience a negative reluctance torque in the flux weakening region. This and the irreversible demagnetization of the low-H_c magnets by a negative d-axis current reduces the overall torque of the IS-

VFIPMSMs in the flux weakening region. Consequently, the output power of the IS-VFIPMSMs deteriorates, compared to IPMSMs, in the flux weakening region [79]. This issue has being addressed by utilizing different parallel and/or series combinations of high- and low-coercivity permanent magnets providing a variable amount of rotor flux linkage, as in [80] and [81]. While both configurations (parallel and series) improve the overall high-speed torque capability of the IS-VFIPMSMs, only the series configuration is reported to improve the high-speed motor power capability [81] [82].

The objective of this chapter is twofold. First, to investigate the possible operating envelopes of the IS-VFIPMSM within the machine and inverter electric constraints. Also, to provide an analytical solution of the operating point trajectory (i_d, i_q) in each operating control scheme on the operating envelopes considering the irreversible demagnetization property of the low-H_c magnets with negative d-axis current. Second, to examine the effect of saliency on the output power of the IS-VFIPMSM. This study is valid for any type of VFIPMSMs including but not limited to IS-VFIPMSMs (parallel and/or series configuration). The laboratory experiments are done on a 5 hp IS-VFIPMSM using AlNiCo 9 permanent magnets, which was introduced in [78]. The rotor/magnet flux linkage is estimated online using the proposed estimator in Chapter 3. The effects of saturation and cross coupling on the operating envelopes of the VFIPMSM are not discussed in this work. Also, the ohmic loss is neglected since VFIPMSMs are used in the high-speed region where the voltage drop over the stator resistance is relatively small.

In addition, a comparative study between the IS-VFIPMSM and an equivalent IPMSM in terms of torque and power capabilities, iron and copper losses, efficiency, and speed range is presented in this chapter using simulated and finite element (FE) results. The comparative study lacks experimental results of the equivalent IPMSM due its unavailability in the lab at this moment.

Basic Equations of a VFIPMSM

The steady-state voltage equations of the three-phase VFIPMSM in the dq-synchronous-rotating frame neglecting the resistance drop are [73]:

$$\begin{bmatrix} v_d \\ v_q \end{bmatrix} = \begin{bmatrix} 0 & -\omega L_q \\ \omega L_d & 0 \end{bmatrix} \begin{bmatrix} i_d \\ i_q \end{bmatrix} + \omega \begin{bmatrix} 0 \\ \lambda_m(i_d) \end{bmatrix} \tag{4-1}$$

where

v_d, v_q d- and q-axis armature voltage components,

i_d, i_q d- and q-axis armature current components,

L_d, L_q d- and q-axis armature self-inductance components,

ω rotor electrical angular velocity,

$\lambda_m(i_d)$ magnet/rotor flux linkage as a function of d-axis current.

This is called the lossless model. The phasor diagram is shown in Fig. 4-1 for $i_q > 0$ and $i_d < 0$. The induced torque (T) is given by

$$T = 3P\left[i_q\,\lambda_m(i_d) + \left(L_d - L_q\right) i_d i_q\right]/2$$

(4-2)

$$= 3P\left[I_a\cos(\beta)\,\lambda_m(i_d) + \frac{1}{2}\left(L_q - L_d\right) I_a^2 \sin(2\beta)\right]/2,$$

where $I_a = \sqrt{i_d^2 + i_q^2}$, $\beta = \tan^{-1}\left(-i_d/i_q\right)$, and P is the number pole pairs [83]. β is the angle between the armature current vector I_a and the q-axis.
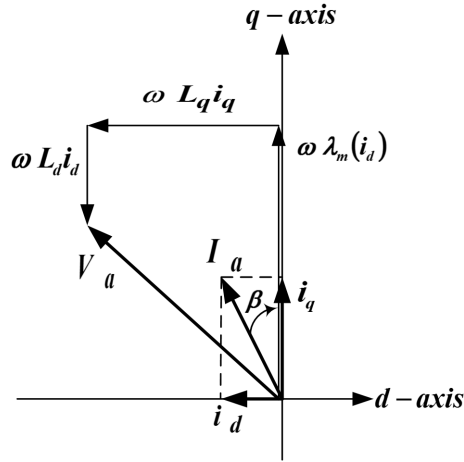
Fig. 4-1. Voltage and current vectors in the (i_d, i_q) plane [83].

The input/output power and the terminal motor voltage V_a are given as follows:

$$P_{in} = 3\left[v_q i_q + v_d i_d\right]/2$$

(4-3)

$$P_{out} = T\omega_m$$

(4-4)

$$V_a = \sqrt{\left(-\omega L_q i_q\right)^2 + \left(\omega L_d i_d + \omega\,\lambda_m(i_d)\right)^2},$$

(4-5)

where ω_m is the rotor mechanical speed in radian per second [73].

The permanent-magnet flux which links the stator coils, or the rotor flux linkage (λ_m) is a function of the d-axis current. Fig. 4-2 depicts the measured change in the AlNiCo9 magnet flux linkage with d-axis current in the second quadrant. This phenomenon is modeled by the following third order polynomial

$$\lambda_m(i_d) = a_3 i_d^3 + a_2 i_d^2 + a_1 i_d + a_0, \qquad (4\text{-}6)$$

where the coefficients are obtained from the curve fit, and their values are shown in Table 0-3 in the appendix. Those coefficients are magnet type and design dependent. Therefore, for each type of magnet and design used in a VFIPMSM, there are specific values for those coefficients. $\lambda_m(i_d)$ is considered constant (λ_m) when operating in the first quadrant of (i_d, i_q) plane, as the magnets can only be demagnetized by a negative d-axis current. Moreover, the magnets are considered fully magnetized at the initial startup.
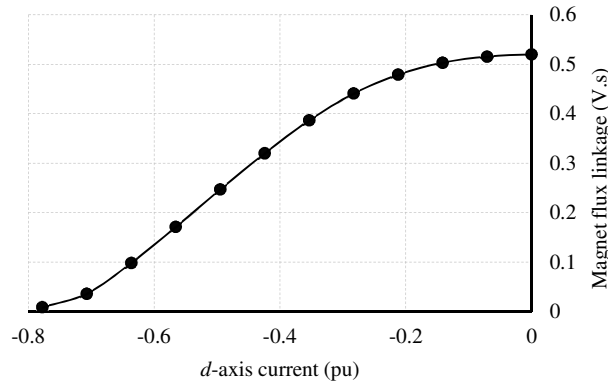
Fig. 4-2. Measured AlNiCo9 magnet flux linkage versus d-axis current.

The inverter is sized to deliver the continuous rated motor current (I_s). The terminal voltage limit (V_s) is decided by the maximum available voltage from the inverter. This depends on the utilized pulse width modulating scheme. Therefore, the motor current (I_a) and the terminal voltage (V_a) are limited as follows [83]:

$$I_a \leq I_s \qquad (4\text{-}7)$$

$$V_a \leq V_s. \qquad (4\text{-}8)$$

From Fig. 4-1and equation (4-7), the current limit circle is represented by [83]

$$i_d^2 + i_q^2 = I_s^2 \tag{4-9}$$

and from equations (4-5) and (4-8), the voltage limit ellipse is represented by [83]

$$\left(L_q i_q\right)^2 + [L_d i_d + \lambda_m(i_d)]^2 = (V_s/\omega)^2. \tag{4-10}$$

An explanatory representation of the current limit circle and voltage limit ellipse in the (i_d, i_q) plane for an IS-VFIPMSM is shown in Fig. 4-3. As the speed increases, the voltage limit ellipse shrinks [84]. The voltage limit ellipse for the VFIPMSMs is not a perfect ellipse, as seen in Fig. 4-3. This is because of the demagnetization property of the low-H_c magnets with a negative d-axis current. For an arbitrary armature current vector $\boldsymbol{I}_a$ (i_d, i_q) satisfying both the limiting conditions given by (4-7) and (4-8), must be within both the current limit circle and the voltage limit ellipse [84]. For instance, in Fig. 4-3 at $\omega = \omega_x$, the allowable current vector is inside the hatched area UVWXYZ.
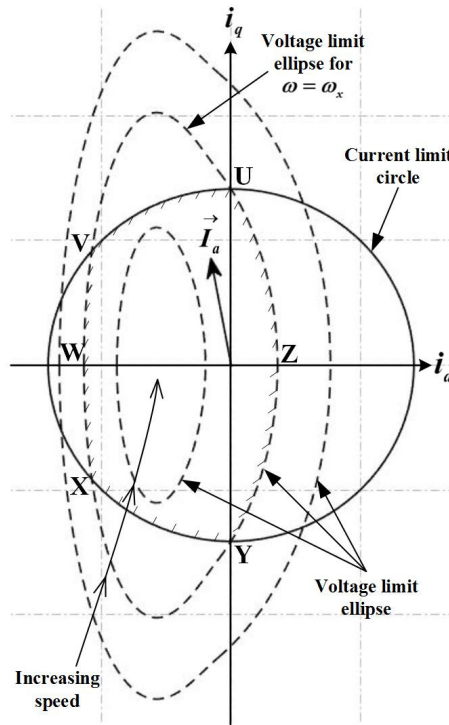
Fig. 4-3. Voltage and current limits for IS-VFIPMSM.

Below the base speed, maximum torque per ampere (MTPA) control is used to maximize the torque for a given current magnitude [83] [84]. Because of the inverted saliency ($L_d > L_q$) of the IS-VFPMSM, the MTPA trajectory is in the first quadrant of the (i_d, i_q) plane.

Consequently, the reluctance torque of the IS-VFIPMSM, unlike in the normal-saliency IPMSM, assists the magnet torque in the first quadrant of the (i_d, i_q) plane. In order to obtain a maximum magnet torque below the base speed, the low-H_c magnets are kept fully magnetized.

To achieve a MTPA, the desired angle β is obtained by differentiating (4-2) with respect to β which results in [83] [84]

$$\beta_0 = sin^{-1}\left[\frac{\lambda_m - \sqrt{\lambda_m^2 + 8(L_d - L_q)^2 I_a^2}}{4(L_d - L_q)I_a}\right]. \qquad (4\text{-}11)$$

Fig. 4-4 shows the MTPA trajectory of the IS-VFIPMSM. It is the set of points $\{(I_a \sin \beta_0, I_a \cos \beta_0)\}$ that the constant torque curves intersect the current circles as shown in Fig. 4-4 [83]. The constant torque curves can be obtained from equations (4-2) and (4-6), for a given torque and a varying armature current magnitude.
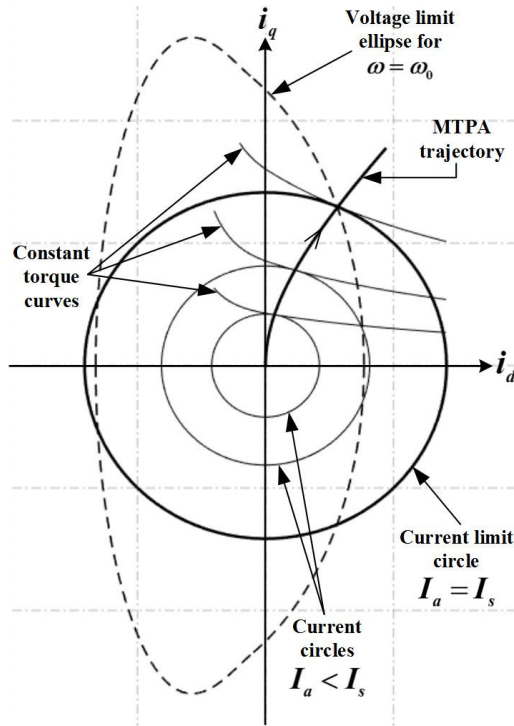
Fig. 4-4. MTPA trajectory for IS-VFIPMSM.

The angle which gives the maximum output torque of the IS-VFIPMSM is obtained by substituting $I_a = I_s$ in equation (4-11). The motor is accelerated with this torque until the terminal voltage reaches its limit ($V_a = V_s$) at $\omega = \omega_0$. This maximum speed for the constant torque region is given by [84]

$$\omega_0 = \frac{V_s}{\sqrt{\left(L_q i_{q_0}\right)^2 + \left[L_d i_{d_0} + \lambda_m\right]^2}}$$

(4-12)

in which $i_{d_0} = I_s \sin\beta_0$ and $i_{q_0} = I_s \cos\beta_0$.

Extending the Operating Limits via Two Different Flux Weakening Methods

At the rated load and speed ω_0, the terminal motor voltage reaches the maximum. To accelerate beyond this point, the growing back emf has to be compensated. In the VFIPMSM, this can be done by either of the two following strategies.

First, by demagnetizing the magnets with a short d-axis current pulse. This weakens the air-gap flux linkage allowing for some speed extension beyond the base speed. Once the new base speed is reached, another demagnetization pulse, which is greater in magnitude than the previous one, is excited to demagnetize the magnets to a lower value than the previous one, and so on. In this way, the need of applying a continuous negative d-axis current in the flux weakening region is eliminated. This is how the VFIPMSM was designed to perform [74] [78]. It was claimed in [74], [78], and [17] that this method eliminates the associated copper loss with the negative d-axis current in the flux weakening region, thus better machine efficiency. In this chapter, this is going to be investigated and compared with the next strategy.

Second, by using a continuous negative d-axis current taking into consideration the demagnetization property of low-H_c (Fig. 4-2), which is modeled by equation (4-6).

Based on the above two mentioned flux weakening strategies, there will be two operating torque/power-speed envelopes of the IS-VFIPMSM.

4.1.1 Flux weakening by demagnetization pulses (Method I)

Beyond the base speed, the maximum power per speed (MPPS) control is utilized to maximize the output power for a given speed [83]. As the speed increases beyond the base speed, the voltage limit forces the current angle to decrease, which means less d-axis current and more q-axis current, until $\omega = \omega_1$, where the d-axis current reaches zero as seen in Fig. 4-5.

It is obvious from a geometric point of view that the solution (i_d, i_q) which makes the MPPS trajectory is found at the intersection point of the current limit circle and the voltage limit ellipse [84]. The intersection point can be calculated by substituting

$$i_q^2 = I_s^2 - i_d^2 \tag{4-13}$$

into (10), which yields in [83]

$$(1 - \xi^2)i_d^2 + 2\frac{\lambda_m}{L_d}i_d + \left(\frac{\lambda_m^2}{L_d^2} + \xi^2 I_s^2 - \frac{V_s^2}{\omega^2 L_d^2}\right) = 0. \tag{4-14}$$

Since the intersection point is in the first quadrant, the positive solution is considered for the d-axis current in equation (4-14). Thus [83] [84],

$$i_d = \frac{1}{(\xi^2 - 1)}\left(\frac{\lambda_m}{L_d} + \sqrt{\xi^2 \frac{\lambda_m^2}{L_d^2} + (\xi^2 - 1)\left(\xi^2 I_s^2 - \frac{V_s^2}{\omega^2 L_d^2}\right)}\right), \tag{4-15}$$
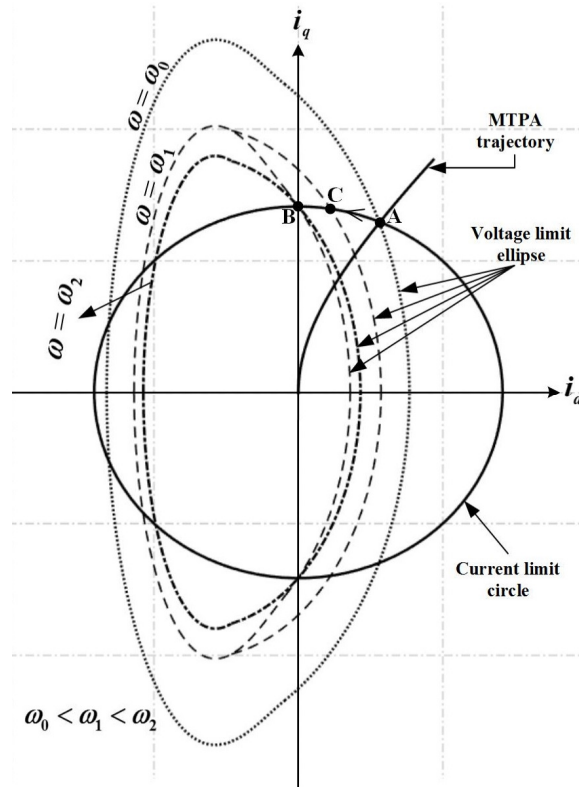
Fig. 4-5. Operating point trajectory of the IS-VFIPMSM using Method I.

where $\xi = L_q/L_d$.

At ω_1, the operating point is **B** in Fig. 4-5. To go beyond ω_1, the magnets should be demagnetized by a short *d*-axis current pulse to a lower magnetization level λ_{m_1}, where $\lambda_{m1} < \lambda_m$. The duration of this pulse can be as low as 10ms. The effect of the pulse duration on the magnetization state is not the subject of this chapter. For this point, one can consult [85]. This irreversible reduction in magnet flux widens the voltage limit ellipse at $\omega = \omega_1$, and shifts the operating point from **B** to **C** as seen in Fig. 4-5. As a result, the speed is extended from point **C** ($\omega = \omega_1$) to point **B** ($\omega = \omega_2$) on the MPPS trajectory, as seen in Fig. 4-5. Then, the magnets are demagnetized further to a lower level than λ_{m_1} by a *d*-axis current pulse, where magnitude is higher than the previous one. To ensure a smooth torque/power-speed curve, one can set the percentage of demagnetization by 5 % each time. The *d*-axis current magnitude needed for each demagnetization level is as per Fig. 4-2. Theoretically, the maximum speed of this region is obtained when the magnet flux reaches zero (fully demagnetized magnets). Thus from equation (4-10), it can be derived that

$$\omega_{max(MPPS)} = \frac{V_s}{L_q I_s}. \tag{4-16}$$

This speed marks the end of the torque/power-speed operating envelope of the IS-VFIPMSM. Thus, the operating point trajectory with this method in the (i_d, i_q) plane is AB, as seen in Fig. 4-5.

4.1.2   Flux weakening by continuous d-axis current (Method II)

With this method, and contrary to the previous method, continuous negative *d*-axis current is utilized in the flux weakening region taking into consideration the non-linear demagnetization property of the low-H_c magnets modeled by equation (4-6). The MPPS region is divided into two parts.

First from **A** to **B**, as seen in Fig. 4-6, this part is in the first quadrant of the (i_d, i_q) plane, and the magnet flux is constant. Therefore, the intersection point (solution) between the current limit circle and the voltage limit ellipse is given by equations (4-15) and (4-13).

Second, from **B** to **D**. As seen in Fig. 4-6, this part is in the second quadrant of (i_d, i_q) plane, and the magnet flux is varying with the negative *d*-axis current as per equation (4-6). Therefore, one can rewrite (4-14) as follows
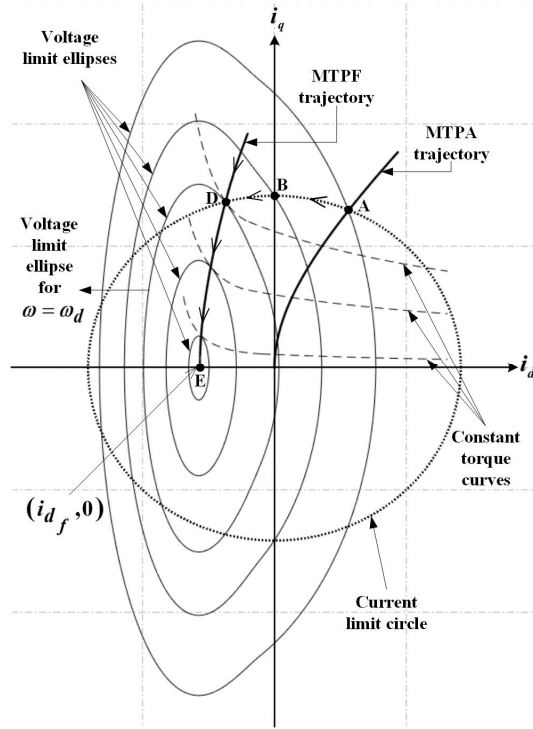
Fig. 4-6. Operating point trajectory of the IS-VFIPMSM using Method II.

$$(1 - \xi^2)i_d^2 + 2\frac{\lambda_m(i_d)}{L_d}i_d + \left(\frac{\lambda_m^2(i_d)}{L_d^2} + \xi^2 I_s^2 - \frac{V_s^2}{\omega^2 L_d^2}\right) = 0. \qquad (4\text{-}17)$$

The term $\lambda_m^2(i_d)$ is problematic. It makes equation (4-17) a sixth order polynomial in d-axis current, and an explicit solution is challenging. In order to overcome this, the measured magnet flux values in Fig. 4-2 are squared and drawn versus d-axis current as seen in Fig. 4-7. Then, this curve is modeled by a new polynomial as follows
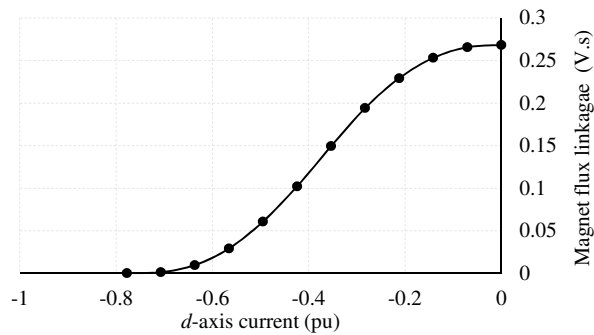
Fig. 4-7. Squared measured AlNiCo9 magnet flux linkage values versus d-axis current.

58

$$\lambda_m^2(i_d) = b_3 i_d^3 + b_2 i_d^2 + b_1 i_d + b_0, \tag{4-18}$$

where the coefficients are obtained from the curve-fit and shown in Table 0-3 in the appendix.

By substituting equations (4-6) and (4-18) into equation (4-17), it follows that

$$\frac{2a_3}{L_d} i_d^4 + \left(\frac{2a_2}{L_d} + \frac{b_3}{L_d^2}\right) i_d^3 + \left[(1 - \xi^2) + \frac{2a_1}{L_d} + \frac{b_2}{L_d^2}\right] i_d^2 + \left(\frac{2a_0}{L_d} + \frac{b_1}{L_d^2}\right) i_d$$
$$+ \left(\frac{b_0}{L_d^2} + \xi^2 I_s^2 - \frac{V_s^2}{\omega^2 L_d^2}\right) = 0. \tag{4-19}$$

The designated root of this quartic polynomial is [86] [87]

$$i_d = -\frac{L_d}{8a_3}\left[\left(\frac{2a_2}{L_d} + \frac{b_3}{L_d^2}\right) - \sqrt{\left(\frac{2a_2}{L_d} + \frac{b_3}{L_d^2}\right)^2 - 16\left(\frac{2a_3}{L_d}\right)^{3/2}\left(\frac{b_0}{L_d^2} + \xi^2 I_s^2 - \frac{V_s^2}{\omega^2 L_d^2}\right)^{1/2}}\right], \tag{4-20}$$

and $i_q = \sqrt{I_s^2 - i_d^2}$. ω_d marks the maximum speed of the MPPS region. Below this speed, the voltage limit ellipse shrinks to inside the current limit circle, as seen in Fig. 4-6. Thus, no intersection between the two limit curves, and no feasible solution can be found.

In order to increase the speed beyond ω_d, the maximum torque per flux (MTPF) control is adopted. This control method is applicable in the high speed operation where the MPPS operation cannot be achieved [83].

Let the d-axis flux linkage be denoted by

$$\lambda_d \equiv \lambda_m(i_d) + L_d i_d, \tag{4-21}$$

then it follows from the voltage limit ellipse equation (4-10) that:

$$\left(L_q i_q\right)^2 + \lambda_d^2 = (V_s/\omega)^2. \tag{4-22}$$

By substituting equation (4-22) into the torque equation (4-2), it follows that,

$$T^2 = \left(\frac{3P}{2}\right)^2 [(1 - \xi)\lambda_d + \xi\lambda_m(i_d)]^2 \frac{(V_s/\omega)^2 - \lambda_d^2}{L_q^2}. \tag{4-23}$$

Differentiating (4-23) with respect to λ_d and making it equal to zero results in

$$\lambda_d = \frac{1}{4(L_d - L_q)}\left(-L_q\lambda_m(i_d) + \sqrt{L_q^2\lambda_m^2(i_d) + 8(L_d - L_q)^2(V_s/\omega)^2}\right). \tag{4-24}$$

Equation (4-24) denotes the *d*-axis flux needed to achieve a maximum torque in the MTPF region. By substituting equations (4-6), (4-18), and (4-21) into equation (4-24), and solving for i_d, it follows that

$$2ma_3 i_d^4 + \left[2ma_2 + (n^2 L_q^2 - m^2)b_3\right]i_d^3 + \left[2ma_1 + (n^2 L_q^2 - m^2)b_2 - 1\right]i_d^2$$
$$+ \left[2ma_0 + (n^2 L_q^2 - m^2)b_1\right]i_d + \left[(n^2 L_q^2 - m^2)b_0 + \frac{(V_s/\omega)^2}{2L_d^2}\right] = 0 \tag{4-25}$$

in which

$$m = -\frac{\xi}{4(L_d - L_q)} - \frac{1}{L_d}, \tag{4-26}$$

$$n = \frac{1/L_d}{4(L_d - L_q)}. \tag{4-27}$$

The designated root of the quartic polynomial (4-25) is [86] [87]

$$i_d = -\frac{1}{8ma_3}\left\{\left[2ma_2 + (n^2 L_q^2 - m^2)b_3\right]\right.$$
$$-\left(\left[2ma_2 + (n^2 L_q^2 - m^2)b_3\right]^2\right. \tag{4-28}$$
$$\left.\left. - 16(2ma_3)^{\frac{3}{2}}\left[(n^2 L_q^2 - m^2)b_0 + \frac{(V_s/\omega)^2}{2L_d^2}\right]^{\frac{1}{2}}\right)^{1/2}\right\}.$$

By substituting (4-24) into (4-22), and solving for i_q, it follows,

$$i_q = \frac{1}{L_q}\left\{\frac{V_s^2}{\omega^2} - \left[\frac{1}{4(L_d - L_q)}\left(-L_q\lambda_m(i_d) + \sqrt{L_q^2\lambda_m^2(i_d) + 8(L_d - L_q)^2(V_s/\omega)^2}\right)\right]^2\right\}^{1/2}. \tag{4-29}$$

By substituting equations (4-6) and (4-18) into equation (4-29), the full expression of i_q is obtained as follows

$$i_q = \frac{1}{L_q}\left\{\left(\frac{V_s}{\omega}\right)^2 - \left[\frac{1}{4(L_d - L_q)}\left(-L_q(a_3 i_d^3 + a_2 i_d^2 + a_1 i_d + a_0)\right.\right.\right.$$
$$\left.\left.\left. + \sqrt{L_q^2(b_3 i_d^3 + b_2 i_d^2 + b_1 i_d + b_0) + 8(L_d - L_q)^2(V_s/\omega)^2}\right)\right]^2\right\}^{1/2}, \tag{4-30}$$

60

where i_d is as per equation (4-28). Thus, (4-28) and (4-30) gives the solution set $\{(i_d, i_q)\}$ for the maximum torque per flux trajectory of the VFIPMSM. Those are the set of points where the voltage limit ellipse intersects tangentially with the constant torque curves as seen in Fig. 4-6.

It is clear from Fig. 4-6 that as the speed goes to infinity, the q-axis current goes to zero. Thus, it falls from equation (4-22) that λ_d goes to zero as well. By substituting $\lambda_d = 0$ into equation (4-21), it yields

$$\lambda_m(i_d) + L_d i_d = 0, \tag{4-31}$$

and by substituting (4-6) into (4-31), it follows that

$$a_3 i_d^3 + a_2 i_d^2 + (a_1 + L_d) i_d + a_0 = 0. \tag{4-32}$$

The discriminant of equation (4-32) is zero, and the term $[a_2^2 - 3a_3(a_1 + L_d)]$, which determines the type of this cubic function, is not equal to zero. Therefore, the designated root is [88]

$$i_{d_f} = \frac{9a_3 a_0 - a_2(a_1 + L_d)}{2[a_2^2 - 3a_3(a_1 + L_d)]} \tag{4-33}$$

Thus, at the infinite speed, the voltage limit ellipse shrinks to the point $\mathbf{E}(i_{d_f}, 0)$, as seen in Fig. 4-6, where i_{d_f} is given by equation (4-33). From Fig. 4-6, it can be seen that the operating point trajectory with this method is **ABDE**.
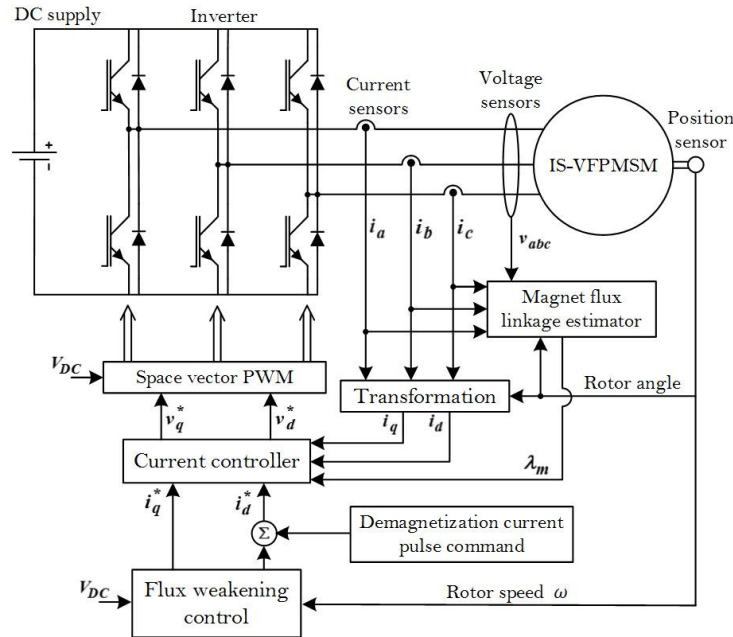
Fig. 4-8. Block diagram of the drive system.

Fig. 4-8 shows the block diagram of the IS-VFIPMSM current controller according to the forgoing flux weakening algorithms. The current command is always kept within the current limit circle and the voltage limit ellipse. The magnet flux linkage is estimated as per [89].

Fig. 4-9 and Fig. 4-10 show the output characteristics of the IS-VFIPMSM with method I and method II, respectively. The results are shown in per unit, and the rated motor parameters are shown in Table 0-2 in the appendix. Below the base speed, the motor is accelerated with the MTPA, where the torque is kept at its maximum, and the power is proportional to the motor speed, as seen in Fig. 4-9 and Fig. 4-10.

From Fig. 4-9, in the flux-weakening region (*Region II*), where $i_d = 0$ and the flux is weakened by demagnetizing the magnets via negative d-axis current pulses, it can be seen that the output torque and power decrease rapidly. This is due to the significant reduction in the magnet flux to extend the speed with the rated machine current by MPPS control, as seen in Fig. 4-9. In addition, the speed with this method is not much extended, where the maximum speed is almost double the base speed.

However, when the MPPS control continued with a continuous negative d-axis current, as seen in Fig. 4-10 (*Region II*, where $i_d < 0$), the output torque and power are higher than the ones obtained from method I. This is because the continuous negative d-axis current demagnetizes the magnets and weakens the air-gap flux at the same time. Thus, the magnet's demagnetization level needed to extend the speed in method II is less than that in method I. This saving in the magnet flux enhances the output torque and consequently the output power, and extends the speed, as seen in Fig. 4-10 (*Regions II and III*). For instance, a negative 0.35 per unit d-axis current pulse demagnetizes the low-H_c magnets to 75% and extends the speed to 1.5 per unit as seen in Fig. 4-9. However, the same magnitude of continuous negative d-axis current demagnetizes the low-H_c magnets to 75% and extends the speed to almost 3 per unit as seen in Fig. 4-10. In other words, to reach a speed of 1.5 per unit using method II, less d-axis current is required compared with method I. In fact, only 0.2 per unit negative d-axis current is needed to reach a 1.5 per unit speed as seen in Fig. 4-10. This corresponds to a 90% magnetization state. In terms of motor torque at 1.5 per unit speed, Fig. 4-9 and Fig. 4-10 show a difference of 0.1 per unit torque in favor of continuous negative d-axis current method. This is because of the saving on magnet flux from 75% when using a negative d-axis current pulse to 90% when a continuous negative d-axis current is used.
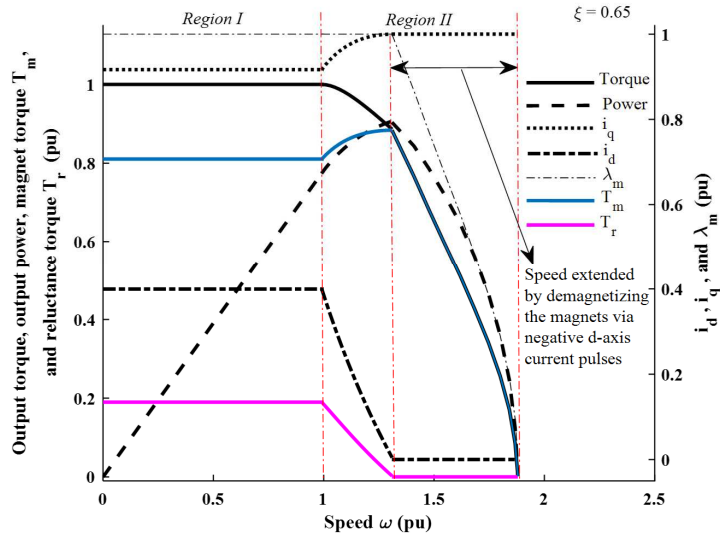
Fig. 4-9. Output characteristics of the IS-VFIPMSM using method I (simulated result).
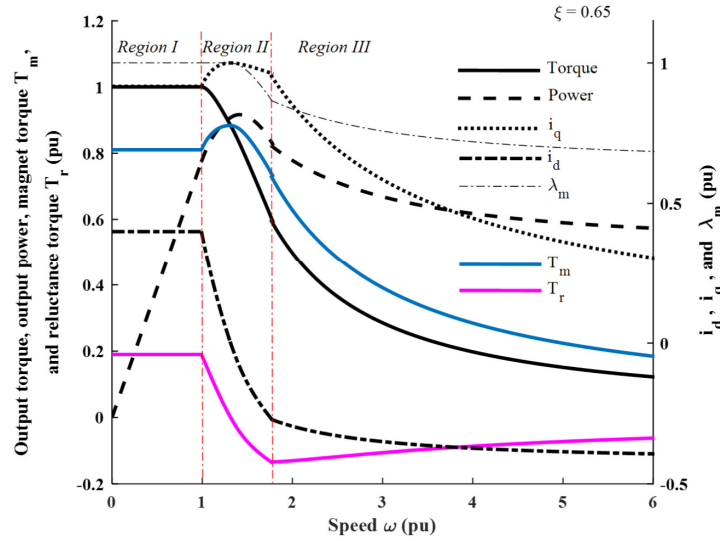
Fig. 4-10. Output characteristics of the IS-VFIPMSM using method II (simulated result).

4.1.3 Effect of saliency on the IS-VFIPMSM's output power using Method II

Based on equation (4-33), Fig. 4-11 shows the relation between the d-axis inductance and the final d-axis current (i_{d_f}) reached as the speed goes to infinity. Note that the saliency ($\xi = L_q/L_d$) increases as the d-axis inductance decreases, with q-axis inductance held constant. In addition, from Fig. 4-11, it can be seen that as the d-axis inductance decreases, the

final d-axis current (i_{d_f}) increases in the negative direction. This means, and as per the operating point trajectory shown in Fig. 4-6, the MTPF trajectory is shifted to the negative direction resulting in widening the MPPS trajectory of the IS-VFIPMSM, as seen in Fig. 4-12. The effect of this change on the output power can be seen in Fig. 4-13. In Fig. 4-13, below the base speed, it can be seen that there is a slight decrease in the output power as the saliency increases. This is due to the reduction of the positve reluctance torque as the saliency approaches unity. On the other hand, beyond the base speed, the increase in saliency enhances the output power. An ideal constat power beyond the base speed is not acheievable in the VFIPMSMs as the magnets are irreverisibly demagnetized during the flux weakening control.

From a machine design perspective, a constant output power in the flux weakening region for IPMSMs can be achieved if $\lambda_m = I_s L_d$ [90] [91]. However, for VFIPMSMs, the magnet/rotor flux linkage has a nonlinear variation with the negative d-axis current. This nonliearity brings challenges and opens a new research window for variable flux machine designers to overcome and investigate in order to achive a constant power region. The saliency manipulation shown in this subsection can be a subject for further studies.
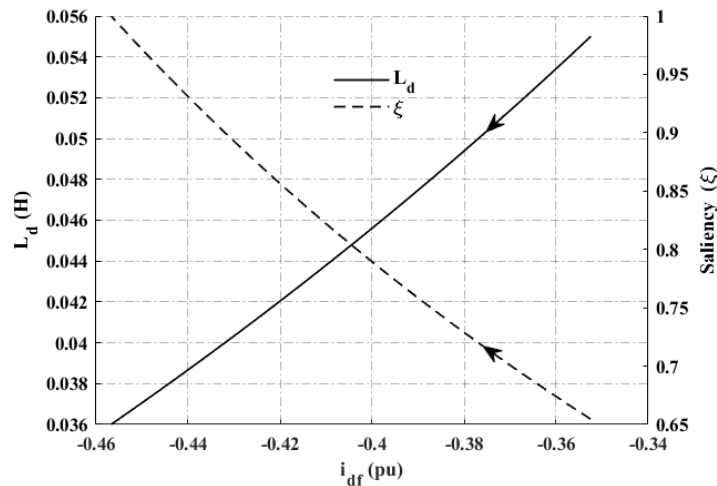
Fig. 4-11. Relationship between d-axis inductance L_d, saliency ξ, and i_{d_f}.

64
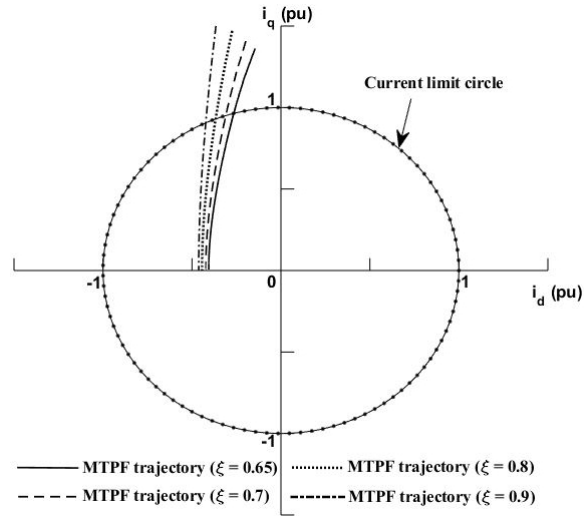
Fig. 4-12. MTPF trajectories for different saliencies.
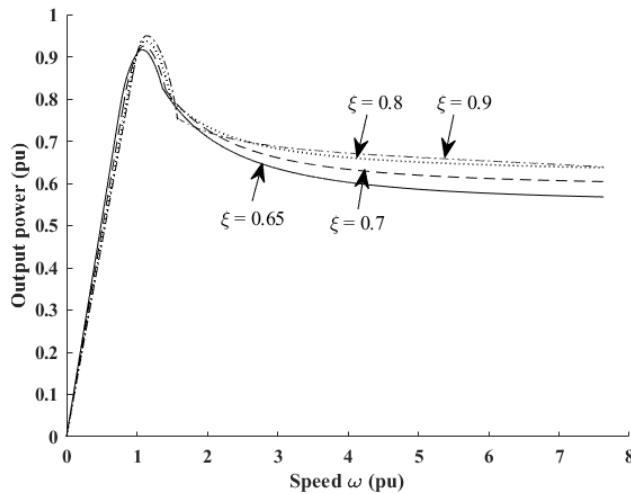
Fig. 4-13. Effect of saliency on the output power.

Experimental Verification

The testbed is as shown in Fig. 4-14. A two-level inverter with a 5 kHz switching frequency is used to drive the IS-VFIPMSM. A space-vector PWM scheme is adopted for better DC bus voltage utilization. The magnet flux linkage is estimated as in chapter 3 [89].

Fig. 4-15 depicts the output torque and power versus speed envelops of the IS-VFIPMSM using the flux weakening control methods explained in the previous section. It is clear that when the air-gap flux is weakened by demagnetizing the magnets with *d*-axis current pulses

(method I), and without the use of continuous negative *d*-axis current, the output motor characteristics experience a rapid decrease in the flux weakening region. This is due to the significant demagnetization level required to extend the speed at the rated machine current, as seen in Fig. 4-16 and Fig. 4-17. Also, with this method the motor speed is not extended, and the maximum speed achieved is almost double the base speed. In terms of efficiency, Fig. 4-18 shows the efficiency maps of the IS-VFIPMSM obtained from finite element software using both methods. It can be seen that the torque-speed curve obtained using method I decreases rapidly beyond base speed, whereas in method II, the torque-speed curve is much extended.

The simulated and the experimentally validated result show that the output power of the IS-VFIPMSM cannot be kept constant in the flux weakening region. This is due to the fact that the magnets are irreversibly demagnetized with the negative *d*-axis current (either pulse or continuous).
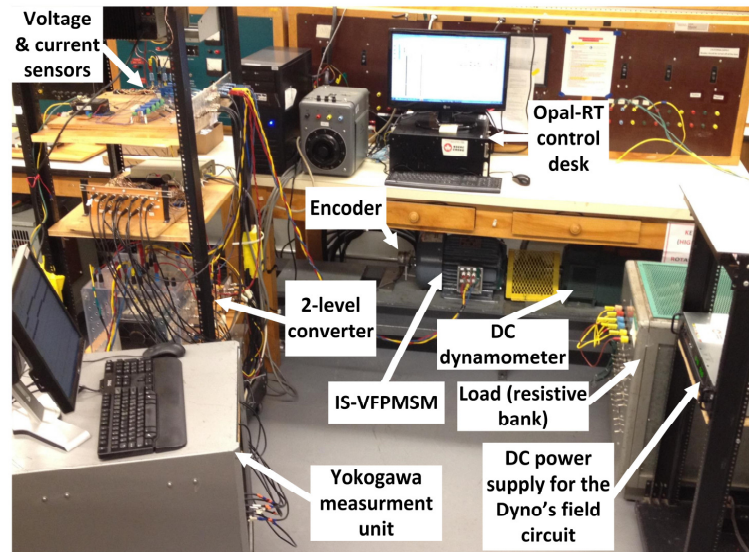
Fig. 4-14. Experimental setup.
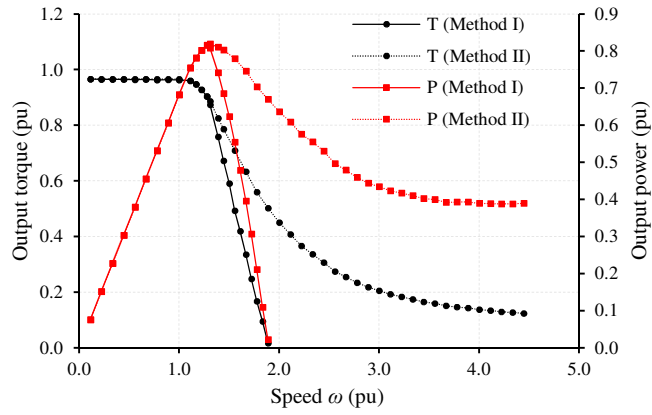
Fig. 4-15. Measured output torque and power versus speed.
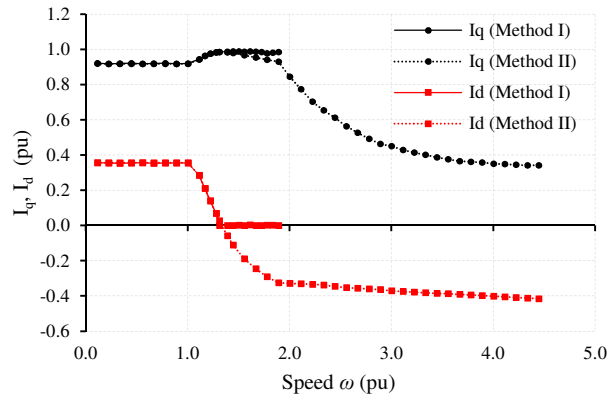
Fig. 4-16. Measured currents versus speed.
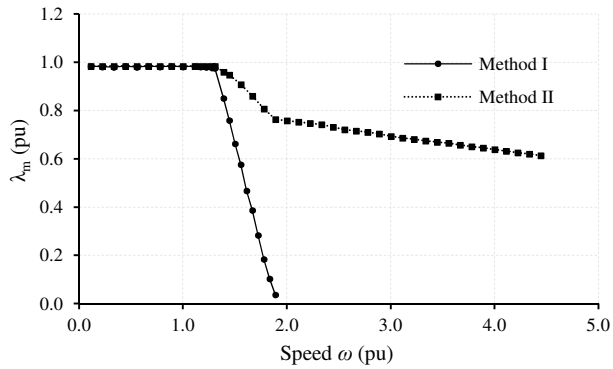
Fig. 4-17. Measured magnet flux linkage versus speed.
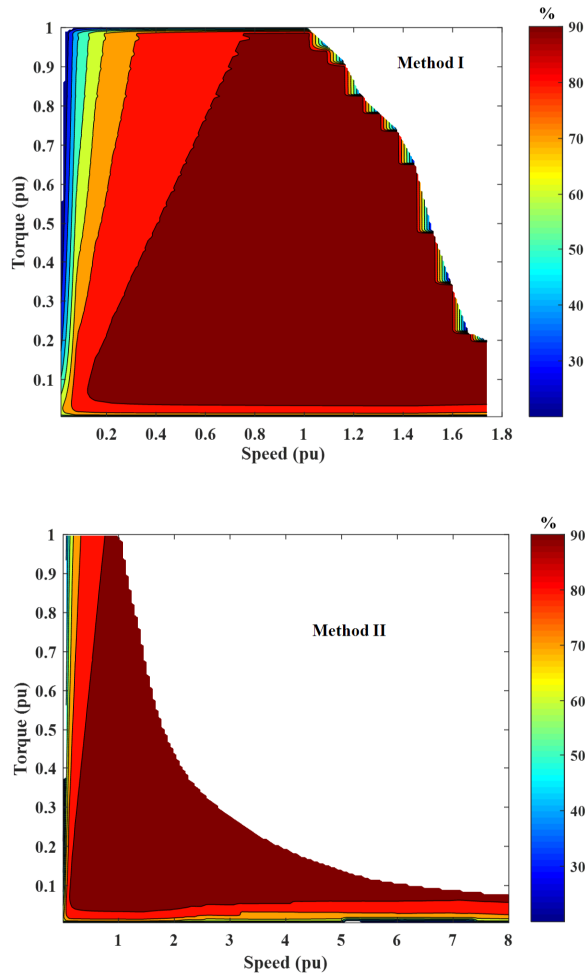
Fig. 4-18. Efficiency maps obtained by finite element software using method I and method II.

Comparison between the IS-VFIPMSM and an Equivalent IPMSM in terms of Operating Point Trajectories, Operating Envelopes, Efficiency, and Speed Range

Both motors have the same design, ratings, and saliency ($L_d > L_q$) for more accurate comparison. The permanent magnet material for the IPMSM is NdFeB and for the VFIPMSM is AlNiCo9. The second quadrant B-H curves for both materials are shown in Fig. 4-19. Since operating with continuous negative d-axis current (method II) results in better motor performance for the VFIPMSM as seen in sections 4.4 and 4.5, this method is used for the comparison with the IPMSM.
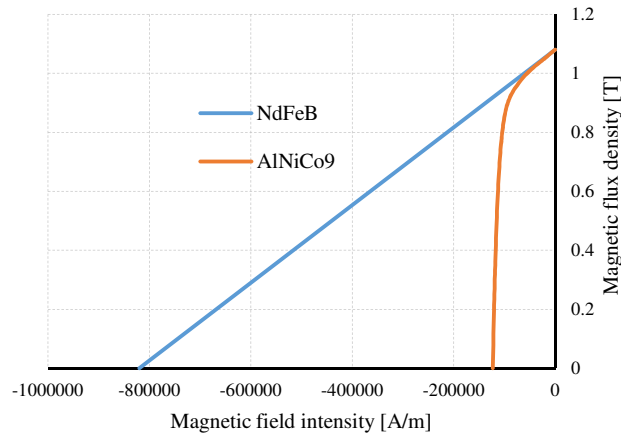
Fig. 4-19. Flux density versus field intensity for AlNiCo9 and NdFeB.

Fig. 4-20 shows the operating point trajectories for both motors in the (i_d, i_q) plane. The solutions of the operating point in the (i_d, i_q) plane for the IPMSM are presented in [84], and for the VFIPMSM including the nonlinear demagnetization characteristics of the low-H_c magnets are presented in section 4.3. As seen in Fig. 4-20, theoretically, the operating point trajectory as the motor accelerates from zero to infinite speed is $A_1A_2A_3$ for the IPMSM, and $B_1B_2B_3$ for the VFIPMSM. Also, it can be seen that both motors share the same MTPA trajectory. This is because no demagnetization occurs for the AlNiCo9 magnets in the first quadrant. However, beyond the rated speed and in the second quadrant of the (i_d, i_q) plane, unlike the Nd-Fe-B magnets, the AlNiCo9 magnets of the VFIPMSM are permanently demagnetized by negative d-axis current. Although, this permanent demagnetization results in reshaping the voltage-limit ellipses of the VFIPMSM to semi-ellipses, it reduces the amount of negative d-axis current needed as the speed goes to infinity compared to the IPMSM. As seen in Fig. 4-20, the amount of d-axis current needed as the speed goes to infinity is negative 0.63 per unit for the IPMSM compared to a negative 0.4 per unit for the VFIPMSM. Fig. 4-21 presents a clearer combined comparison of the operating point trajectories between the two motors in the (i_d, i_q) plane without the voltage limit ellipses. The difference in the operating region between the two motors in the (i_d, i_q) plane is marked by the highlighted area in Fig. 4-21. This is further illustrated with current versus speed curves shown in Fig. 4-22, where the reduction in the amount of d-axis current needed in the high-speed region with the VFIPMSM is clearly evident.
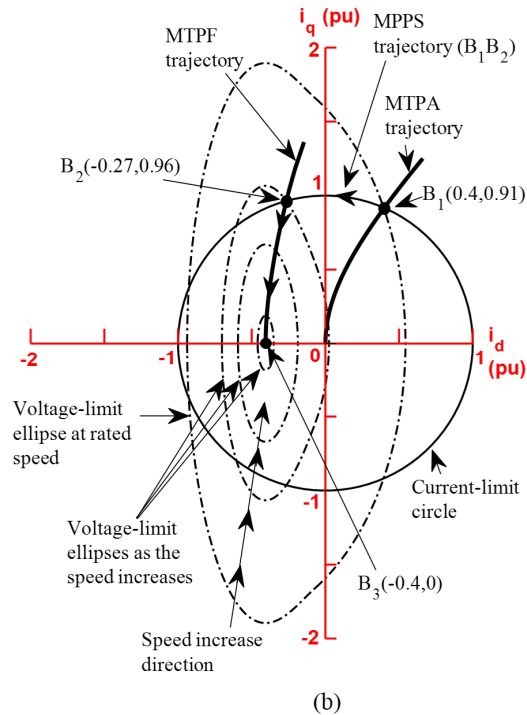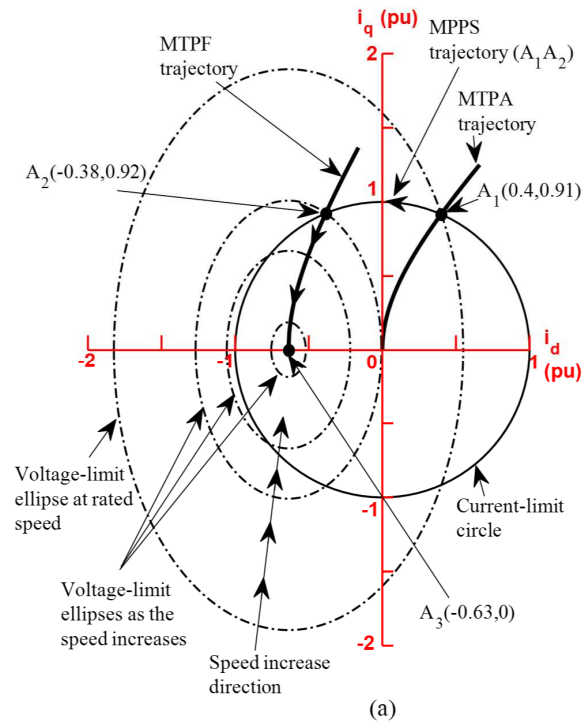
Fig. 4-20. Simulated result of the operating point trajectories: (a) inverted-saliency IPMSM, (b) inverted-saliency VFIPMSM.
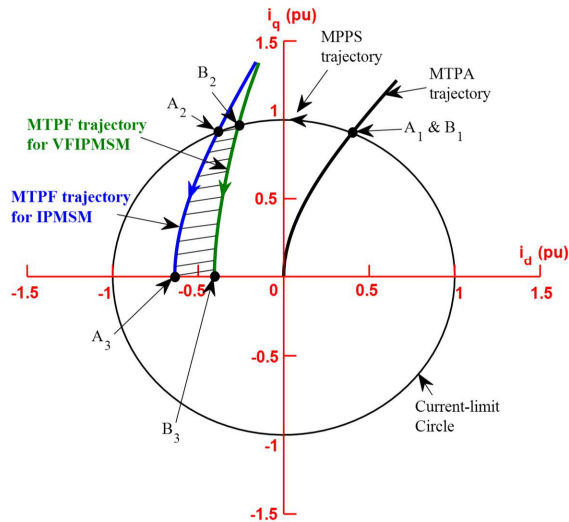
Fig. 4-21. Difference in the operating point trajectory between the IPMSM and the VFIPMSM in the (i_d, i_q) plane.
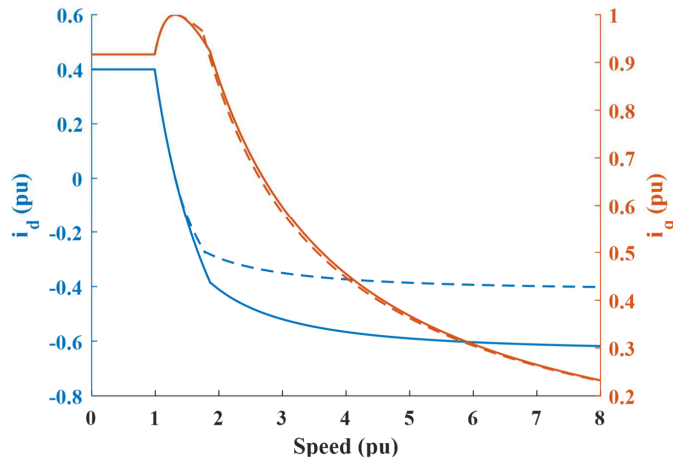
Fig. 4-22. *dq*-axis currents versus speed curves (simulated result): solid line is IPMSM, and dashed line is VFIPMSM.

Fig. 4-23 shows the simulated torque/power versus speed curves of both motors. Clearly, the IPMSM has better output characteristics compared to the VFIPMSM. This reduction in the output torque and power of the VFIPMSM in the high-speed region is expected, and it is due to the permanent demagnetization of the low-H_c magnets causes by negative *d*-axis current. Since the research on the VFIPMSM is still ongoing, this drawback of the VFIPMSM can still be minimized by more enhanced and optimized motor designs. However, for the VFIPMSM,

71

this permanent demagnetization of the low-H_c magnets in the high-speed region reduces the iron losses, and the reduction in the amount of current results in copper loss reduction compared
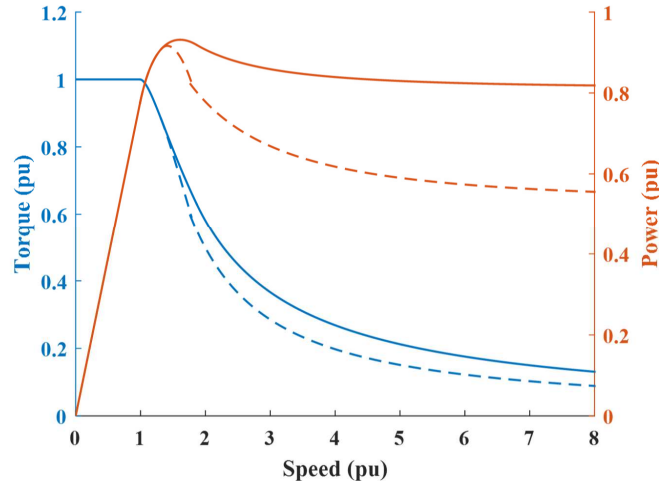
Fig. 4-23. Torque/power versus speed curves (simulated result): solid line is IPMSM, and dashed line is VFIPMSM.

to the IPMSM. Consequently, the efficiency of the VFIPMSM is higher in the high-speed region compared to the IPMSM. This is the actual benefit of the VFIPMSM. Besides the high torque capability in the low-speed region, which is comparable to the IPMSM, the motor can still operate with high efficiency in the high-speed region. This improvement in the motor efficiency can contribute to battery energy savings, especially when cruising for extended time periods e.g. on the highway. By means of finite element (FE) analysis, Fig. 4-24, Fig. 4-25 and Fig. 4-26 demonstrate the comparison between the IPMSM and the VFIPMSM in terms of iron loss, copper loss, and efficiency, respectively. In those three figures, the loss reduction and efficiency improvement of the VFIPMSM in the high-speed region are apparent.

In terms of speed extension, theoritically the speed can be extended to infinite speed when $\lambda_m < I_s L_d$ [84] [91], which is the case for both motors in the comparison. However, in reality considering the motor losses and the physical limits, there is an upper limit for both motors. Using finite element software to obtain the torque-speed curves of both motors for extended speeds as depicted by Fig. 4-27, it can be seen that the speed is extended with the VFIPMSM compared to an IPMSM of the same ratings.
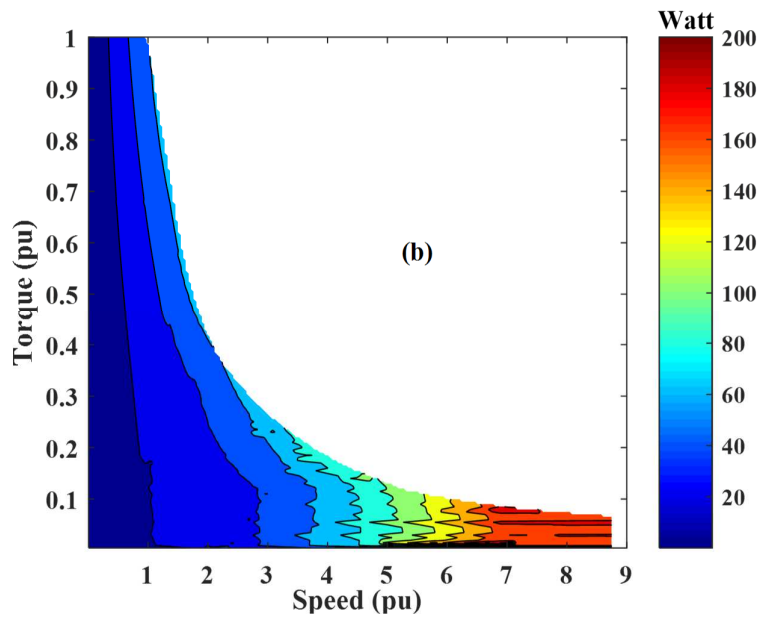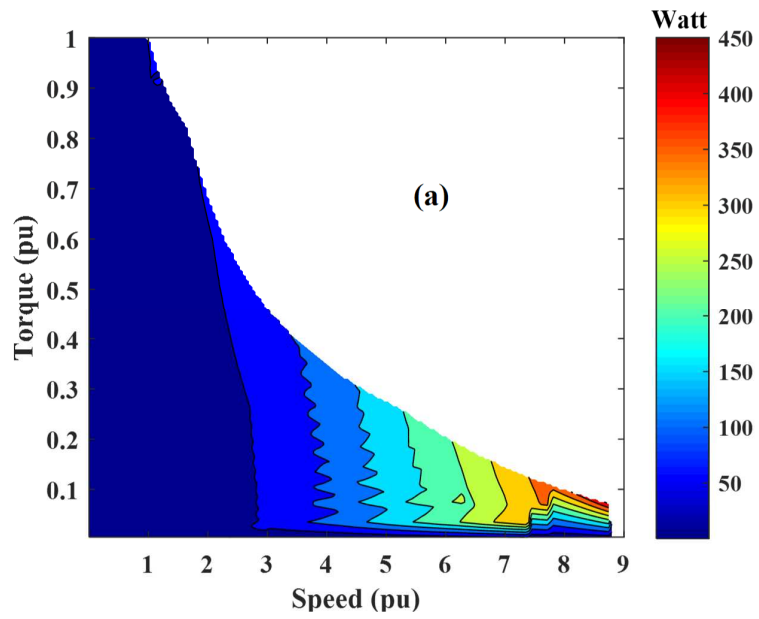
Fig. 4-24. Iron loss via finite element: (a) IPMSM, (b) VFIPMSM.
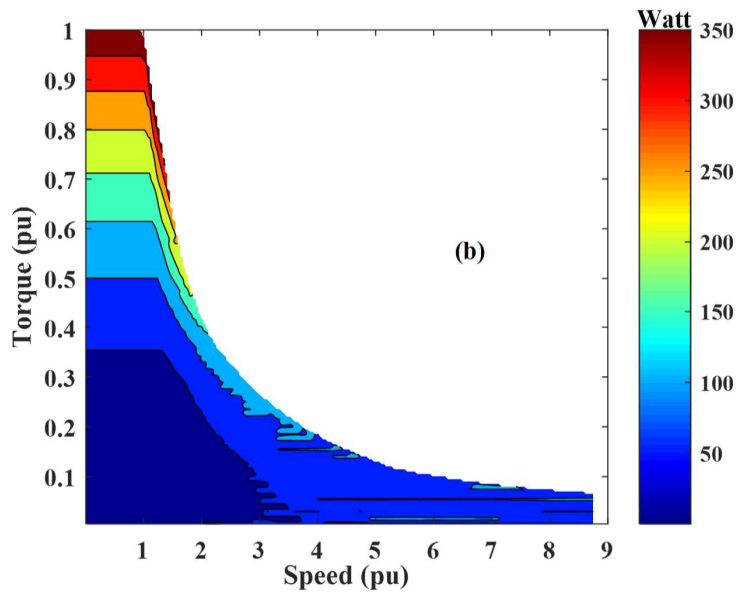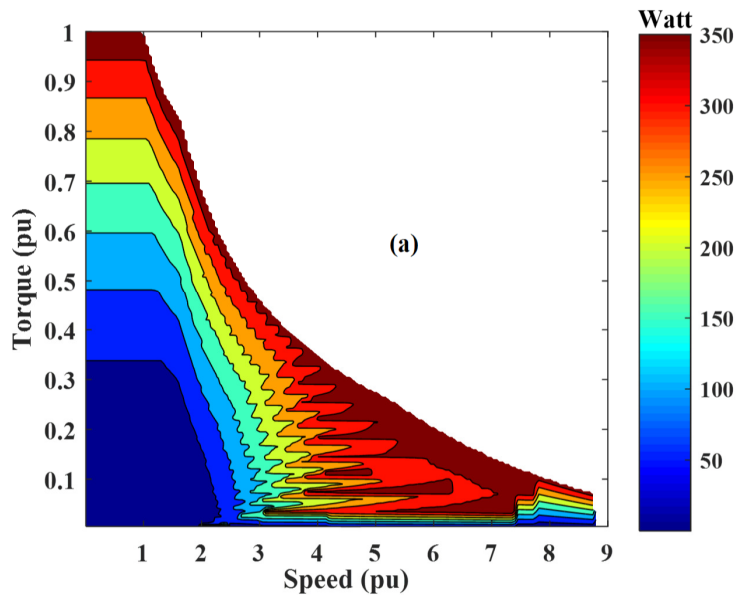
Fig. 4-25. Copper loss via finite element: (a) IPMSM, (b) VFIPMSM.
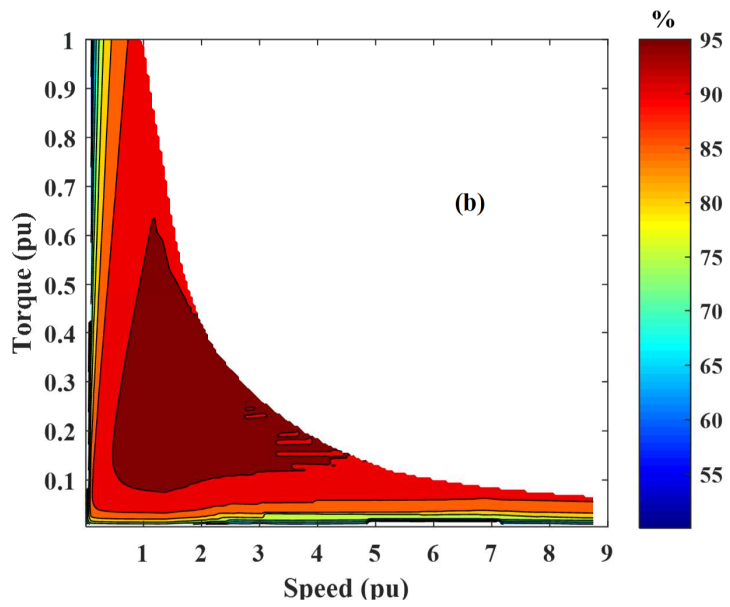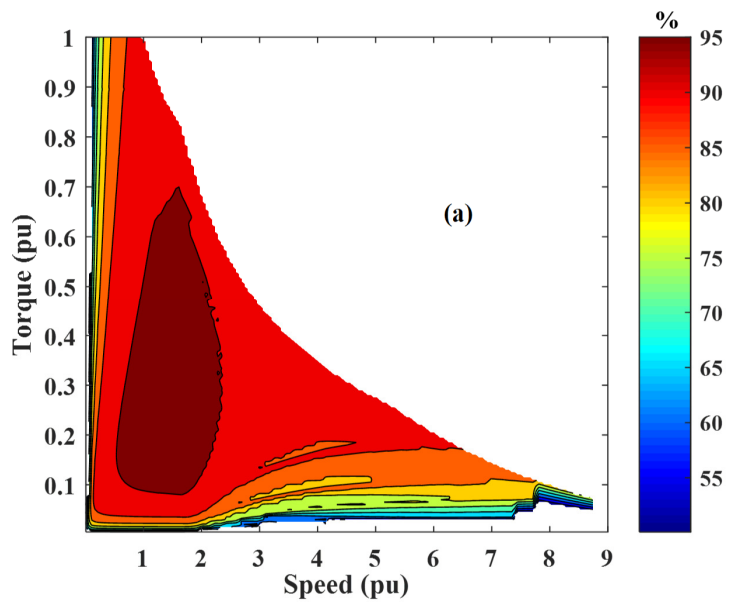
Fig. 4-26. Efficiency maps via finite element, from 50% to 95%: (a) IPMSM, (b) VFIPMSM.
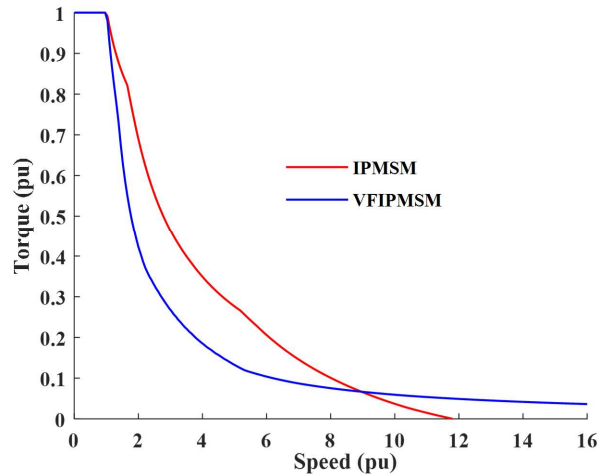
Fig. 4-27. Torque-speed curves for extended speed (finite element result).

Summary

In this chapter, the operating envelopes of the inverted-saliency variable-flux interior permanent magnet synchronous motor is investigated. The solution of the operating point (i_d, i_q) in the flux weakening control of the IPMSM is extended to the IS-VFIPMSM taking into account the irreversible demagnetization property of the low-H_c magnets. Thus, new solutions of the operating point are reached for the maximum power per speed control and for the maximum torque per flux control. Based on the simulated and experimental results, the following can be stated.

1) Flux weakening via demagnetizing the low-H_c magnets of the IS-VFIPMSM by only short negative d-axis current pulses leads to a quick drop of the motor output characteristics. This is due to the high level of magnet demagnetization needed to extend the speed with the rated motor current.

2) The use of negative d-axis current considering the demagnetization property of the low-H_c magnets greatly enhances the output characteristics and extends the speed range of the IS-VFIPMSM. This is because the continuous negative d-axis current demagnetizes the magnets and weakens the air-gap flux at the same time, which results in a lower level of magnet demagnetization, compared with the previous method, needed to extend the speed beyond the base speed. Although, the continuous negative d-axis current causes negative reluctance torque, the saving in magnet flux results in a higher output torque than in the previous method.

3) Due to the irreversible demagnetization property with negative d-axis current, the output power of the IS-VFIPMSM cannot be kept constant during the flux weakening control.

4) The derived equation (4-33) shows that the maximum d-axis current reached as the speed goes to infinity (i_{d_f}) is a function of the d-axis inductance for a given demagnetization curve. Based on this relationship, the reduction of d-axis current (increased saliency) leads to an increase in the magnitude of i_{d_f}, which results in shifting the MTPF trajectory to the left side in the (i_d, i_q) plane. Consequently, the MPPS trajectory is widened. Also, with this comes an improvement in the output power in the flux weakening region, which is mainly due to the lower negative reluctance torque as the d-axis inductance decreases (saliency increases).

5) Although, the permanent demagnetization of the low-H_c magnets (AlNiCo9) by negative d-axis current results in output torque and power reduction beyond the base speed compared to the IPMSM, it reduces the amount of iron loss of the VFIPMSM compared to the IPMSM. Also, it reduces the amount of d-axis current needed in the high-speed region compared to the IPMSM, which results in lowering the copper loss of the VFIPMSM. The total loss reduction caused by the permanent demagnetization of the low-H_c magnets improves the efficiency of the VFIPMSM in the high-speed region compared to the IPMSM. Moreover, it extends the speed range of the VFIPMSM compared to the IPMSM.

Chapter 5. Braking a Variable Flux-Intensifying IPMSM in Minimal Time

Introduction

Variable-flux IPMSMs were recently introduced as a strong rival to the interior permanent magnet synchronous motors (IPMSMs) especially for high-speed applications including but not limited to electrified transportation [77] [16] [92]. The utilization of the low-coercivity (low-H_c) magnets in the variable-flux IPMSMs allows reduction of copper and iron losses by means of magnetization state manipulation, thus having improved motor efficiency especially in the high-speed region [77] [16]. Because of low-H_c, the magnets can be subject to demagnetization by load currents during the loading conditions. This issue has been addressed by having an inverted-saliency (flux-intensifying) type of variable flux IPMSMs [77] [16]. This way, the positive d-axis current, which is utilized in the constant torque region to maximize the output torque, stabilizes the operating point of the low-H_c magnets and prevents possible demagnetization by the load current [77] [16]. In this chapter, the proof-of-concept flux-intensifying IPMSM proposed in [16] is utilized to validate the proposed braking algorithm.

While recent work on the variable-flux IPMSM focuses on optimizing the magnetization current of the low-H_c magnets to not oversize the inverter [93] [16] and improving the output power characteristics over a wide speed range to deliver the electric vehicle requirements [92] [79], this chapter throws light on a drawback regarding the braking aspect of the variable-flux IPMSM and proposes a method to overcome this limitation.

In the high-speed region, unlike the IMPSM, the low-H_c magnets in the variable-flux IPMSM are permanently demagnetized to a reduced level. Hence, the braking torque is not being maximized as the speed goes to zero, thus minimum time braking is not feasible. In order to magnetize the magnets during braking, a positive d-axis current is needed to be supplied. The amount of this current ranges from 1 per unit [92] to almost 3 per unit [77] [16] depending on the type and design of the low-H_c magnets. Supplying this amount of current in the high-speed region when the inverter is running out of DC bus voltage is quite challenging. Various braking methods for three-phase AC motors are presented in the literature and can be summarized as follows.

Regenerative braking, where the braking energy is fed back to the mains, is the only existing efficient braking method [94]. Since it increases the cost of the drive system because of the bidirectional power-flow electronic devices, e.g. active-front-end rectifiers, it is utilized in high power applications, e.g. traction and wind applications, where the efficiency overweighs the cost [95] [96]. However, in medium- and low-power applications, the diode bridge rectifiers are used for lower cost and robustness [97]. With such unidirectional power-flow devices, the braking energy is dissipated in the motor/inverter system [97]. However, with this method, a controlled braking resistor connected across the DC link is usually used to passively dissipate the braking energy in the form of heat instead of dissipating it into the motor windings, and prevent prohibitive dc bus voltage rise [97]. This also increases the cost and size of the inverter [98].

In order to brake the motor without any additional power electronic devices, the only solution is to increase system losses [94] [99]. Even though the copper loss is not significant in high-power and efficiency applications, it can significantly reduce the braking time in medium and low- power applications [97] [98]. Another example is flux braking of induction motors [94] [100], where in principle, the flux is kept low below base speeds to improve the efficiency, during the braking it should be increased to its rated value which worsen the efficiency. The problem with these methods is the excessive DC bus voltage rise during rapid deceleration. In order to avoid this issue with such braking methods, the braking power has to be reduced which results in slowing the deceleration process [101]. Current harmonic injection to increase the losses during braking is also proposed in [102] for an induction motor, however, the unavoidable resultant torque ripple degrades the braking performance. A novel loss controller which maximizes the losses within the motor/inverter system during braking by means of a high-frequency square wave signal superimposed on the *d*-axis current is presented in [94] for vector controlled induction motors, where torque ripple minimization and improved braking performance are reported. The proposed method allows regenerative braking at high-torque operation with a diode front-end rectifier, however, it complicates the drive system design.

[103] and [104] proposed a multi-phase excitation for braking the synchronous reluctance motor using a diode bridge rectifier. In addition to the excited phase, a second phase is energized during braking to dissipate the kinetic energy and reduce the DC link rise. In this work, an open-

loop and a closed-loop control are illustrated for the second energized phase current. Despite the inefficiency, the DC bus voltage rise is minimized to 15%.

Even though this work is on the variable-flux IPMSM, the earlier described braking schemes are for the induction and synchronous reluctance motor drives. This is because, up to our knowledge, almost no literature discusses minimal time braking for IPMSM drives. This could be due to the high-coercivity of the permanent magnet excitation, which makes the flux manipulation within the electrical drive limits impossible. However, with the emergence of variable-flux IPMSMs, where the magnet flux can be altered within the inverter electrical limits, the necessity of minimal time braking schemes becomes vital.

Problem Illustration

Fig. 5-1 shows a simulated step change in the speed of the FI-VFIPMSM from zero to rated speed and vice versa. A negative current pulse of eight amperes magnitude and of 50 millisecond width is input at 0.5 second to demagnetize the low-H_c magnets from 100% to about 30% magnetization state. The effect of the pulse width on the magnetization state of the magnets is not the subject of this chapter and a detailed discussion can be found in [52]. As a result of the demagnetization, the deceleration time is extended to 2.5 times the acceleration time as seen in Fig. 5-1.

An obvious solution to maximize the braking torque is to magnetize the magnets. Fig. 5-2 shows the measured amount of d-axis current needed to magnetize and demagnetize the low-H_c magnets (AlNiCo9). From Fig. 5-2(a), it can be seen that almost a 2.5 per unit current is needed to fully magnetize the AlNiCo9 magnets. The amount of this current is varying depending on the type and design of the low-H_c magnets. It can vary from 1 per unit to almost 3 per unit. The variable-flux IPMSM is designed to handle this magnetizing current for short time periods. Also, the inverter is rated to continuously supply this current. Now, the question is about the available voltage to supply this current or part of it in the high-speed region.

Fig. 5-3 shows the voltage contours at different speeds and at 30 % magnetization state in the (i_d, i_q) plane. It can be seen that as the speed decreases, the voltage limit ellipse widens allowing for more current to be supplied. The blue arrows illustrate the maximum positive d-axis current that can be excited as the speed decreases assuming a small q-axis current, e.g. no
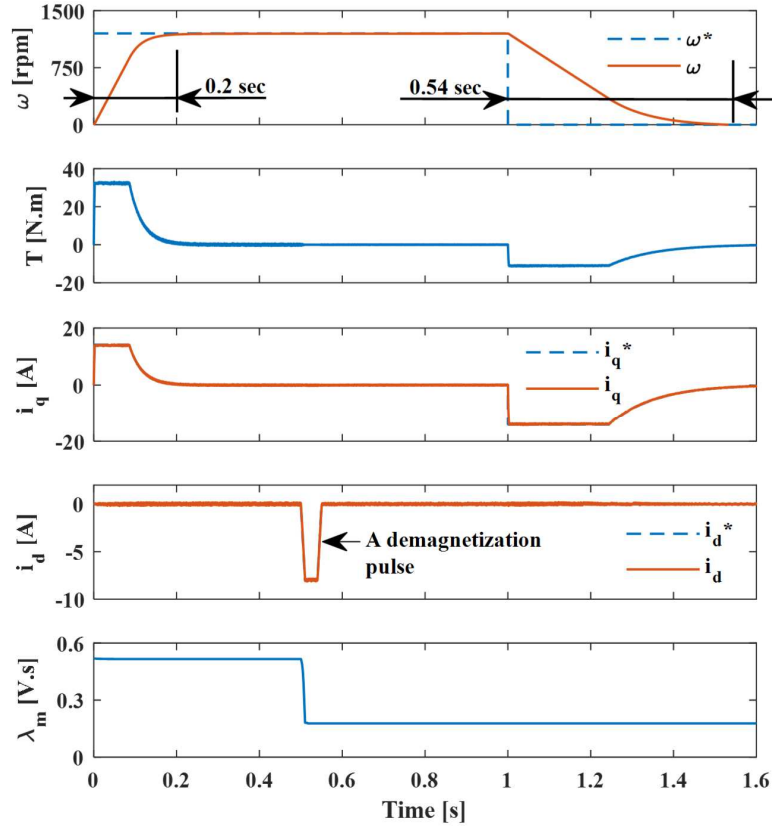
Fig. 5-1. A step change in motor speed at no load from zero to 1200 rpm and from 1200 rpm to zero. Illustration of deceleration time extension when the demagnetization occurs.

load. For example, from Fig. 5-3, at 2 and 3 per unit speed, less than 0.5 per unit *d*-axis current can be supplied, which, according to Fig. 5-2(a), does not magnetize the AlNiCo9 magnets at all. At 1 per unit speed, almost 0.75 per unit *d*-axis current is allowed, which, according to Fig. 5-2(a), magnetizes the magnets to 25%. Since the magnets are at 30% MS, therefore even at 1 per unit speed, the magnetization state of the magnets cannot be altered. However, at 0.75 per unit speed, a maximum of 1.11 per unit *d*-axis current is allowed which magnetizes the magnets to almost 50% MS. This roughly corresponds to 50% torque if *q*-axis current is at its rated value. Finally, at 0.5 per unit speed, a maximum of 1.75 per unit *d*-axis current can be injected, which magnetizes the magnets to almost 95% MS. Therefore, during deceleration, the braking torque can be maximized only at low speeds (below 0.5 per unit).

Waiting until the speed goes below 0.5 per unit to magnetize the magnets and to maximize the braking torque means that the braking time is not minimum especially when decelerating from high speeds, e.g. 2 or 3 per unit. On the other hand, exciting magnetization pulses as the speed decreases causes huge torque ripple which degrades the braking performance, apart from

81

not knowing the exact magnetizing current magnitude needed to be excited as the speed decreases. Therefore, the objective is to decide on the magnitude of the positive *d*-axis current that can maximize the braking torque within the inverter current and voltage limits, and ensure a smooth braking performance.
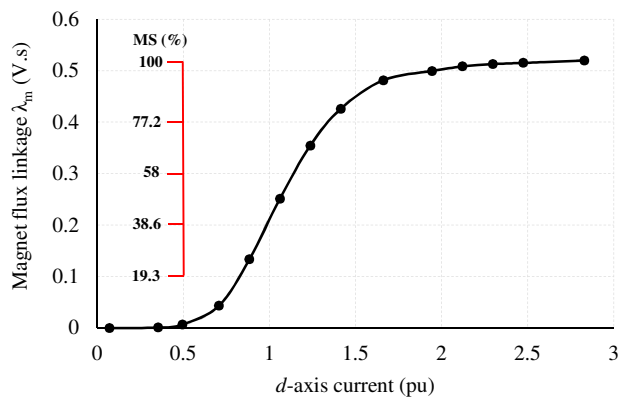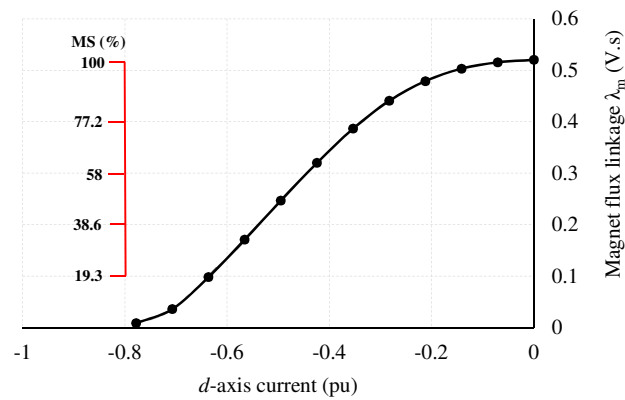
Fig. 5-2. Measured AlNiCo9 magnet flux linkage versus d-axis current: (a) magnetization curve, (b) demagnetization curve.
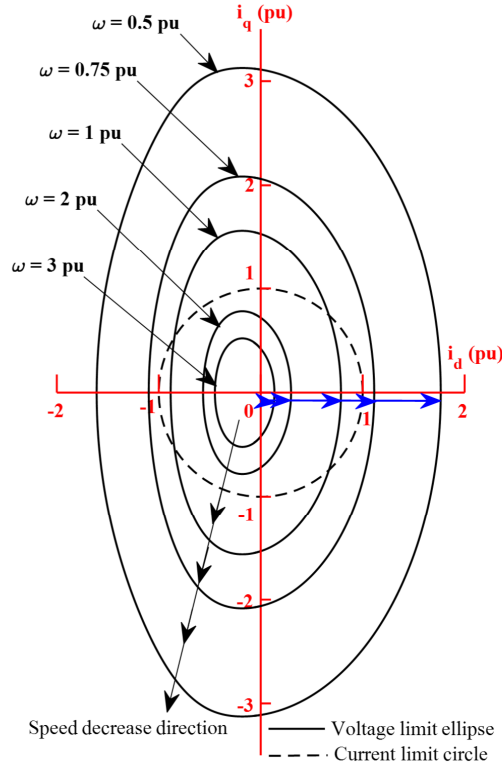
Fig. 5-3. Simulated voltage contours at different speeds and 30% magnetization state. The Illustration of the maximum allowable positive d-axis current as the motor decelerates is highlighted by the blue arrows.

Braking Scheme

The voltage limit and the output torque are defined by equations (5-1) and (5-2), respectively.

$$L_q^2 i_q^2 + (L_d i_d + \lambda_m)^2 = \left(\frac{V_\ell}{\omega}\right)^2 \tag{5-1}$$

$$T = \left(\frac{3P}{2}\right)\left[(L_d - L_q)i_d + \lambda_m\right]i_q \tag{5-2}$$

Solving the voltage limit equation for i_q and substituting it into the torque equation squared results in,

$$T^2 = \left(\frac{3P}{2L_q}\right)^2 \left[(L_d - L_q)i_d + \lambda_m\right]^2 \left[\left(\frac{V_\ell}{\omega}\right)^2 - (L_d i_d + \lambda_m)^2\right]. \tag{5-3}$$

By taking the derivative of (5-3) with respect to the *d*-axis current results in,

83

$$(L_d - L_q)[(V_\ell/\omega)^2 - (L_d i_d + \lambda_m)^2] - L_d(L_d i_d + \lambda_m)[(L_d - L_q)i_d + \lambda_m] = 0. \quad (5\text{-}4)$$

The solution of the quadratic equation (5-4) is,

$$i_d = \left(\frac{1}{4L_d^2}\right)\left\{-\lambda_m L_d\left[3 + \frac{1}{(1-\xi)}\right]\right.$$

$$\left. + \sqrt{\lambda_m^2 L_d^2[3 + 1/(1-\xi)]^2 - 8L_d^2\left[\frac{(2-\xi)}{(1-\xi)}\lambda_m^2 - \left(\frac{V_\ell}{\omega}\right)^2\right]}\right\}, \quad (5\text{-}5)$$

where ξ is the saliency ratio and equals to L_q/L_d. Equation (5-5) gives the amount of d-axis current needed to maximize the torque based on the voltage limit. Since the magnitude of this current increases as the speed decreases, it can exceed the inverter rated current. Therefore, the machine current during the braking transient should be limited to the inverted rated current. Hence, the d-axis current in equation (5-5) maximizes the braking torque even at higher speeds where its magnitude is fairly small, and as the speed decreases, its magnitude increases and starts magnetizing the magnets, which will maximize the braking torque even further.

Therefore, once braking is detected, the d-axis current command is decided by equation (5-5), and the q-axis current command is decided by the speed error $(\omega^* - \omega)$ through the proportional-integral controller. For now, the load current (q-axis current) is limited to not exceed the rated current of the machine I_s^r, and the total machine current i_s is limited to not exceed the rated inverter current I_{inv}^r. This allows the magnitude of the d-axis current to increase to a maximum of the rated inverter current during the braking transient in order to magnetize the low-H_c magnets.

Since braking is a transient operation, the reference machine voltages v_d^* and v_q^* might exceed the maximum available voltage by the inverter V_ℓ. This saturates the d- and q-axis currents regulators and sometimes results in the actual currents not following the commanded signals. To avoid this scenario, the reference voltages are compensated so that the total stator reference voltage V_s does not exceed the maximum available voltage from the inverter V_ℓ.

Fig. 5-4 shows the block diagram of the drive system. The front-end active rectifier control is given in detail in [105]. Its purpose is to prevent the prohibitive voltage rise of the DC link during the braking transient by recuperating the kinetic energy back to the mains. All

the controllers are proportional-integral based compensators. A space vector pulse modulation is adopted for better DC bus voltage utilization. The braking unit is highlighted by the red-dashed rectangle. The braking detector is a relay-based circuit, which can detect the braking operation based on the rate of change of the speed. Its output signal, which is either 1 (braking) or zero (no-braking), is multiplied by the output of the equation (5-5). The limiter ($L2$) has the following characteristics,

$$y = f(x) = \begin{cases} -i_d^{limit}, & for\ x < -i_d^{limit} \\ x, & for\ -i_d^{limit} \le x \le i_d^{limit} \\ i_d^{limit} & for\ x > i_d^{limit}, \end{cases} \tag{5-6}$$

in which,

$$i_d^{limit} = \sqrt{I_{inv}^{r\,2} - i_q^2}. \tag{5-7}$$
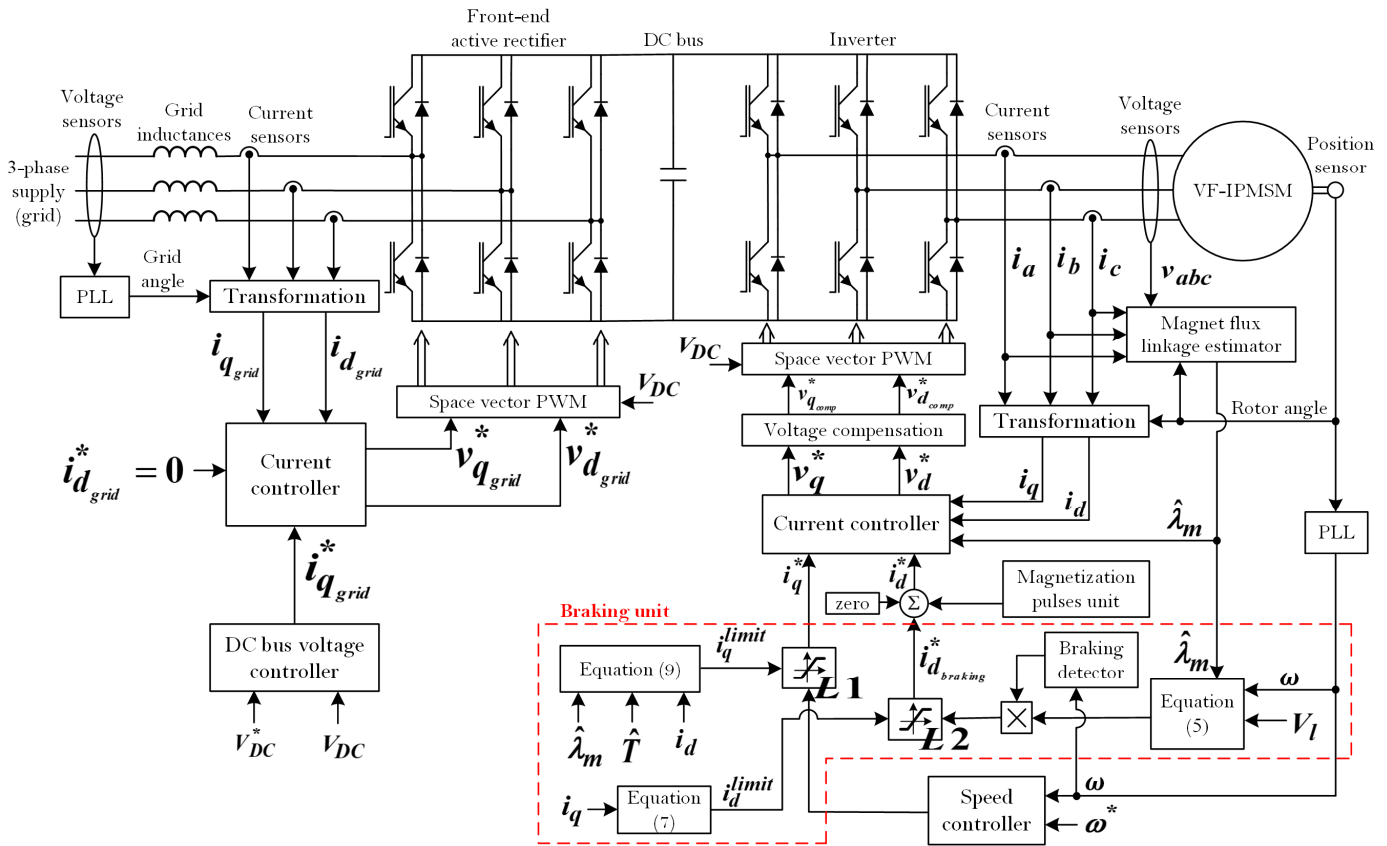
Fig. 5-4. Block diagram of the drive system.

Therefore, the limiter (*L2*) dynamically limits the reference *d*-axis braking current in preference to the *q*-axis current to not exceed the inverter rated current. The limiter (*L1*) is configured so that the reference *q*-axis current does not exceed the rated motor current.
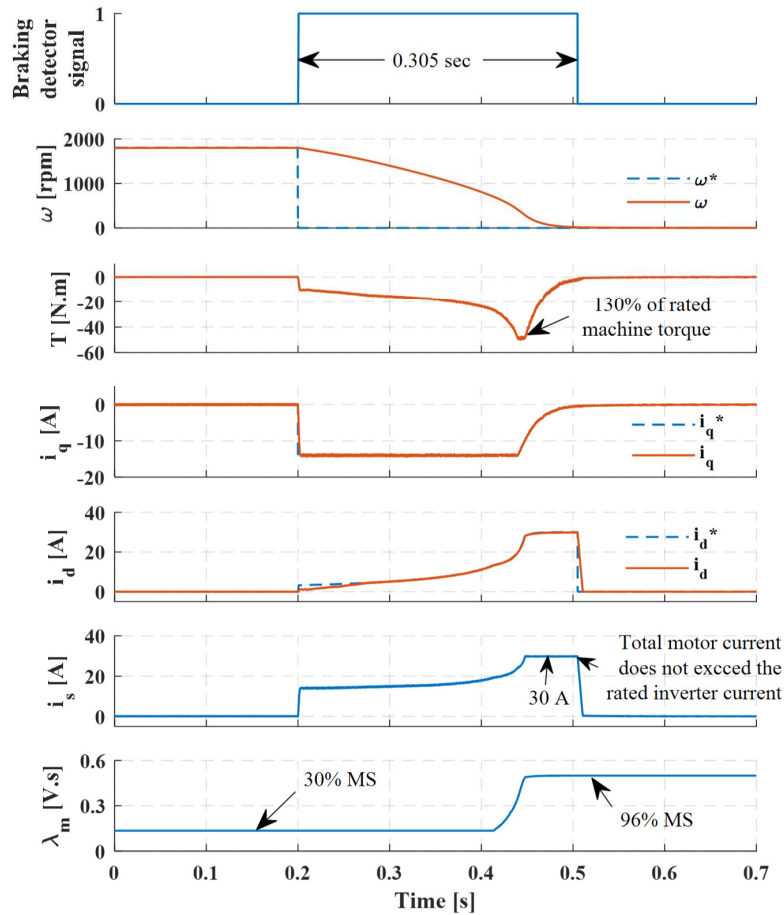
Fig. 5-5. A step change in motor speed at no load from 1800 rpm to zero. Illustration of harsh braking in minimal time via torque maximization using equation (5-5).

Fig. 5-5 demonstrates the dynamics during a step change in motor speed from twice the rated speed to zero. The magnets are initially demagnetized to almost 30% magnetization level. Once the braking is detected, the *d*-axis current required to maximize the torque based on the available voltage from the inverter is excited. It can be seen that the *q*-axis current is limited to the rated machine current (14.14 A), and the total motor current is limited to the rated inverter current (30 A). At almost half rated speed, the *d*-axis braking current starts magnetizing the magnets, and the torque increases rapidly and exceeds the rated motor torque (36 N.m). In order

86

to not exceed the rated motor torque during braking, the q-axis reference current limiter ($L1$) is adjusted to have the following characteristics,

$$y = f(x) = \begin{cases} -i_q^{limit}, & for \; x < -i_q^{limit} \\ x, & for -i_q^{limit} \le x \le i_q^{limit} \\ i_q^{limit} & for \; x > i_q^{limit}, \end{cases} \quad (5\text{-}8)$$

in which,

$$i_q^{limit} = \begin{cases} \dfrac{T_{rated}}{\dfrac{3}{2}\dfrac{P}{}\left[\lambda_m + (L_d - L_q)i_d\right]}, & for \; T_{rated} < T < -T_{rated} \\ I_s^r, & for -T_{rated} \le T \le T_{rated.} \end{cases} \quad (5\text{-}9)$$

Therefore, the upper and lower limits of the q-axis reference current are dynamically changed as per (5-9) so that the motor torque does not exceed the rated torque in all operating conditions including braking.

Fig. 5-6 demonstrates the same operating conditions simulated in Fig. 5-5 considering the dynamics of the limiter ($L1$) given by (5-8) and (5-9), where the reduction in q-axis current is highlighted by a circle. This action prevents the motor torque from exceeding the rated value during braking as seen in Fig. 5-6.

Experimental Verification

A 5 hp proof-of-concept variable flux IPMSM, which was proposed in [16], is used for experimental validation. The motor parameters are shown in Table 0-2 in the appendix. The block diagram of the system is shown in Fig. 5-4, and the experimental setup is shown in Fig. 5-7. The control is implemented on a real-time controller, Opal-RT OP5600 platform [59], with a sampling rate of 50 kS/s. A space vector pulse width modulation scheme with a 5 kHz switching frequency is utilized for both converters. The magnet flux linkage and the electromagnetic torque are estimated online as in chapter 3 [89]. The two-level front-end active rectifier regulates the DC link to 600 V.

Fig. 5-8 demonstrates a step change in motor speed from 1800 rpm (2 per unit) to zero speed at no load and 40% magnetization level without applying the proposed minimal-time braking scheme. During braking, it can be seen that the speed controller is maximizing the q-axis current, which is limited to the rated motor current, and the d-axis current is controlled to
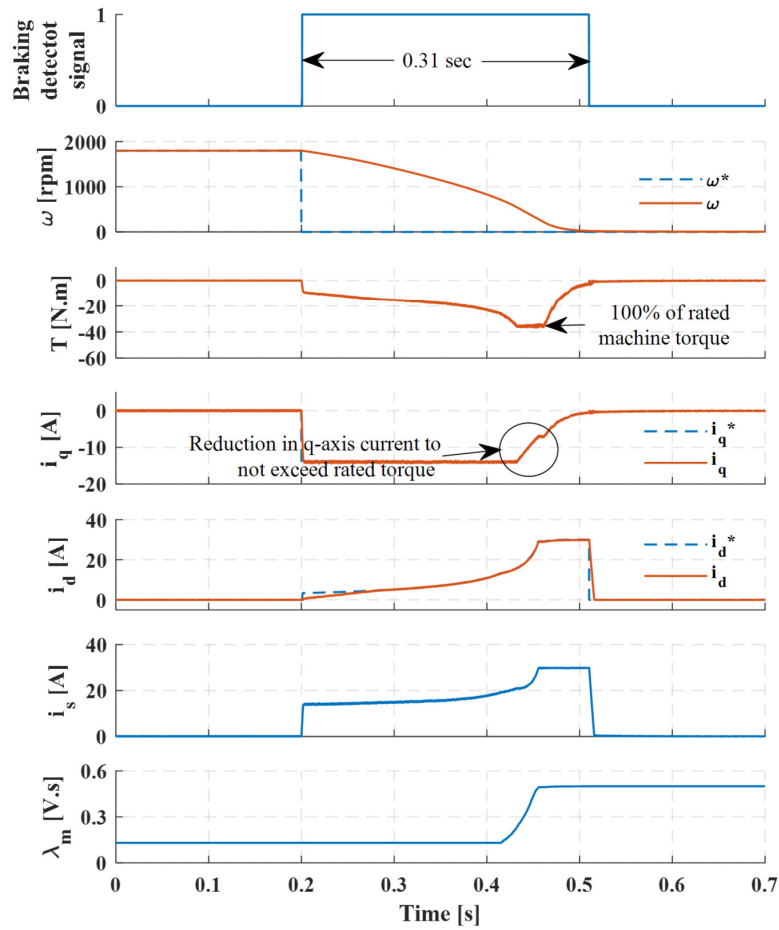
Fig. 5-6. Simulated the same operating conditions in Fig. 5 taking into consideration the dynamics of the limiter (*L*1) given by equations (5-8) and (5-9) in order to not exceed the rated motor torque during braking.
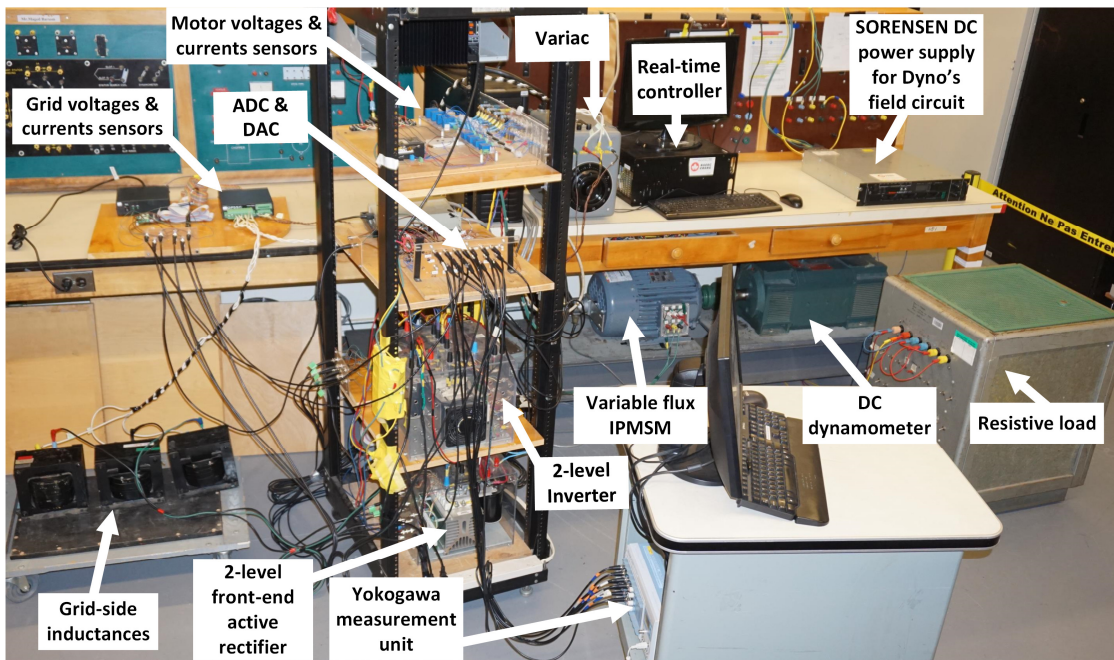
Fig. 5-7. Experimental setup.

be zero. The magnets are demagnetized to 40% magnetization level, this results in the output torque not being maximized and the motor stops in 1.76 seconds. Also, from Fig. 5-8, it can be noticed that the DC link is controlled via the front-end active rectifier at 600 V. Moreover, during braking, the grid phase voltage and current are out of phase, which means that the braking energy is fed back to the mains. This is further illustrated by the sign change of the grid q-axis current, from positive to negative as seen in Fig. 5-8.
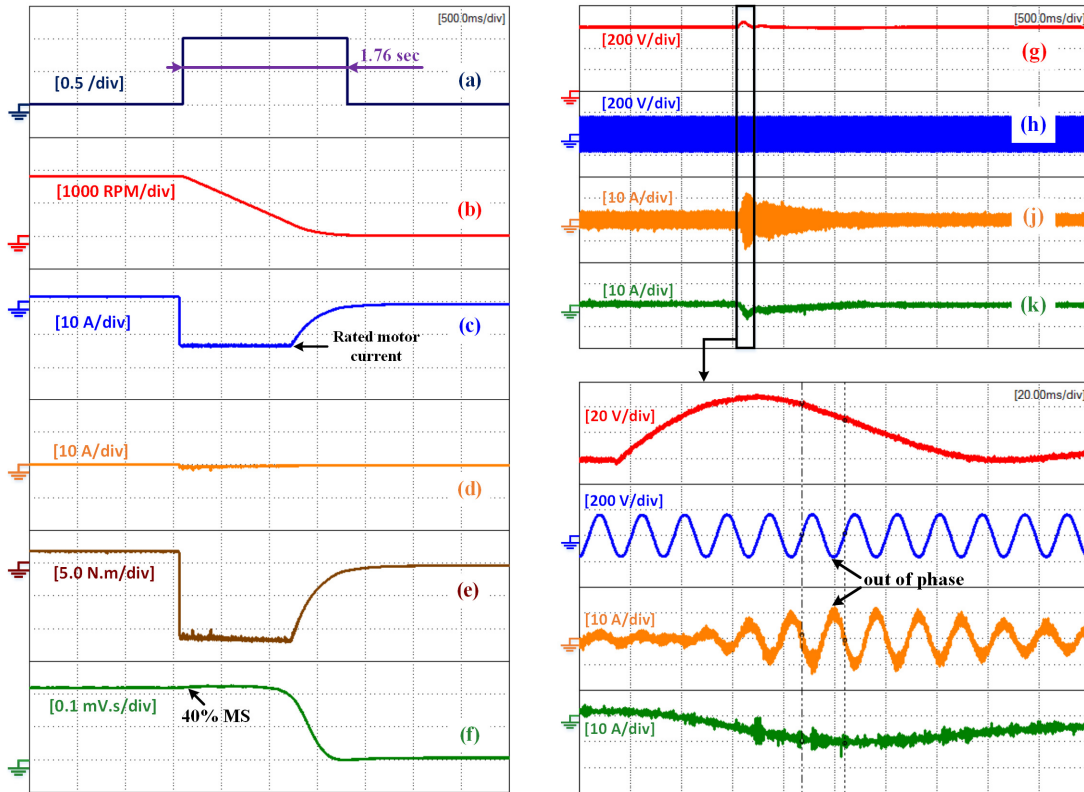
Fig. 5-8. A step change in motor speed form double base speed (1800 RPM) to zero at no load and 40% mgnetization state: (a) braking detector signal, (b) speed, (c) q-axis current, (d) d-axis current, (e) estimated torque, (f) estimated magnet flux linkage, (g) DC link voltage, (h) grid phase voltage, (j) grid phase current, (k) grid q-axis current.

In Fig. 5-9, the proposed minimal-time braking scheme is activated. It can be seen that during braking, the d-axis current is injected based on equation (5-5) to maximize the braking torque considering the voltage limit. The q-axis current is decided by the speed controller, and it is limited to the rated motor current as long as the torque is within the rated value. Moreover, once the magnets start being magnetized, the torque tends to exceed its rated value. At this moment, the q-axis current limiter ($L1$) operates to reduce the q-axis current in order to keep the torque within its rated value. During these dynamics, the magnets are magnetized from 40%

to almost 94% magnetization level, and the motor stops in 1.06 seconds, which is almost 40% less time than the previous case, which is depicted by Fig. 5-8.
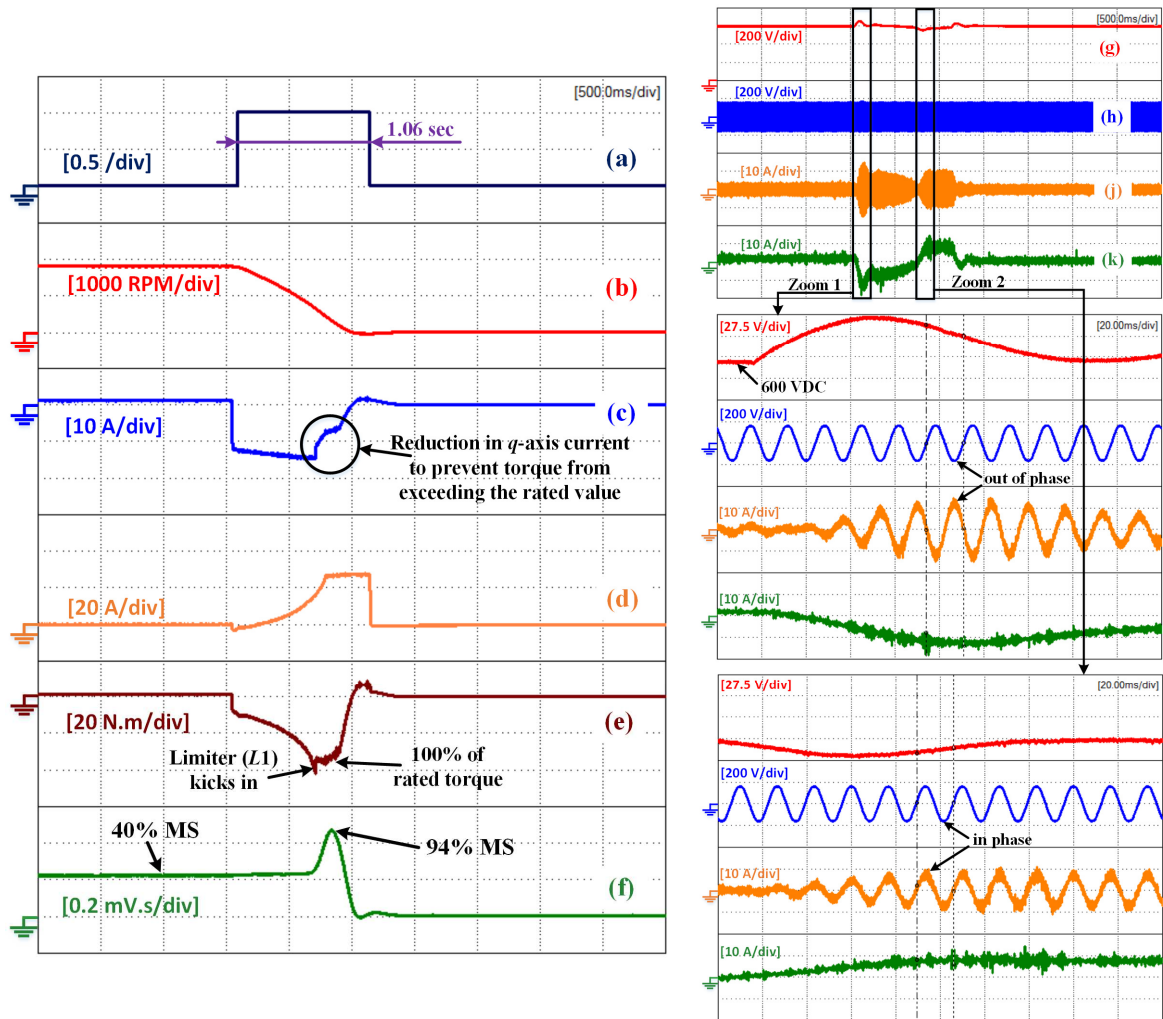
Fig. 5-9. Illustration of minimal-time braking. A step change in motor speed form double base speed (1800 RPM) to zero at no load and 40% magnetization state: (a) braking detector signal, (b) speed, (c) q-axis current, (d) d-axis current, (e) estimated torque, (f) estimated magnet flux linkage, (g) DC link voltage, (h) grid phase voltage, (j) grid phase current, (k) grid q-axis current.

In addition, and as in the previous case, the grid phase voltage and current are out of phase during braking, which illustrates the braking energy being fed back to the mains. Moreover, once the magnets are being magnetized by the increasing *d*-axis current as the speed decreases, the grid phase voltage and current are in phase, which means that the energy needed for magnetizing the low-H_c magnets is supplied from the mains to the motor. This can also be noticed by the sign change of the grid *q*-axis current, first from positive to negative and then

back to positive again. The DC link is controlled to 600 V with the recorded variation being less than 10% during the transient braking operation.

Fig. 5-10 shows the *dq*-axis currents, magnet flux linkage, and torque trajectories during severe braking (from 1800 RPM to zero) in minimal-time at different loading conditions and 40% magnetization level. It can be seen that the *q*-axis current is within the rated machine current, and the total machine current is within the rated inverter current. It is worth mentioning that the rated inverted current is 30 A, and in the experiment, the total machine current is limited to 27 A as a safety precaution. As a result, during braking, the magnets are magnetized to almost 94% instead of 96% at rated inverted current. Moreover, from Fig. 5-10, it can be seen that the as the load increases the braking time decreases which means that the load torque supports the machine torque during braking.
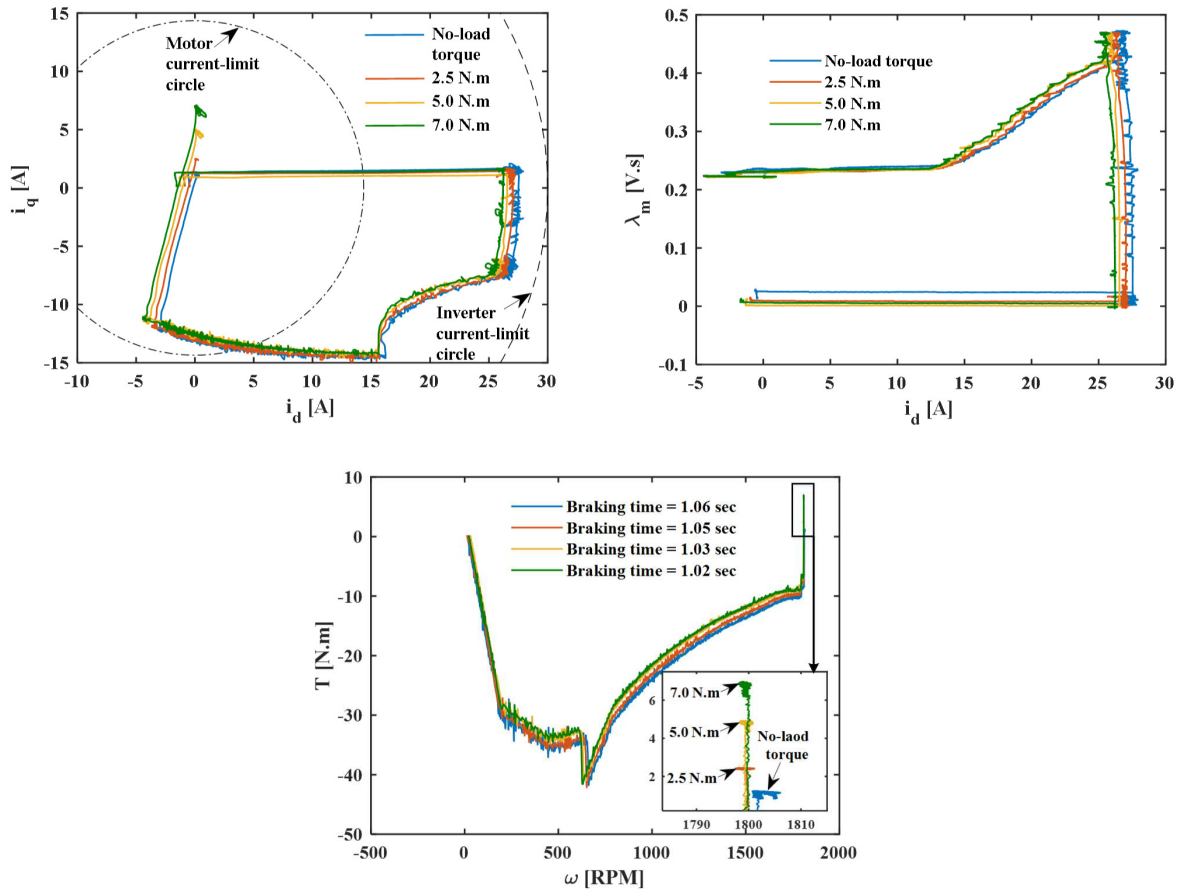
Fig. 5-10. Motor Currents, rotor flux linkage, and torque trajectories during minimal-time braking from twice base speed (1800 RPM) to zero at different loading conditions.

Summary

In this chapter, the issue of minimal time braking from high speeds with variable flux-intensifying IPMSMs has been illustrated. A simple but effective minimal-time braking algorithm has been proposed with energy regeneration. The proposed algorithm enables the use of d-axis current to magnetize the magnets and maximize the braking torque within the inverter voltage and current limits. It is based on a field-oriented vector control, and it demonstrates an excellent dynamic braking performance under different loading conditions using a speed controlled drive system.

Chapter 6. Conclusions and Future Work

Conclusions

Based on the work presented on the variable-flux interior permanent magnet synchronous motors in this thesis, the following can be stated;

1. A review of rotor flux linkage estimation techniques in chapter 1 showed that a full-rank machine model is required for accurately estimating the rotor flux linkage. Since the *dq*-model of the machine is known for rank-deficiency for simultaneously estimating the resistance, *dq*-axis inductances, and the rotor flux linkage, two out of these four parameters have to be measured prior to the estimation of the other two parameters from the *dq*-model of the machine. Therefore, in the proposed rotor flux linkage estimator in chapter 3, the stator resistance and the *d*-axis inductance are measured prior to rotor flux linkage estimation.

2. The review also showed that an offline measured look-up table of rotor flux linkage versus current cannot predict the actual magnetization state of the magnets online. A certain current is needed to demagnetize/re-magnetize the low-coercivity magnets depends on machine parameters which are varying based on the machine operating condition. In addition, the review showed that the current pulse excitation method for magnetization causes non uniform variable flux distribution in the air-gap. Therefore, a sophisticated method for rotor flux estimation based on harmonics extraction is presented in chapter 3 for variable-flux IPM synchronous machines.

3. In chapter 3 an online rotor flux linkage estimator was developed, in which a modified adaptive nonlinear filter was utilized to instantaneously estimate the amplitude, phase, and frequency of the back emf harmonics. It was shown that in order to overcome the tradeoff between the convergence speed and the steady state error of the filter response, a variable step size is needed.

4. The conducted study on the machine operating envelopes, which was presented in chapter 4, showed the superiority of using a continuous negative d-axis current in the flux weakening region over demagnetization pulses in enhancing the machine output characteristics. Also, it showed that the output power of the machine cannot be held constant in the flux weakening region due the irreversible demagnetization of the low-H_c magnets. However, the simulated results showed that the output power can be enhanced via saliency manipulation.

5. Despite the output power reduction of the machine, the irreversible demagnetizations of the low-H_c magnets reduces the amount of negative d-axis current needed in the high-speed region compared to the rare-earth IPM synchronous machine. This results in iron and copper losses reduction and improved machine efficiency in the high-speed region compared to the rare-earth IPM synchronous machine.

6. The irreversible demagnetization of the low-H_c magnets in the high-speed region results in severe braking not being done in minimal time. An analytical solution to the amount of magnetizing current needed to be injected to magnetize the magnets and maximize the braking torque in order to achieve minimal-time braking was presented in chapter 5.

Future Work

1. A closed-loop magnetization state controller can be developed, in which the estimated rotor flux linkage, as in chapter 3, can be treated as an actual signal.

2. This can further be improved by operating the machine to obtain the best efficiency in all operating conditions by selecting the rotor flux reference signal from the measured efficiency map of the machine.

3. The proposed flux estimator in chapter 3 can be used for testing the effect of exciting different magnetization pulse shapes on the uniformity of the air-gap flux distribution by means of harmonics comparison.

4. The braking in minimal-time for normal saliency variable-flux IPMSM is challenging. This is because the resultant reluctance torque out of the magnetizing current opposes the magnet braking torque. Thus, the braking torque is not maximized, which makes the minimal time braking not feasible or more challenging.

References

[1] "Global EV outlook 2017, two million and counting," Iternational Energy Agency, 2017. [Online]. Available: https://www.iea.org/publications/freepublications/publication/GlobalEVOutlook2017.pdf.

[2] "2016 Vehicle technologies market report," Oak Ridge National Laboratory, U.S. Department of Energy, 2016. [Online]. Available: https://info.ornl.gov/sites/publications/files/Pub74587.pdf.

[3] "Running on electricity in Québec," [Online]. Available: http://vehiculeselectriques.gouv.qc.ca/ english/particuliers/vehicules-electriques.asp. [Accessed 1 February 2016].

[4] Z. Q. Zhu, W. Q. Chu and Y. Guan, "Quantitative comparison of electromagnetic performance of electrical machines for HEVs/EVs," *CES Trans. on Electrical Machines and Systems,* vol. 1, no. 1, p. 37–47, Mar. 2017.

[5] Z. Q. Zhu and C. C. Chan, "Electrical machine topologies and technologies for electric, hybrid, and fuel cell vehicles," in *IEEE Vehicle Power and Propulsion Conf.*, Harbin, China, 2008.

[6] J. Santiago, H. Bernhoff, B. Ekergård, S. Eriksson, S. Ferhatovic, R. Waters and M. Leijon, "Electrical motor drivelines in commercial all-electric vehicles: a review," *IEEE Trans. on Vehicular Technology,* vol. 61, no. 2, p. 475–484, Feb. 2012.

[7] P. Pillay and R. Krishnan, "Application characteristics of permanent magnet synchronous and brushless DC motors for servo drives," *IEEE Trans. on Ind. Appl.,* vol. 27, no. 5, p. 986–996, Sept.-Oct. 1991.

[8] A. M. El-Refaie, "Motors/generators for traction/ propulsion applications: a review," *IEEE Vehicular Technology Magazine,* vol. 8, no. 1, p. 90–99, Mar. 2013.

[9] "UQM TECHNOLOGIES," [Online]. Available: https://www.uqm.com/English/home/ default.aspx. [Accessed 29 Mar. 2018].

[10] "Green Car Congress," [Online]. Available: http://www.greencarcongress.com/2016/06/ 20160615-accord.html. [Accessed 29 Mar. 2018].

[11] "MOTOR TREND," [Online]. Available: http://www.motortrend.com/cars/honda/accord/ 2006/hybrid-sedan-comparison/. [Accessed 29 Mar. 2018].

[12] V. Ostovic, "Memory Motors," *IEEE Ind. Appl. Magazine,* vol. 9, no. 1, p. 52–61, Jan.-Feb. 2003.

[13] K. Sakai and K. Yuuki, "Permanent-magnet-type rotating electrical machine and permanent magnet motor drive system". US Patent US 2010/0327689 A1, 30 Dec. 2010.

[14] N. Limsuwan, T. Kato, K. Akatsu and R. D. Lorenz, "Design and evaluation of a variable-flux flux-intensifying interior permanent magnet machine," *IEEE Trans. on Ind. Appl.,* vol. 50, no. 2, p. 1015–1024, Mar.-Apr. 2014.

[15] M. Ibrahim, L. Masisi and P. Pillay, "Design of high torque density variable flux permanent magnet machine using alnico magnets," *IEEE Trans. on Ind. Appl.,* vol. 51, no. 6, p. 4482–4491, Nov.-Dec. 2015.

[16] M. Ibrahim, L. Masisi and P. Pillay, "Design of Variable Flux Permanent-Magnet Machine for Reduced Inverter Rating," *IEEE Trans. on Ind. Appl.,* vol. 51, no. 5, p. 3666–3674, Apr. 2015.

[17] L. Masisi and P. Pillay, "Control strategy of a variable flux machine using AlNiCo permanent magnets," in *Energy Conv. Congress and Expo. (ECCE)*, Montreal, 2015.

[18] R. Krishnan and P. Vijayraghavan, "Fast estimation and compensation of rotor flux linkage in permanent magnet synchronous machines," in *Proc. of the IEEE Int. Symp. on Ind. Electronics (ISIE)*, Bled, 1999.

[19] S. Ichikawa, M. Tomita, S. Doki and S. Okuma, "Sensorless control of permanent-magnet synchronous motors using online parameter identification based on system identification theory," *IEEE Trans. on Ind. Electronics,* vol. 53, no. 2, p. 363–372, Apr. 2006.

[20] K. Liu, Z. Q. Zhu and D. A. Stone, "Parameter estimation for condition monitoring of PMSM stator Winding and rotor permanent magnets," *IEEE Trans. on Ind. Electronics,* vol. 60, no. 12, p. 5902–5913, Dec. 2013.

[21] T. Boileau, N. Leboeuf, B. Nahid-Mobarakeh and F. Meibody-Tabar, "Online identification of PMSM parameters: parameter identifiability and estimator comparative study," *IEEE Trans. on Ind. Appl.,* vol. 47, no. 4, p. 1944–1957, July-Aug. 2011.

[22] K. Liu, Q. Zhang, J. T. Chen, Z. Q. Zhu, J. Zhang and A. Shen, "Online multiparameter estimation of non-salient pole PM synchronous machines with temperature variation tracking," *IEEE Trans. on Ind. Electronics,* vol. 58, no. 5, p. 1776–1788, May 2011.

[23] Y. Shi, K. Sun, L. Huang and Y. Li, "Online identification of permanent magnet flux based on extended Kalman filter for IPMSM drive with position sensorless control," *IEEE Trans. on Ind. Electronics,* vol. 59, no. 11, p. 4169–4178, Nov. 2012.

[24] M. N. Uddin and M. M. I. Chy, "Online parameter-estimation-based speed control of PM AC motor drive in flux-weakening region," *IEEE Trans. on Ind. Appl.,* vol. 44, no. 5, p. 1486–1494, Sep.-Oct. 2010.

[25] M. Rashed, P. F. A. MacConnell, A. F. Stronach and P. Acarnley, "Sensorless indirect-rotor-field-orientation speed control of a permanent-magnet synchronous motor with stator-resistance estimation," *IEEE Trans. on Ind. Electronics,* vol. 54, no. 3, p. 1664–1675, June 2007.

[26] L. Liu and D. A. Cartes, "Synchronisation based adaptive parameter identification for permanent magnet synchronous motors," *IET Control Theory & Appl.,* vol. 1, no. 4, p. 1015–1022, July 2007.

[27] B. Nahid-Mobarakeh, F. Meibody-Tabar and F. -M. Sargos, "Mechanical sensorless control of PMSM with online estimation of stator resistance," *IEEE Trans. on Ind. Appl.,* vol. 40, no. 2, p. 457–471, Mar.-Apr. 2004.

[28] X. Xiao, C. Chen and M. Zhang, "Dynamic permanent magnet flux estimation of permanent magnet synchronous machines," *IEEE Trans. on Applied Superconductivity,* vol. 20, no. 3, p. 1085–1088, June 2010.

[29] M. A. Hamida, J. D. Leon, A. Glumineau and R. Boisliveau, "An adaptive interconnected observer for sensorless control of PM synchronous motors with online parameter identification," *IEEE Trans. on Ind. Electronics,* vol. 60, no. 2, p. 739–748, Feb. 2013.

[30] G. Gatto, I. Marongiu and A. Serpi, "Discrete-time parameter identification of a surface-mounted permanent magnet synchronous machine," *IEEE Trans. on Ind. Electronics,* vol. 60, no. 11, p. 4869–4880, Nov. 2013.

[31] Z. Q. Zhu, X. Zhu and P. D. Sun, "Estimation of winding resistance and PM flux-linkage in brushless AC machines by reduced-order extended Kalman Filter," in *IEEE Int. Conf. on Networking, Sensing and Control*, London, 2007.

[32] K. W. Lee, D. H. Jung and I. J. Ha, "An online identification method for both stator resistance and back-EMF coefficient of PMSMs without rotational transducers," *IEEE Trans. Ind. Electronics,* vol. 51, no. 2, p. 507–510, Apr. 2004.

[33] S. J. Underwood and I. Husain, "On-line parameter estimation and adaptive control of permanent magnet synchronous machines," *IEEE Trans. on Ind. Electronics,* vol. 57, no. 7, p. 2435–2443, July 2010.

[34] S. B. Lee and T. G. Habetler, "An online stator winding resistance estimation technique for temperature monitoring of line-connected induction machines," *IEEE Trans. on Ind. Appl.,* vol. 39, no. 3, p. 685–694, May-June 2003.

[35] K. Liu and Z. Q. Zhu, "Online estimation of the rotor flux linkage and voltage-source inverter nonlinearity in permanent magnet synchronous machine drives," *IEEE Trans. on Power Electronics,* vol. 29, no. 1, p. 418–427, Jan. 2014.

[36] K. Liu and Z. Q. Zhu, "Quantum genetic algorithm-based parameter estimation of PMSM under variable speed control accounting for system identifiability and VSI nonlinearity," *IEEE Trans. on Ind. Electronics,* vol. 62, no. 4, p. 2363–2371, Apr. 2015.

[37] K. Liu and Z. Q. Zhu, "Mechanical parameter estimation of permanent-magnet synchronous machines with aiding from estimation of rotor PM flux linkage," *IEEE Trans. on Ind. Appl.,* vol. 51, no. 4, p. 3115–3125, July-Aug. 2015.

[38] K. Liu and Z. Q. Zhu, "Position-offset-based parameter estimation using the Adaline NN for condition monitoring of permanent-magnet synchronous machines," *IEEE Trans. on Ind. Electronics,* vol. 62, no. 4, p. 2372–2383, Apr. 2015.

[39] A. Piippo, M. Hinkkanen and J. Luomi, "Adaptation of motor parameters in sensorless PMSM drives," *IEEE Trans. on Ind. Appl.,* vol. 45, no. 1, p. 203–212, Jan.-Feb. 2009.

[40] S. Morimoto, M. Sanada and Y. Yakeda, "Mechanical sensorless drives of IPMSM with online parameter identification," *IEEE Trans. on Ind. Appl.,* vol. 42, no. 5, p. 1241–1248, Sept.-Oct. 2006.

[41] J. D. a. Z. L. M. A. Jabbar, "Determination of machine parameters for internal permanent magnet synchronous motors," in *2nd Int. Conf. on Power Electronics, Machines, and Drives (PEMD)*, Edinburgh, 2004.

[42] D. D. Reigosa, F. Briz, P. Gacia, J. M. Guerrero and M. W. Degner, "Magnet temperature estimation in surface PM machines using high-frequency signal injection," *IEEE Trans. on Ind. Appl.,* vol. 46, no. 4, p. 1468–1475, July-Aug. 2010.

[43] K. H. Kim and M. J. Youn, "A nonlinear speed control for a PM synchronous motor using a simple disturbance estimation technique," *IEEE Trans. on Ind. Electronics,* vol. 49, no. 3, p. 524–535, June 2002.

[44] D. D. Reigosa, D. Fernandez, Z. Q. Zhu and F. Briz, "PMSM magnetization state estimation based on stator-reflected PM resistance using high-frequency signal injection," *IEEE Trans. on Ind. Appl.,* vol. 51, no. 5, p. 3800–3810, Sept.-Oct. 2015.

[45] D. D. Reigosa, F. Briz, M. W. Degner, P. Garcia and J. M. Guerrero, "Magnet temperature estimation in surface PM machines during six-step operation," *IEEE Trans. on Ind. Appl.,* vol. 48, no. 6, p. 2353–2361, Nov.-Dec. 2012.

[46] D. D. Reigosa, F. Briz, M. W. Degner, P. Garcia and J. M. Guerrero, "Temperature issues in saliency-tracking-based sensorless methods for PM synchronous machines," *IEEE Trans. on Ind. Appl.,* vol. 47, no. 3, p. 1352–1360, May-June 2011.

[47] D. D. Reigosa, D. Fernandez, H. Yoshida, T. Kato and F. Briz, "Permanent-magnet temperature estimation in PMSMs using pulsating high-frequency current injection," *IEEE Trans. on Ind. Appl.,* vol. 51, no. 4, p. 3159–3168, July-Aug. 2015.

[48] N. Bianchi and S. Bolognani, "Influence of rotor geometry of an interior PM motor on sensorless control feasibility," in *IAS Annual Meeting Conf.*, Kowloon, 2005.

[49] J. M. Guerrero, M. Leetmaa, F. Briz, A. Zamarron and R. D. Lorenz, "Inverter nonlinearity effects in high-frequency signal-injection-based sensorless control methods," *IEEE Trans. on Ind. Appl.,* vol. 41, no. 2, p. 618–626, Mar.-Apr. 2005.

[50] J. W. Choi and S. K. Sul, "A new compensation strategy reducing voltage/current distortion in PWM VSI systems operating with low output voltages," *IEEE Trans. on Ind. Appl.,* vol. 31, no. 5, p. 1001–1008, Sept.-Oct. 1995.

[51] D. Reigosa, D. Fernandez, T. Tanimoto, T. Kato and F. Briz, "Comparative analysis of BEMF and pulsating high-frequency current injection methods for PM temperature estimation in PMSMs," *IEEE Trans. on Power Electronics,* vol. 32, no. 5, p. 3691–3699, May 2017.

[52] C. Y. Yu, T. Fukushige, N. Limsuwan, T. Kato, D. D. Reigosa and R. D. Lorenz, "Variable-flux machine torque estimation and pulsating torque mitigation during magnetization state manipulation," *IEEE Trans. on Ind. Appl.,* vol. 50, no. 5, p. 3414–3422, Sept.-Oct. 2014.

[53] H. Kim, M. Youn, K. Cho and H. Kim, "Nonlinearity estimation and compensation of PWM VSI for PMSM under resistance and flux linkage uncertainty," *IEEE Trans. on Control Systems Technology,* vol. 14, no. 4, p. 589–601, July 2006.

[54] A. M. Aljehaimi and P. Pillay, "Online rotor flux linkage estimation for a variable flux Interior permanent magnet synchronous machine operating at different flux density levels," in *IEEE Int. Conf. on Power Electronics, Drives and Energy Systems (PEDES)*, Trivandrum, 2016.

[55] S. D. Wilson, P. Stewart and B. P. Taylor, "Methods of resistance estimation in permanent magnet synchronous motors for real-time thermal management," *IEEE Trans. on Energy Conv.,* vol. 25, no. 3, p. 698–707, Sept. 2010.

[56] A. R. Munoz and T. A. Lipo, "On-line dead-time compensation technique for open-loop PWM-VSI drives," *IEEE Trans. on Power Electronics,* vol. 14, no. 4, p. 683–689, July 1999.

[57] H. Hua, Z. Q. Zhu, A. Pride, R. P. Deodhar and T. Sasaki, "A novel variable flux memory machine with series hybrid magnets," *IEEE Trans. on Ind. Appl.,* vol. 53, no. 5, p. 4396–4405, Sept.-Oct. 2017.

[58] P. Pillay and R. Krishnan, "Modeling, simulation, and analysis of permanent-magnet motor drives, Part I: The permanent-magnet synchronous motor drive," *IEEE Trans. on Ind. Appl.,* vol. 25, no. 2, p. 265–273, Mar.-Apr. 1989.

[59] "OP5600 V2 User Manual, Real-Time Simulator," OPAL-RT Technologies, Inc., Montreal, 2016.

[60] P. Pillay and R. Krishnan, "Control characteristics and speed controller design for a high performance permanent magnet synchronous motor drive," *IEEE Trans. on Power Electronics,* vol. 5, no. 2, p. 151–159, Apr. 1990.

[61] H. Kim, K. Kim and M. Youn, "On-Line dead-time compensation method based on time delay control," *IEEE Trans. on Control Systems Technology,* vol. 11, no. 2, p. 279–285, Mar. 2003.

[62] Y. Park and S. Sul, "A novel method utilizing trapezoidal voltage to compensate for inverter nonlinearity," *IEEE Trans. on Power Electronics,* vol. 27, no. 12, p. 4837–4846, Dec. 2012.

[63] A. K. Ziarai and A. Konard, "A nonlinear adaptive method of elimination of power line interference in ECG signals," *IEEE Trans. on Biomedical Engineering,* vol. 49, no. 6, p. 540–547, Aug. 2002.

[64] H. Douglas, P. Pillay and A. K. Ziarani, "A new algorithm for transient motor current signature analysis using wavelets," *IEEE Trans. on Ind. Appl.,* vol. 40, no. 5, p. 1361–1368, Sep.-Oct. 2004.

[65] A. K. Zairani, "Extraction of nonstaionary sinusoids," *Ph.D. dissertation, Dept. of Electrical and Computer Engineering, Univ. of Toronto, Toronto, ON, Canada,* 2002 [Online]. Available: http://hdl.handle.net/1807/69155..

[66] J. Barzilai and J. M. Borwein, "Two-point step size gradient methods," *IMA Trans. of Numerical Analysis,* vol. 8, p. 141–148, Jan. 1988.

[67] G. T. e. PLANTI, "Determining parameters of a three phase permanent magnet synchronous machine using concontrol single phase voltage source," *PRZEGLAD ELEKTROTECHNICZNY (Electrical Review),* vol. 87, p. 137–140, 2011.

[68] R. Dutta and M. F. Rahman, "A comparative analysis of two test methodsof measuring d- and q-axes inductances of interior permanent-magnet machine," *IEEE Trans. on Magnetics,* vol. 42, no. 11, p. 3712–3718, Oct. 2006.

[69] R. Thike and P. Pillay, "Vector controlled drive to measure inductances of variable flux machine," in *IEEE Int. Conf. on Power Electronics, Drives and Energy Systems (PEDES)*, Trivandrum, 2016.

[70] J. Hendershot and T. Miller, "Numbers of slots and poles," in *Design of brushless permanent magnet machines*, 2nd edition ed., Motor Design Books, 2010.

[71] Caruso, A. O. D. Tommaso, R. Mastromauro, R. Miceli, R. Rizzo and F. Viola, "Cogging torque comparison of interior permanent magnet synchronous generators with different stator windings," in *6th Int. Conf. on Clean Electrical Power (ICCEP)*, Santa Margherita Ligure, 2017.

[72] J. Potgieter and M. Kamper, "Torque and voltage quality in design optimization of low-cost non-overlap single layer winding permanent magnet wind generator," *IEEE Trans. on Ind. Electronics,* vol. 59, no. 5, p. 2147–2156, May 2012.

[73] T. M. Jahns, "Flux-weakening regime operation of an interior permanent-magnet synchronous motor drive," *IEEE Trans. on Ind. Appl.,* Vols. IA-23, no. 4, p. 681–689, July-Aug. 1987.

[74] V. Ostovic, "Memory Motors," *IEEE Magazine on Ind. Appl.,* vol. 9, no. 1, p. 52–61, Jan.-Feb. 2003.

[75] R. Owen, Z. Q. Zhu, J. B. Wang, D. A. Stone and I. Urquhart, "Review of variable-flux permanent magnet machines," in *Int. Conf. on Elec. Machines and Systems*, Beijing, 2011.

[76] T. Fukushige, N. Limsuwan, T. Kato, K. Akatsu and R. D. Lorenz, "Efficiency contours and loss minimization over a driving cycle of a variable flux-intensifying machine," *IEEE Trans. on Ind. Appl.,* vol. 51, no. 4, p. 2984–2989, July-Aug. 2015.

[77] N. Limsuwan, T. Kato, K. Akatsu and R. D. Lorenz, "Design and evaluation of a variable-flux flux-intensifying interior permanent magnet machine," *IEEE Trans. on Ind. Appl.,* vol. 50, no. 2, p. 1015–1024, Mar.-Apr. 2014.

[78] M. Ibrahim, L. Masisi and P. Pillay, "Design of variable flux permanent-magnet machine for reduced inverter rating," *IEEE Trans. on Ind. Appl.,* vol. 51, no. 5, p. 3666–3674, Apr. 2015.

[79] A. M. Aljehaimi and P. Pillay, "Torque and power improvement for a variable flux permanent magnet synchronous machine," in *IEEE Transportation Electrification Conf. and Expo. (ITEC),* Chicago, 2017.

[80] Y. Zhou, Y. Chen and J. Shen, "Analysis and improvement of a hybrid permanent-magnet memory motor," *IEEE Trans. on Energy Conv.,* vol. 31, no. 3, p. 915–923, Sept. 2016.

[81] H. Hua, Z. Q. Zhu, A. Pride, R. P. Deodhar and T. Sasaki, "A novel variable flux memory machine with series hybrid magnets," *IEEE Trans. on Ind. Appl.,* vol. 53, no. 5, p. 4396–4405, Sept.-Oct. 2017.

[82] A. Athavale, K. Sasaki, B. S. Gagas, T. Kato and R. D. Lorenz, "Variable flux permanent magnet synchronous machine (VF-PMSM) design methodologies to meet electric vehicle traction requirements with reduced losses," *IEEE Trans. on Ind. Appl.,* vol. 53, no. 5, p. 4318–4326, Sept.-Oct. 2017.

[83] K. H. Nam, "AC Motor Control and Electric Vehicle Applications," New York: Taylor and Francis Group, 2010.

[84] S. Morimoto, Y. Takeda, T. Hirasa and K. Taniguchi, "Expansion of operating limits for permanent magnet motor by current vector control considering inverter capacity," *IEEE Trans. on Ind. Appl.,* vol. 26, no. 5, p. 866–871, Sept.-Oct. 1990.

[85] B. S. Gagas, K. Sasaki, T. Fukushige, A. Athavale, T. Kato and R. D. Lorenz, "Analysis of magnetizing trajectories for variable flux PM synchronous machines considering voltage, high-speed capability, torque ripple, and time duration," *IEEE Trans. on Ind. Appl.,* vol. 52, no. 5, p. 4029–4038, Sept.-Oct. 2016.

[86] G. Cardano, The Rules of Algebra: (Ars Magna), New York: Dover Publications, 2007.

[87] G. Brookfield, "Factoring quartic polynomials: a lost art," *Mathematics Magazine,* vol. 80, no. 1, p. 67–70, Feb. 2007.

[88] R. Cooke, Classical Algebra: Its Nature, Origins, and Uses, Hoboken, New Jersey: John Wiley & Sons, 2008.

[89] A. M. Aljehaimi and P. Pillay, "Novel flux linkage estimation algorithm for a variable flux PMSM," *IEEE Trans. on Ind. Appl.,* vol. PP, no. 99, p. 1–1, Jan. 2018.

[90] R. F. Schiferl and T. A. Lipo, "Power capability of salient pole permanent magnet synchronous motors in variable speed drive applications," *IEEE Trans. on Ind. Appl.,* vol. 26, no. 1, p. 115–123, Jan.-Feb. 1990.

[91]   R. Dutta and M. F. Rahman, "Design and analysis of an interior permanent magnet (IPM) machine with very wide constant power operation range," *IEEE Trans. on Energy Conv.,* vol. 23, no. 1, p. 25–33, Mar. 2008.

[92]   A. Athavale, K. Sasaki, B. S. Gagas, T. Kato and R. D. Lorenz, "Variable flux permanent magnet synchronous machine (VF-PMSM) design methodologies to meet electric vehicle traction requirements with reduced losses," *IEEE Trans. on Ind. Appl.,* vol. 53, no. 5, p. 4318–4326, Sept.-Oct. 2017.

[93]   A. Takbash, M. Ibrahim and P. Pillay, "Design optimization of a spoke type variable flux motor using AlNiCo for electrified transportation," *IEEE Trans. on Transportation Electrification,* vol. PP, no. 99, p. 1–12, Mar. 2018.

[94]   J. Jiang and J. Holtz, "An efficient braking method for controlled AC drives with a diode rectifier front end," *IEEE Trans. on Ind. Appl.,* vol. 37, no. 5, p. 1299–1307, Sept.-Oct. 2001.

[95]   E. Jung, H. Yoo, S. Sul, H. Choi and Y. Choi, "A nine-phase permanent-magnet motor drive system for an ultrahigh-speed elevator," *IEEE Trans. on Ind. Appl.,* vol. 48, no. 3, p. 987–995, May-June 2012.

[96]   A. Calle-Prado, S. Alepuz, J. Bordonau, P. Cortes and J. Rodriguez, "Predictive control of a back-to-back NPC converter-based wind power system," *IEEE Trans. on Ind. Electronics,* vol. 63, no. 7, p. 4615–4627, July 2016.

[97]   "Technical Guide No. 8. Electrical Braking," ABB Drives, 2011. [Online]. Available: http://electrical-engineering-portal.com/download-center/books-and-guides/abb-drives-technical-guides/electrical-braking. [Accessed 20 12 2017].

[98]   M. Hinkkanen and J. Luomi, "Braking scheme for vector-controlled induction motor drives equipped with diode rectifier without braking resistor," *IEEE Trans. on Ind. Appl.,* vol. 42, no. 5, p. 1257–1263, Sept.-Oct. 2006.

[99]   Y. Wang, N. Niimura and R. D. Lorenz, "Active braking schemes for low and high power induction machines using loss manipulation deadbeat-direct torque and flux control," in *2015 17th European Conf. on Power Electronics and Appl. (EPE'15 ECCE-Europe)*, Geneva, Switzerland, 2015.

[100] Y. Wang, T. Ito and R. D. Lorenz, "Loss manipulation capabilities of deadbeat direct torque and flux control induction machine drives," *IEEE Trans. on Ind. Appl.,* vol. 51, no. 6, p. 4554–4566, Nov.-Dec. 2015.

[101] M. J. Duran, I. G. Prieto, F. Barrero, E. Levi, L. Zarri and M. Mengoni, "A simple braking method for six-phase induction motor drives with unidirectional power flow in the base-speed region," *IEEE Trans. on Ind. Electronics,* vol. 64, no. 8, p. 6032–6041, Aug. 2017.

[102] M. Rastogi and P. W. Hammond, "Dual-frequency braking in AC drives," *IEEE Trans. on Power Electronics,* vol. 17, no. 6, p. 1032–1040, Nov. 2002.

[103] S. Yang and J. Chen, "Investigation of a dynamic braking scheme for switched reluctance motor drives," in *37th Annual Conf. of the IEEE Ind. Electronics Society (IECON)*, Melbourne, 2011.

[104] S. Yang and J. Chen, "Controlled dynamic braking for switched reluctance motor drives with a rectifier front end," *IEEE Trans. on Ind. Electronics,* vol. 60, no. 11, p. 4913–4919, Nov. 2013.

[105] J. S. Prasad, T. Bhavsar, R. Ghosh and G. Narayanan, "Vector control of three-phase AC/DC front-end converter," *Sadhana,* vol. 33, no. 5, p. 591–613, Oct. 2008.

Appendix

Table 0-1. Variable step size μ_1 generation code

```
function Mu1  = fcn(ampl,w,phase)

%#codegen

% Parameter vector

X = [ampl;w;phase];


% The gradient

G = [2*ampl*(cos(phase))^2 + w*cos(phase);

ampl*cos(phase) + w;

sin(phase)*cos(phase)*(1 - 2*ampl^2) - ampl*w*sin(phase)];


persistent prevG prevX


if isempty(prevG)

prevG = [0;0;0];   % Initial condition of the gradient

prevX = [0;0;0];   % Initial condition of μ1

end


s = X - prevX;

m = G - prevG;

Mu = (s' * s)/ (s' * m); % As per equation (3-17)


prevG = G;

prevX = X;


Mu1 = Mu;
```

Table 0-2. Variable-flux IPMSM parameters

Parameter	Value
Rated speed	900 RPM
Rated torque	30 N.m
Rated power	5 hp
Rated current	10 A
Resistance @ ambient temperature	1.3 Ohm
Q-axis inductance @ rated current and full MS	36.8 mH
D-axis inductance @ rated current and full MS	43.2 mH
Moment of inertia	0.03 kg.m^2
Rotor flux linkage	0 – 0.5182 V.s
Connection type	Wye

Table 0-3. Curve-fit obtained coefficients of the demagnetization curve

Coefficient	Value	Coefficient	Value
a_0	-0.0006	b_0	-0.0006
a_1	-0.0137	b_1	-0.0102
a_2	-0.0265	b_2	-0.0116
a_3	0.5091	b_3	0.2669